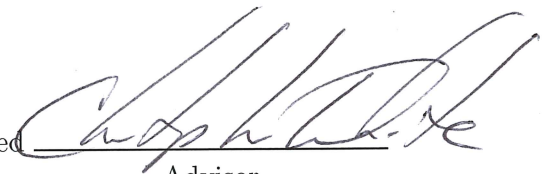


THE VERY ENERGETIC RADIATION IMAGING TELESCOPE  
ARRAY SYSTEM OBSERVATIONS OF THE STARBURST GALAXY M82

BY  
GAYLE RATLIFF

Submitted in partial fulfillment of the  
requirements for the degree of  
Doctor of Philosophy in Physics  
in the Graduate College of the  
Illinois Institute of Technology

Approved



Advisor

Chicago, Illinois  
July 2015

© Copyright by  
GAYLE RATLIFF  
July 2015

## ACKNOWLEDGMENT

I would like to thank:

- The Adler Planetarium Astronomy Department
- The faculty and staff of the IIT Physics Department
- The Illinois Space Grant Consortium
- The VERITAS Group at the University of Chicago
- The Fred Lawrence Whipple Observatory Basecamp staff
- The Women in Physics Group at IIT
- My Committee

Jeff Grube, Geza Gyuk, Larry Ciupik, Grace Wolf-Chase, Mark SubbaRao, Mark Hammergren, José Francisco Salgado, Cynthia Tarr and Rebecca Thornton of the Adler Planetarium; Professor Christopher White, Professor Sally Laurent-Muehleisen, Professor Yurii Shylnov, Professor Christena Nippert-Eng, Professor Carlo Segre, Joy Calderone, Todd Kersh, Professor Candace Wark, Omid Ahmadi, Bill Luebke, Daniel Duffty, Amy Rice, Karin Gilje, Sam Bowerman and Michael Martynowycz of the Illinois Institute of Technology; Professor Jamie Holder, Gernot Maier and Professor Martin Pohl of the VERITAS Collaboration; Professor Scott Wakely, Andrew McCann and Valeri Galtsev of the University of Chicago.

Most importantly, thank you to my family. Through all of my successes and failures, your love and encouragement has sustained me. Thank you for sacrificing so much so that I could accomplish my dream.

## TABLE OF CONTENTS

	Page
ACKNOWLEDGEMENT . . . . .	iii
LIST OF TABLES . . . . .	vi
LIST OF FIGURES . . . . .	ix
LIST OF SYMBOLS . . . . .	x
ABSTRACT . . . . .	xii
CHAPTER	
1. INTRODUCTION . . . . .	1
1.1. The Imaging Atmospheric Cherenkov Technique . . . . .	1
1.2. Starburst Galaxies as Targets for VHE $\gamma$ -ray Astronomy . . . . .	8
2. EXTENSIVE AIR SHOWERS . . . . .	11
2.1. Electromagnetic Cascades in the Atmosphere . . . . .	11
2.2. Hadronic Cascades in the Atmosphere . . . . .	15
2.3. Cherenkov Radiation from Extensive Air Showers . . . . .	17
3. THE VERITAS ARRAY . . . . .	21
3.1. Telescope Mechanics and Tracking . . . . .	21
3.2. Telescope Optics . . . . .	22
3.3. Camera and Electronics . . . . .	22
3.4. Other Peripheral Devices . . . . .	24
3.5. The VERITAS Trigger System . . . . .	24
3.6. VERITAS Data Acquisition . . . . .	26
3.7. Event Construction and Compilation . . . . .	27
3.8. Calibration . . . . .	28
4. VERITAS DATA ANALYSIS . . . . .	33
4.1. Trace Summation . . . . .	33
4.2. Double Pass Method . . . . .	34
4.3. Image Cleaning . . . . .	35
4.4. Image Parameterization . . . . .	36
4.5. Quality Cuts . . . . .	39
4.6. Event Reconstruction . . . . .	39
4.7. Energy Estimation . . . . .	40
4.8. Gamma/Hadron Separation . . . . .	42
4.9. Signal vs. Background Estimation . . . . .	43



4.10. Statistical Significance . . . . .	46
4.11. Spectral Reconstruction . . . . .	48
4.12. Flux Measurement . . . . .	49
5. DIFFUSE VHE $\gamma$ -RAY PRODUCTION IN M82 . . . . .	51
5.1. Overview of the Starburst and Starburst Core . . . . .	52
5.2. Diffuse VHE $\gamma$ -ray Production in M82 . . . . .	57
5.3. Diffuse VHE $\gamma$ -ray Emission Modeling . . . . .	58
6. VERITAS OBSERVATIONS OF M82 . . . . .	62
6.1. Quality Selection of Observations . . . . .	62
6.2. Eventdisplay Analysis . . . . .	63
6.3. Eventdisplay Results . . . . .	68
7. CONCLUSION . . . . .	74
APPENDIX . . . . .	80
A. FERMI ACCELERATION . . . . .	80
B. VHE $\gamma$ -RAY EMISSION DUE TO NEUTRAL PION DECAY . . . . .	90
B.1. Pion Production Kinematics . . . . .	91
B.2. Gamma-ray Spectrum due to Neutral Pion Decay . . . . .	96
C. CRAB SENSITIVITY STUDIES SUPPLEMENTARY TABLES . . . . .	101
C.1. Eventdisplay v470 Sensitivity Study . . . . .	102
C.2. M82 Cut Optimization . . . . .	102
D. SYSTEMATIC CHECKS . . . . .	114
BIBLIOGRAPHY . . . . .	116

## LIST OF TABLES

Table	Page
4.1 Commonly Used Air Shower Parameters. . . . .	38
4.2 Image Quality Cuts. . . . .	39
5.1 Properties of the Starburst Galaxy M82. . . . .	53
6.1 M82 Observations . . . . .	62
6.2 Standard Hard Source Cuts. . . . .	64
6.3 Summary of $\gamma$ -ray-like Events using Standard Hard Cuts . . . . .	64
6.4 V6 Size Optimization Results . . . . .	66
6.5 V5 $\theta^2$ Crab Sensitivity Results . . . . .	67
6.6 Optimized Hard Source Cuts. . . . .	68
6.7 Summary of $\gamma$ -ray-like Events . . . . .	69
6.8 $\gamma$ -ray-like Events by Energy . . . . .	73
7.1 Comparison of Eventdisplay Analyses. . . . .	75
7.2 Comparison of Energy Thresholds . . . . .	76
C.1 V4 Low Elevation Crab Runlist . . . . .	103
C.2 V4 High Elevation Crab Runlist . . . . .	104
C.3 V4 Sensitivity Results . . . . .	105
C.4 V5 Low Elevation Crab Runlist . . . . .	106
C.5 V5 High Elevation Crab Runlist . . . . .	107
C.6 V5 Sensitivity Results . . . . .	108
C.7 V6 Low Elevation Crab Runlist . . . . .	109
C.8 V6 High Elevation Crab Runlist . . . . .	110
C.9 V6 Sensitivity Results . . . . .	111
C.10 V6 Crab Low Elevation Runlist: Size Study . . . . .	112
C.11 V5 Crab High Elevation Runlist: $\theta^2$ Study . . . . .	113

## LIST OF FIGURES

Figure	Page
1.1 The Mechanism of Cherenkov Radiation. (Cherenkov 1958) . . . . .	2
1.2 The Crimean $\gamma$ -ray Telescope System. (Weekes 2013) . . . . .	3
1.3 Cherenkov Light Due to $\gamma$ -rays. (Bernlöhner 2008) . . . . .	4
1.4 $\gamma$ -ray and Proton Light Pools. (Ong 1998) . . . . .	4
1.5 Shower Imaging with Whipple. (Bernlöhner 2008) . . . . .	5
1.6 Schematic of Steroscopic Observations. (Völk & Bernlöhner 2009) . .	6
1.7 Third Generation IACTs. (Völk & Bernlöhner 2009) . . . . .	7
1.8 The Cherenkov Telescope Array. (Acharya et al. 2013) . . . . .	8
1.9 VHE $\gamma$ -ray Detections. (Wakely & Horan 2015) . . . . .	8
1.10 VHE Image of the M82 Region. (Acciari et al. 2009) . . . . .	9
2.1 Structure of a Typical Electromagnetic Cascade. (McCann 2011) .	12
2.2 Heitler's Diagram of an Electromagnetic EAS. (Heitler 1954) . . .	13
2.3 Development of an Electromagnetic EAS. (Aharonian et al. 2008)	14
2.4 Simulated $\gamma$ -ray Air Shower. (Schmidt & Knapp 2005) . . . . .	15
2.5 Structure of a Typical CR Proton-induced Cascade. (McCann 2011)	16
2.6 Simulated Proton Air Shower. (Schmidt & Knapp 2005) . . . . .	17
2.7 Lateral Distribution of Cherenkov Photons. (Meier 2012) . . . . .	18
2.8 $\gamma$ -ray and CR Cherenkov Light Pools. (Ong 1998) . . . . .	19
2.9 Random $\gamma$ -ray and CR Simulation Results. (Maier 2014) . . . . .	20
3.1 The Very Energetic Radiation Imaging Telescope Array System. .	21
3.2 Hexagonal Mirrors of the VERITAS Reflector . . . . .	22
3.3 Cross Section of a PMT. (Hamamatsu 2010) . . . . .	23
3.4 The VERITAS Camera. (Kieda 2013) . . . . .	24
3.5 The VERITAS Trigger System. (Weinstein 2007) . . . . .	26

3.6	Relative Gains and their Gaussian Distribution. (Meier 2014) . . .	29
3.7	Single PE Calibration Tools. (Meier 2014). . . . .	30
3.8	Reflectivity Measurements. (Courtesy of Emmet Roache) . . . . .	30
3.9	Optical Alignment Apparatus. (McCann et al. 2009) . . . . .	31
3.10	Optical Alignment Diagram. (McCann et al. 2009) . . . . .	32
4.1	Structure of the Eventdisplay Analysis Tool. (Maier 2014) . . . . .	33
4.2	Sample Air Shower Tzero values. (Holder 2005) . . . . .	35
4.3	Two FADC Traces. (Prokoph 2013) . . . . .	36
4.4	VERITAS Camera Image Before and After Cleaning. (Maier 2014)	37
4.5	Original Hillas Parameters. (Fegan 1997) . . . . .	37
4.6	Arrival Direction and Shower Core Position. (Prokoph 2013) . . .	40
4.7	Energy Look-up Tables. (Prokoph 2013) . . . . .	42
4.8	Distribution of Mean-scaled Parameters. (Prokoph 2013) . . . . .	44
4.9	Ring and Reflected-region Background Models. (Berge et al. 2007)	45
4.10	Typical $\gamma$ -ray Counting Rates. (Li & Ma 1983) . . . . .	47
4.11	Effective Area Derivation. (Maier 2014) . . . . .	49
5.1	M82. (NASA, ESA, & Hubble Heritage Team) . . . . .	51
5.2	Neutral Hydrogen Gas Structure of the M81 Group. (Yun et al. 1995)	54
5.3	Photographic Plate of M82. (O'Connell & Mangano 1978) . . . . .	55
5.4	M82 at Mid-IR Wavelengths. (Lipsy & Plavchan 2004) . . . . .	55
5.5	Discrete Radio Sources in the Core of M82. (Fenech et al. 2008) .	56
5.6	The Superwind of M82. (Subaru Telescope Facility 2011) . . . . .	57
5.7	Code Flow of <i>Q-Diffuse</i> . (de Cea del Pozo et al. 2009) . . . . .	60
5.8	Predicted Differential $\gamma$ -ray Flux. (de Cea del Pozo 2009) . . . . .	61
6.1	VERITAS Run Log Generator Sample Output. . . . .	63
6.2	Summary of Crab Sensitivity Results. . . . .	65
6.3	V4 and V5 $\theta^2$ Plots from Crab Study. . . . .	68

6.4	Excess VHE $\gamma$ -ray Events in the M82 Region. . . . .	70
6.5	M82 Spectrum. . . . .	71
6.6	M82 Flux Estimates. . . . .	72
7.1	M82 Spectral Energy Distribution with Theoretical Predictions. . . . .	77
7.2	Simulation of CTA Observations of M82. (Acero et al. 2013) . . . . .	79
A.1	Type B Reflection of a Cosmic Ray Particle. (Fermi 1949) . . . . .	82
A.2	Elastic Scattering in a Magnetic Cloud. (Kachelrieß 2008) . . . . .	82
A.3	Dynamics of a Strong Shock. (Longair 2011) . . . . .	85
A.4	Oblique Shock. (Bell 1978) . . . . .	88
A.5	SNR RX J0852.0-4622. (Aharonian et al. 2007) . . . . .	89
B.1	Energy Momentum and Velocity Triangles. (Stecker 1971) . . . . .	92
B.2	Energy Distribution of Two-body Decay. (Stecker 1971). . . . .	97
B.3	Predicted $\gamma$ -ray Spectrum due to Pion Decay. . . . .	100
D.1	Significance Metrics. . . . .	115
D.2	Reconstructed Crab Spectrum. . . . .	116

## LIST OF ABBREVIATIONS

Abbreviation	Definition
AGN	Active Galactic Nucleus
CCD	Charge-coupled Device
CR	Cosmic Ray
CTA	The Cherenkov Telescope Array
DAT	Digital Asynchronous Transceiver Module
EAS	Extensive Air Shower
FADC	Flash Analog-to-digital Converter
Fermi LAT	Fermi Large Area Telescope
FIR	Far Infrared
H.E.S.S.	The High Energy Spectroscopic Array
IACT	Imaging Atmospheric Cherenkov Telescope
LED	Light-emitting Diode
LUT	Look-up Table
MSCL	Mean-scaled Length
MSCW	Mean-scaled Width
NSB	Night Sky Background
OSS	Optical Support Structure
PDM	Pulse Delay Module
PE	Photo-electron
PMT	Photomultiplier Tube
PSF	Point Spread Function

PWN	Pulsar Wind Nebula
SFR	Star Formation Rate
SNR	Supernova Remnant
VHE	Very High Energy (100 GeV-100 TeV)

## ABSTRACT

This work describes the Very Energetic Radiation Imaging Telescope Array Systems (VERITAS) observations of the starburst galaxy M82 by documenting the analysis of 231 quality-selected hours of observational data taken between 2008 and 2014. The prototypical starburst galaxy, M82’s high supernova (SN) rate and dense central accumulation of molecular gas make it a promising candidate for studying cosmic ray (CR) acceleration and propagation with the detection of diffuse very high energy (VHE; approximately 100 GeV-100 TeV)  $\gamma$ -ray emission. This diffuse emission is predicted to result from proton-proton interactions within the galaxy’s core that produce VHE  $\gamma$ -rays through neutral pion decay. This work confirms the results of the initial VERITAS publication covering 137 hours of M82 observations between January 2008 and April 2009, yielding a total of 103.5 excess  $\gamma$ -ray-like events (0.007  $\gamma$ /min, 5.7 pre-trial statistical significance) from a deeper exposure of 231 hours of observation. The spectral properties found are in agreement with the original detection within errors ( $\Gamma=2.85 \pm 0.39$ ). These results are consistent with paradigms that describe the production of CRs via the conversion of mechanical energy generated in supernovae (SNe). These findings will improve current diffuse emission models by better constraining galaxy parameters and by providing insight into CR proton loss processes and timescales, with further understanding to be gained with the introduction of the Cherenkov Telescope Array (CTA).



## CHAPTER 1

### INTRODUCTION

#### 1.1 The Imaging Atmospheric Cherenkov Technique

In 1934, Pavel Cherenkov discovered that charged particles (electrons,  $\pi$ -mesons, protons) moving uniformly in a medium (e.g. water) emit radiation when traveling at speeds exceeding the phase velocity of light in that medium (Cherenkov 1934). The unusual characteristics of this radiation, in particular its pronounced spatial asymmetry, ruled out any before seen luminescence phenomenon. Cherenkov postulated that these charged particles created electromagnetic excitations, propagating light waves at an angle to the direction of motion (Cherenkov 1958).

Il'ja Frank and Igor Tamm continued to investigate the fundamental properties of this radiation, developing a complete theory and naming this radiation *Vavilov-Čerenkov Radiation*, to commemorate its discovery by Cherenkov and to emphasize the role played by Cherenkov's scientific advisor at the Russian Academy of Sciences, Sergei Vavilov (Tamm & Frank 1937; Tamm 1958). Cherenkov, Frank, and Tamm all received Nobel Prizes in 1958, and today this radiation is commonly known as *Cherenkov Radiation*. Figure 1.1 shows the mechanism of Cherenkov radiation. Radiation is emitted at some angle,  $\Theta$ , relative to the motion of a charged particle traveling at velocity,  $v$ . The waves are “quenched through interference” in all directions except at angle  $\Theta$  in which:  $\cos \Theta = \frac{1}{\beta n}$ , where  $\beta$  is the ratio of  $v$  to the speed of light,  $c$ , and  $n$  is the refractive index of the medium (Cherenkov 1958).

The idea of *atmospheric Cherenkov radiation* was first proposed by P.M.S. Blackett in July of 1947 at the Royal Society's Gassiot Committee meeting, organized to investigate optical radiation in the upper atmosphere. He suggested a possible contribution to the continuous spectrum of the night sky background (NSB) due

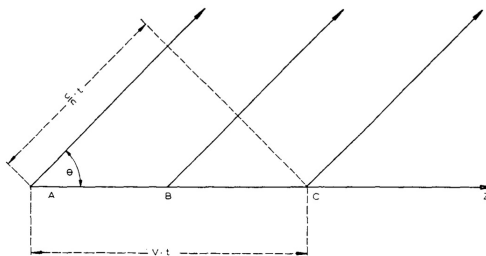


Figure 1.1. The Mechanism of Cherenkov Radiation. (Cherenkov 1958)

to Cherenkov radiation resulting from energetic charged cosmic rays (CRs) traveling through the atmosphere (“Emission Spectra” 1947, Blackett 1948). It was soon proposed that  $\gamma$ -rays ( $\sim 0.2$ -400 MeV: Morrison 1958;  $\sim$ TeV: Cocconi 1959) could also initiate air showers with detectable Cherenkov light.

The first atmospheric Cherenkov experiments focused on the detection of cosmic ray (e.g. Galbraith & Jelley 1953), but later groups targeted  $\gamma$ -ray initiated events. It is generally recognized that the first experiment designed to detect the Cherenkov light from  $\gamma$ -ray initiated air showers was conducted in the Crimea by a group of scientists from the Lebedev Institute in Moscow (Zatsepin & Chudakov 1961). All results from the Crimean group were negative, but others were inspired to use the technique based on the simplicity of the detector (see Weekes 1995). A number of other groups pursued the technique early on, including a British-Irish group (Fruin et al. 1964), a group based in India (Tata Institute of Fundamental Research; see Acharya 2005), and a Smithsonian group (Fazio et al. 1968). The Crimean  $\gamma$ -ray telescope system is shown in Figure 1.2 (Lorenz & Wagner. 2012, courtesy of Trevor Weekes). Each barrel contained a phototube and was positioned on rails to view the sky at different angles.

These first generation experiments looked for excesses in Cherenkov light but made no attempt to discriminate between the Cherenkov light caused by  $\gamma$ -rays and



Figure 1.2. The Crimean  $\gamma$ -ray Telescope System. (Weekes 2013)

the Cherenkov light caused by the very large background of cosmic rays. Second-generation detectors used an *imaging* technique. Imaging atmospheric Cherenkov detectors were designed not only to detect, but also to characterize the Cherenkov light in the atmosphere. The imaging technique exploits fundamental differences in the Cherenkov light pools generated by the two sources of emission: cosmic rays (CRs) and very high energy (VHE, approximately 100 GeV-100 TeV)  $\gamma$ -rays .

When a VHE  $\gamma$ -ray reaches the atmosphere, pair production in the Coulomb field of an atomic nucleus creates electrons and positrons that then emit Bremsstrahlung radiation, producing more photons. The pair production/Bremsstrahlung process repeats itself until the energy of the electrons become so small that ionization losses dominate. This series of events is called an *electromagnetic air shower*. The number of particles in an air shower grows exponentially while reaching its maximum, giving rise to thousands of particles. This cascade of high energy charged particles creates a relatively uniformly illuminated pool of Cherenkov light on the ground. Figure 1.3 shows the Cherenkov light produced by a single charged particle and the light pool due to a Primary 1 TeV  $\gamma$ -ray (Bernlöhner 2008).

Cosmic rays create hadronic air showers which are more disordered and laterally spread. High energy protons entering the atmosphere initiate pion production

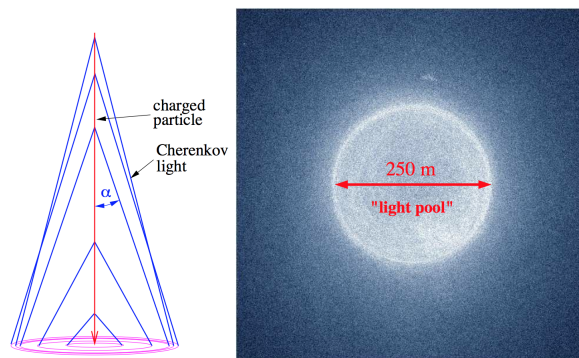


Figure 1.3. Cherenkov Light Due to  $\gamma$ -rays. (Bernlöhr 2008)

which seeds an electromagnetic component via neutral pion decay. Charged pions seed hadronic and muonic components. As a result, CR-induced showers produce Cherenkov light that is more disordered and more laterally-spread. These characteristics help distinguish between  $\gamma$ -rays and CRs when air showers are *imaged*. Figure 1.4 shows Cherenkov light pools on the ground due to a 50 GeV  $\gamma$ -ray initiated air shower (left) and a 200 GeV proton initiated air shower (right).

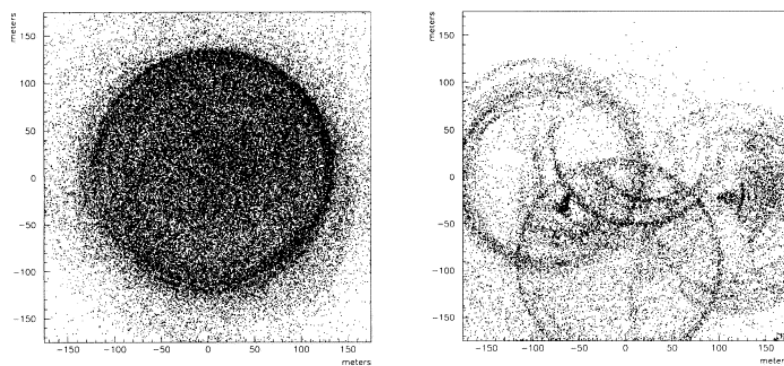


Figure 1.4.  $\gamma$ -ray and Proton Light Pools. (Ong 1998)

Using multi-pixel cameras composed of sensitive photomultiplier tubes (PMTs),  $\gamma$ -ray initiated air showers can be distinguished from CR initiated showers based on the camera images of their Cherenkov light pools.<sup>1</sup> One of the earliest imaging at-

<sup>1</sup>Also, arrival times of the Cherenkov photons in the camera (see Prokoph 2009)

atmospheric Cherenkov telescopes, the Whipple Observatory in southern Arizona, was constructed in 1968, and updated in to include a multi-pixel camera in 1984 (see *Timeline to VERITAS* 2015). Whipple obtained the first VHE  $\gamma$ -ray detection, a detection of the Crab Nebula with the help of a 37-pixel (PMT) camera and better analysis techniques to allow cuts on various parameters to extract the  $\gamma$ -ray signal (Weekes et al. 1989). Figure 1.5 shows shower imaging using Whipple.

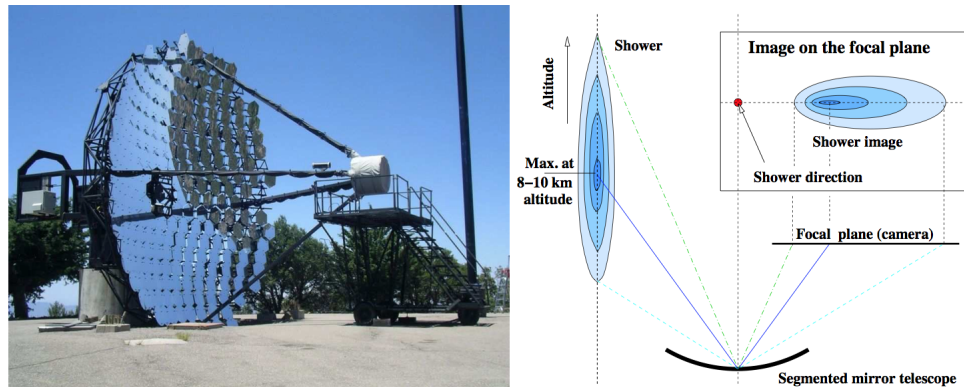


Figure 1.5. Shower Imaging with Whipple. (Bernlöhr 2008)

In general, the performance of imaging atmospheric Cherenkov telescopes (IACTs) has been improved by:

- Increasing mirror diameters (to detect fainter showers and effectively lower the energy threshold)
- Increasing the number of PMTs in the focal plane (to increase the field of view and improve shower image resolution)
- By making observations *stereoscopically* using several telescopes (see Lidvansky 2006).

Using a stereo technique, telescopes are separated by a distance commensurate with the size of the Cherenkov light pool. Pioneered by the HEGRA telescope array

on La Palma, the stereoscopic technique provides multiple projections of a single air shower. Stereoscopic observations lower trigger thresholds, improve spatial and energy resolution, and results in better CR background rejection (Daum et al. 1997), due to a number of favorable effects, including the suppression of local muon triggers, better localization of the air shower and better reconstruction of the Cherenkov light pool (see Funk et al. 2004).

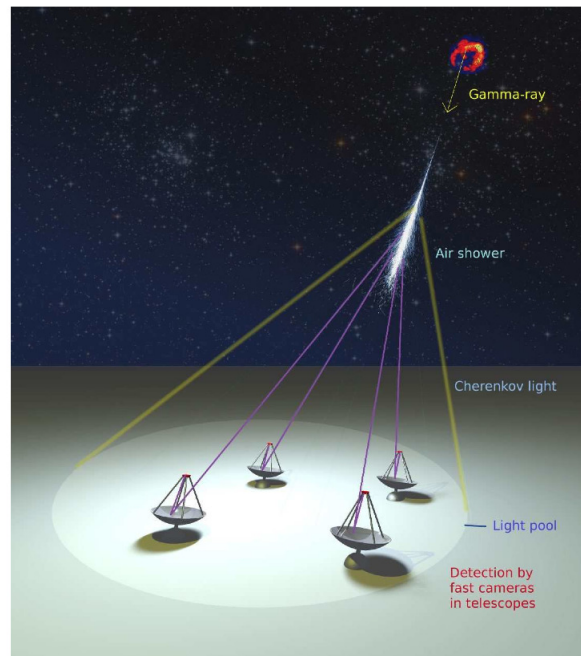


Figure 1.6. Schematic of Stereoscopic Observations. (Völk & Bernlöhr 2009)

With these improvements, third generation IACT's use pixelated ( $\sim 100$  pixels) cameras and operate in arrays, by in large. These detectors consist of: CANGAROO III near Woomera, South Australia, H.E.S.S. in Namibia, MAGIC on La Palma, and VERITAS in southern Arizona.<sup>2</sup> These third generation telescopes reach sensitivities  $\sim 0.7\%$  of the Crab Nebula flux ( $> \text{TeV}$ , 50 hrs of Observations; Acharya et al. 2013) and have resulted in a large increase in the number of VHE  $\gamma$ -ray detections.

---

<sup>2</sup>MAGIC was initially designed and until 2009 operated as a large single telescope.

Currently, there are 154 known VHE  $\gamma$ -ray sources, the majority of the detections resulting from these instruments (see Wakely & Horan 2015).

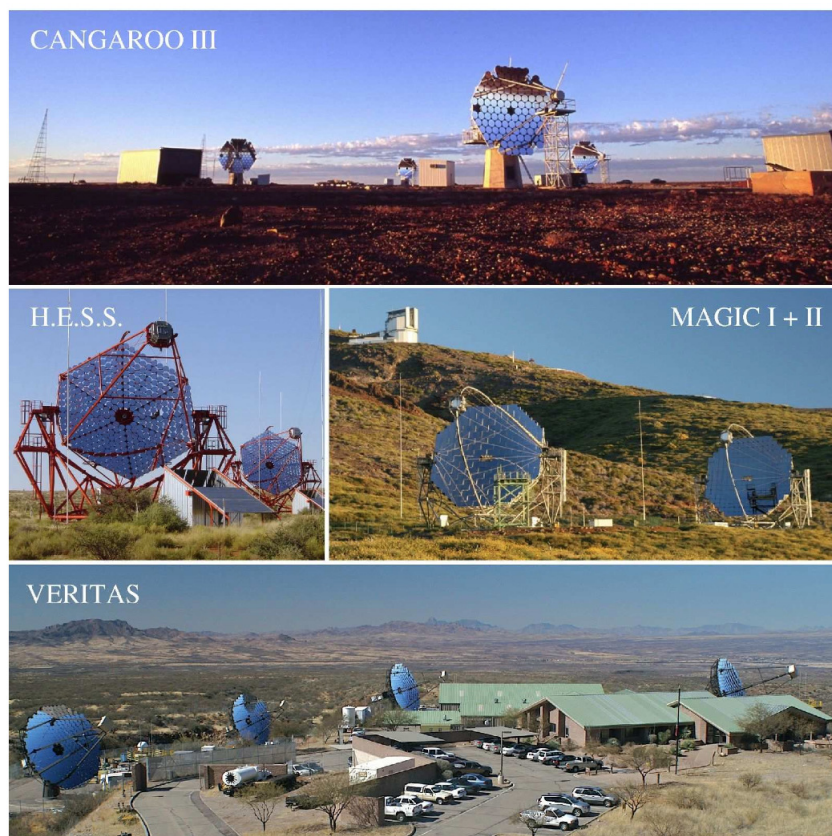


Figure 1.7. Third Generation IACTs. (Völk & Bernlöhr 2009)

Plans for the next generation of IACTs currently center on the Cherenkov Telescope Array (CTA). Currently in the planning stages, CTA will yield a factor of ten improvement in sensitivity and extend the accessible energy range ( $< 100$  GeV to  $> 300$  TeV). The CTA proposal calls for a combination of telescopes of different sizes in a large array consisting of 50-100 telescopes at two different sites. Expected to have the ability to detect  $\sim 1,000$  sources, CTA will provide unprecedented angular and energy resolution. Figure 1.8 shows an artist's concept of CTA.



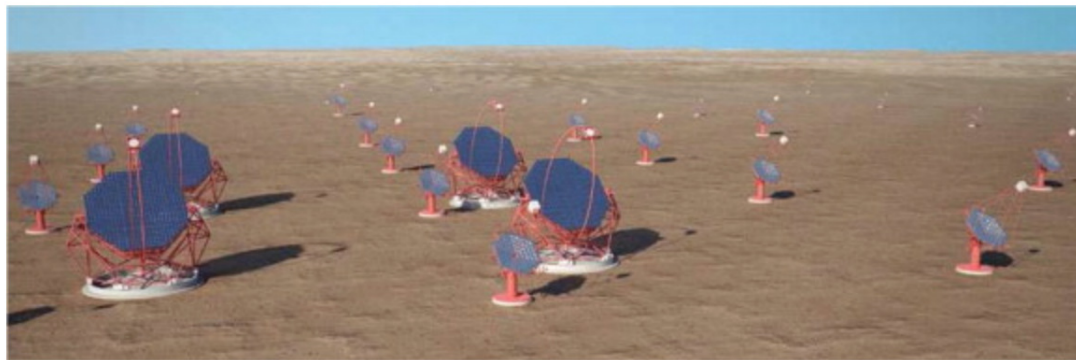


Figure 1.8. The Cherenkov Telescope Array. (Acharya et al. 2013)

## 1.2 Starburst Galaxies as Targets for VHE $\gamma$ -ray Astronomy

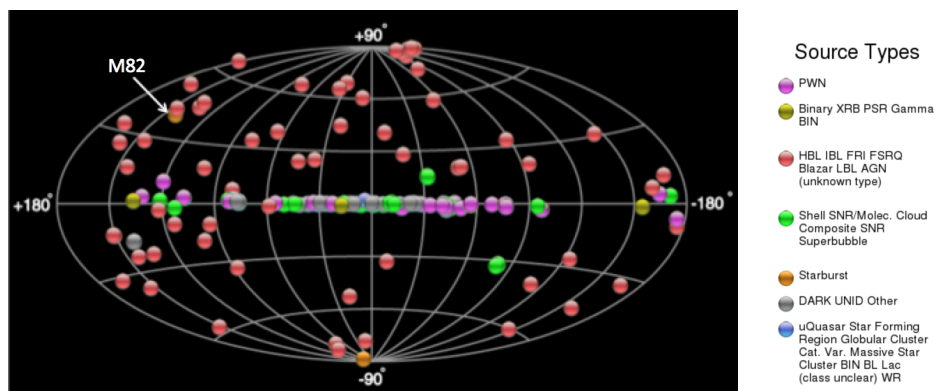


Figure 1.9. VHE  $\gamma$ -ray Detections. (Wakely & Horan 2015)

VERITAS has detected VHE  $\gamma$ -rays from over 40 sources, including two starburst galaxies, galaxies undergoing periods of increased star formation—including M82, discovered in 2009. The following year, two starburst galaxies, M82 and NGC253, were detected by the Fermi LAT instrument (Abdo et al. 2010;  $\sim$  GeV energies). Figure 1.9 shows all VHE  $\gamma$ -ray detections to date. Two starburst galaxies appear as orange dots (M82, northern hemisphere; NGC 253, southern hemisphere). Figure 1.10 shows the M82 region in VHE energies. This sky map shows the excess of  $\gamma$ -ray events above the estimated background. The VERITAS point spread function (PSF; 68% containment) is represented by a white circle. The black star denotes the



location of the core of the galaxy.

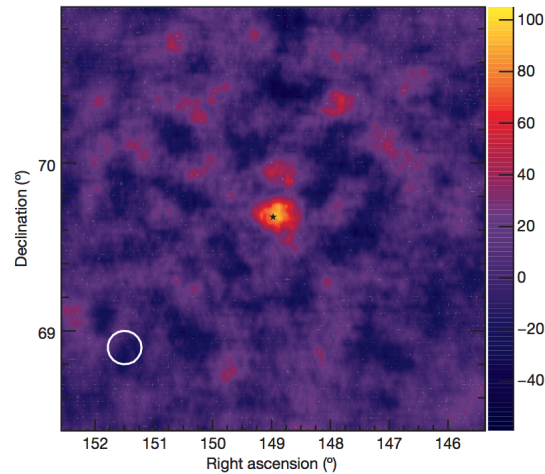


Figure 1.10. VHE Image of the M82 Region. (Acciari et al. 2009)

The detection of M82 is notable not only because it is the only object of its kind detected by the VERITAS array, but also because it is one of the only extragalactic source detected whose emission is not dominated by an active galactic nucleus (AGN) or accretion onto a supermassive black hole. This makes it possible to study cosmic ray (CR) acceleration and propagation with the detection of the galactic diffuse VHE emission.

Within the core of M82, increased star formation due to the accumulation of interstellar gas and high supernova rates create enhanced  $\gamma$ -ray emission as dense gas serves as a target for CRs. VHE  $\gamma$ -rays are produced primarily via neutral pion decay, and rates of  $\gamma$ -ray production are closely tied to CR escape timescales within the galaxy's core. In this sense, observations of starburst galaxies not only provide valuable information on the mechanism of CR acceleration but also on the conditions within the galaxy.

This work details VERITAS observation of M82 by documenting the analysis of the full data set, 231 quality-selected hours of observations taken between 2008

and 2014. M82 is one of the weakest sources ever detected by the VERITAS array and the data analysis involves careful extraction of the  $\gamma$ -ray signal and an understanding of the instrument's performance and sensitivity. The results provide insight into the analysis of weak VHE  $\gamma$ -ray sources and help to better constrain emission estimates, providing insight into CR acceleration and diffuse emission models.

## CHAPTER 2

### EXTENSIVE AIR SHOWERS

High energy cosmic rays (CRs) and electromagnetic radiation enter the Earth's atmosphere and create cascades of secondary particles known as *extensive air showers* (EAS). Ground based very high energy (VHE)  $\gamma$ -ray experiments derive information about primary particles and radiation from these secondary particles, particularly from the Cherenkov light that these secondary particles produce. Understanding the properties of primary particles and radiation depends on modeling complex, high energy interactions that lead to pools of Cherenkov light on the ground. This section provides a description of high energy extensive air showers and the models used to understand the key physical processes and the shower characteristics exploited in the VERITAS analysis chain.

#### 2.1 Electromagnetic Cascades in the Atmosphere

For a VHE  $\gamma$ -ray entering the atmosphere, the most dominant loss mechanism is pair production. Pair production occurs in the Coulomb field of a nucleus when an incident  $\gamma$ -ray is completely annihilated and its energy is transferred to an electron/positron pair. The two particles then interact with molecules in the air to give secondary  $\gamma$ -rays via bremsstrahlung. These secondary  $\gamma$ -rays can also undergo pair production, creating an exponentially growing shower of secondary particles. What results is a very narrow cascade of particles with the major axis pointing in the direction of the incident  $\gamma$ -ray. The small lateral spread of the cascade results primarily from multiple Coulomb scattering.

The shower process continues, creating new particles in the cascade, until the average energy of the particles drops to a point where ionization energy losses and radiation losses become equal. This energy is known as the critical energy,  $\xi_c^e$ . Once

the critical energy is reached, the number of particles in the shower diminishes, and the cascade dies away. Figure 2.1 shows the structure of a typical electromagnetic cascade.

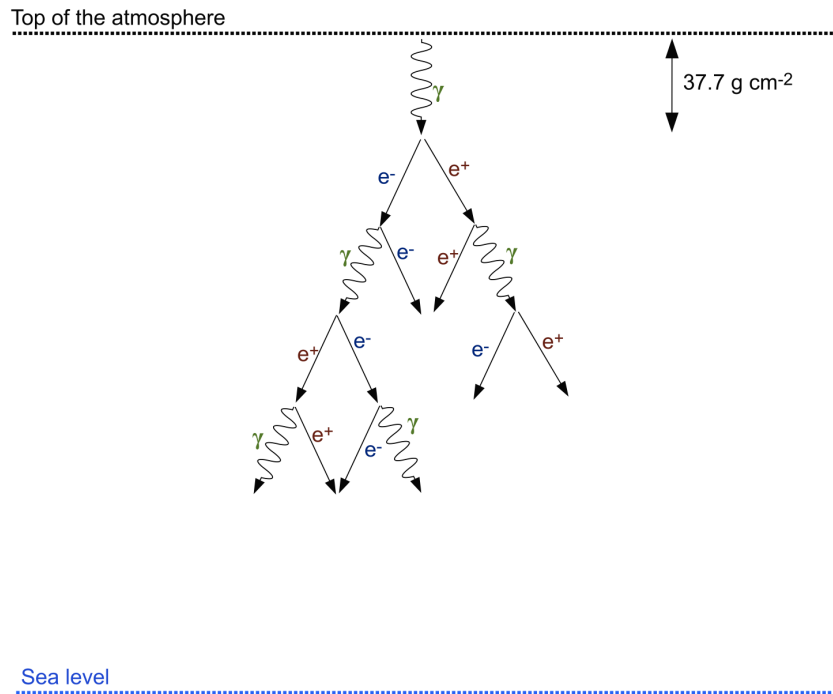


Figure 2.1. Structure of a Typical Electromagnetic Cascade. (McCann 2011)

To first approximation, in each radiation length, a single particle produces two more particles that share its energy. In his simple model, Heitler (1954) defined a *splitting length* over which the number of particles doubles:  $d = \lambda_T \ln 2$ , where  $\lambda_T$  is the radiation length. After  $n$  splittings, the total number of particles in the shower is given by,  $N = 2^n$ . The cascade reaches a maximum when all particles reach the critical energy. In terms of the initial energy,  $E_0$ :

$$E_0 = \xi_c^e N_{\max}. \quad (2.1)$$

Figure 2.2 shows Heitler's diagram of an electromagnetic extensive air shower. At each increment of  $d$ , the number of particles is multiplied by 2, by pair production or

by single photon bremsstrahlung. This process continues until the energy falls below the critical energy.

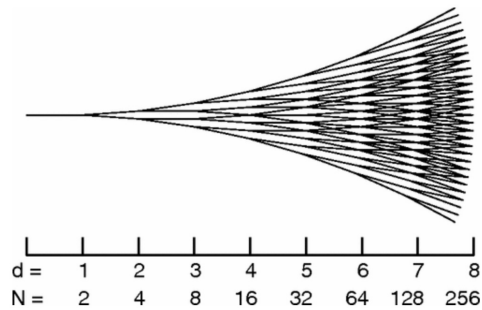


Figure 2.2. Heitler's Diagram of an Electromagnetic EAS. (Heitler 1954)

The atmospheric depth at which the shower reaches its maximum is determined by the point at which the number of splittings reaches its maximum value,  $N_{\max} = 2^{n_{\max}}$ .

Combining this expression with equation 2.1:

$$n_{\max} = \ln[E_0/\xi_c^e]/\ln(2) \quad (2.2)$$

and the total depth reached by the shower is given by:

$$X_{\max} = n_{\max}d = n_{\max}\lambda_T \ln(2) = \lambda_T \ln[E_0/\xi_c^e] \quad (2.3)$$

While the Heitler model does not account for all loss and production (particularly it does not model the loss of particles), a number of important features are accounted for by this simple electromagnetic cascade model:

- The final number of electrons, positrons, and photons in the shower is directly proportional to energy of the initial  $\gamma$ -ray.
- The depth of the shower maximum is logarithmically proportional to the energy of the initial  $\gamma$ -ray.

These features in particular are exploited in the VERITAS analysis chain discussed in later sections. Figure 2.3 shows the longitudinal development of an electromagnetic extensive air shower for several primary  $\gamma$ -ray energies based on the Heitler model (Aharonian et al. 2008). The x-axis shows the atmospheric depth expressed as radiation lengths, while the y-axis shows the number of particles in the electromagnetic cascade.

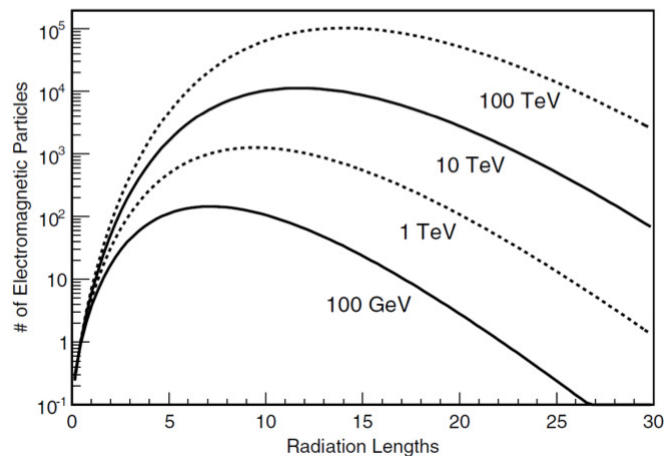


Figure 2.3. Development of an Electromagnetic EAS. (Aharonian et al. 2008)

To fully model electromagnetic cascades, transport equations that take into account all particle loss and production must be solved. VERITAS analysis relies on the COsmic Ray SIMulations for KAscade (CORSIKA), a Monte Carlo program capable of modeling extensive air showers up to very high energies ( $E > 10^{20}$  eV; Heck et al. 1998). CORSIKA includes the EGS4 package (Nelson et al. 1985) which is capable of simulating the coupled transport of electrons and photons from a few keV to several TeV and takes into account numerous processes including bremsstrahlung and pair production using formulas for relativistic cross sections. Figure 2.4 shows CORSIKA results for the simulation of a 50 GeV photon. The figure shows the shower projected onto the XZ and XY planes. These figures show  $0 < z < 30.1$  km and 5 km

around the shower core. Each red track represents the path of an electron, positron, or  $\gamma$ -ray ( $E > 0.1$  MeV; Schmidt & Knapp 2005).

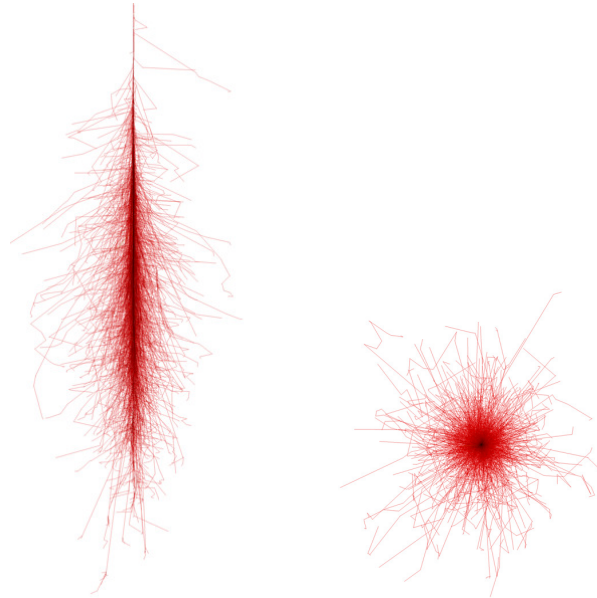


Figure 2.4. Simulated  $\gamma$ -ray Air Shower. (Schmidt & Knapp 2005)

## 2.2 Hadronic Cascades in the Atmosphere

The vast majority of extensive air showers detected by VERITAS are initiated by the very large background of charged cosmic rays, primarily high energy protons. Charged protons collide with nuclei of atmospheric atoms, initiating the production of pions. Charged pions interact with other atmospheric nuclei to produce more secondaries, until they fall below a critical energy and decay into muons and neutrinos. Neutral pions quickly decay into  $\gamma$ -rays that in turn create electromagnetic cascades. Figure 2.5 shows the structure of a typical hadronic cascade.

For a proton-initiated air shower, hadrons account for only a small percentage of the particles produced in the cascade; however, the hadronic component fuels the electromagnetic component via the decay of neutral pions. Due to the transverse momentum acquired during their production, pions are produced with a lateral spread.

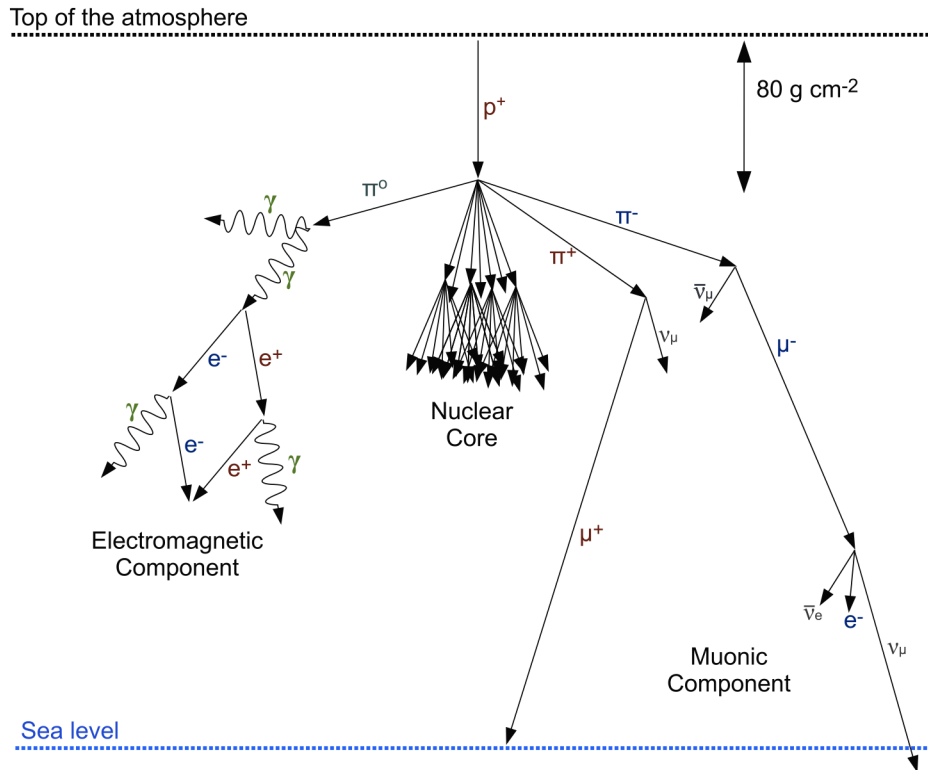


Figure 2.5. Structure of a Typical CR Proton-induced Cascade. (McCann 2011)

In general, this spread is larger than that of the particles produced in electromagnetic cascades.

To model hadronic interactions at low energies, FLUKA, a hadron-nucleon interaction model, is used in CORSIKA (FLUKA: Battistoni et al. 2007). For energies above  $\sim 100 \text{ GeV}$ , there are several models, some with differing assumptions, as models must extrapolate cross sections from accelerator data into higher energies (for a comparison of high energy hadronic models see: Greider 2010 and Stokes et al. 2013). The VERITAS analysis chain often uses QGSJET to model high energy hadronic reactions (QGSJET: Ostapchenko 2013). Figure 2.6 shows CORSIKA results for the simulation of a 100 GeV proton. The figure shows the shower projected onto the XZ and XY planes. These figures show  $0 < z < 30.1 \text{ km}$  and 5 km around the shower core. Red tracks indicate the path of electrons, positrons, and  $\gamma$ -rays ( $E > 0.1$



MeV). Blue and green tracks represent the paths of hadrons and muons respectively ( $E > 0.1$  GeV; Schmidt & Knapp 2005).

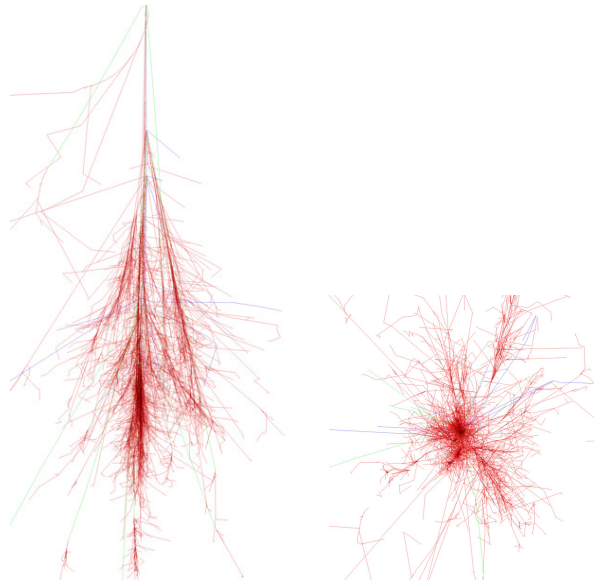


Figure 2.6. Simulated Proton Air Shower. (Schmidt & Knapp 2005)

### 2.3 Cherenkov Radiation from Extensive Air Showers

When a charged particle is moving through a dielectric medium (refractive index,  $n$ ) at speeds greater than that of light in the medium ( $v > c/n$ ), coherent radiation known as *Cherenkov Radiation* occurs (see Section 1.1). The angle of the wavefront with respect to the motion of the particle is given by:

$$\cos \theta = c/nv \quad (2.4)$$

For the Earth's atmosphere the angle of this wavefront is approximately  $1^\circ$ . However, the angle of emission of the Cherenkov light is a function of the density of the air, and therefore tied to the emission height of the particle.

The wavefront creates a faint ( $\sim 100$  photons/m<sup>2</sup>), short ( $\sim$ ns) electromagnetic flash that peaks at wavelengths between 300 and 350 nm for a 1 TeV photon. For an air shower that starts at an altitude of 20-25 km above sea level, a *Cherenkov*

*light pool* of radius  $\sim 100$  m develops on the ground, due to the numerous relativistic charged particles cascading toward the earth. Figure 2.7 shows the lateral distribution of photons on the ground due to the Cherenkov light produced by a range of  $\gamma$ -ray energies.

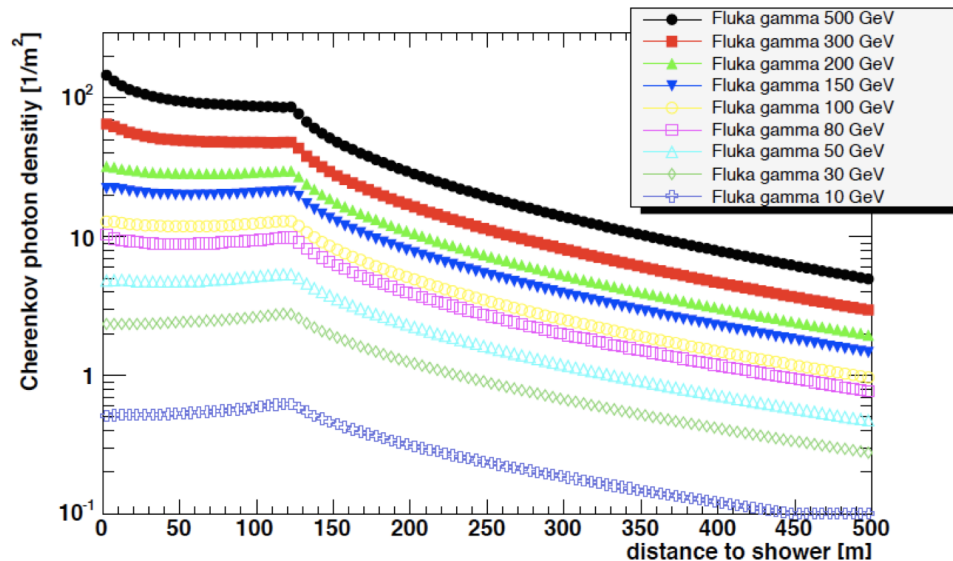


Figure 2.7. Lateral Distribution of Cherenkov Photons. (Meier 2012)

The charged particles created in CR-initiated showers also produce Cherenkov light, and similarly a Cherenkov light pool develops on the ground. However, a CR light pool appears more disordered, and in general this pool is more laterally spread. Gamma/hadron separation in the VERITAS analysis chain exploits these differences in the Cherenkov light pools. Figure 2.8 shows two Cherenkov light pools, one due to an electromagnetic cascade (left), the other due to a hadronic cascade (right). The Cherenkov light produced by the  $\gamma$ -ray appears symmetrical while the CR light pool appears more disordered with a greater lateral spread.

In CORSIKA, the Cherenkov photons due to electrons, positrons, muons, and charged hadrons are modeled using a program extension developed by the HEGRA collaboration (Arqueros et al. 1993) and improved by Bernlöhner (2008). The extension

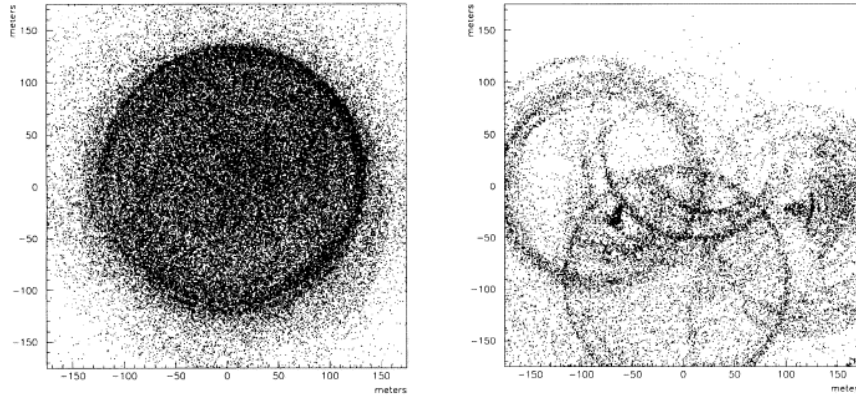


Figure 2.8.  $\gamma$ -ray and CR Cherenkov Light Pools. (Ong 1998)

allows for the estimation of Cherenkov photons arriving at the lowest level of observation, accounting for atmospheric absorption due to factors such as Rayleigh and Mie scattering, ozone absorption, and scattering due to water vapor. CORSIKA outputs for 5 randomly selected Cherenkov light pools due to  $\gamma$ -ray (top) and proton (bottom) air showers are shown in Figure 2.9. CORSIKA is able to account for uncertainties in interaction parameters using a Monte Carlo approach so each run produces distinct results. The following sections detail how extensive air showers are detected by the VERITAS array and used in the VERITAS analysis chain.

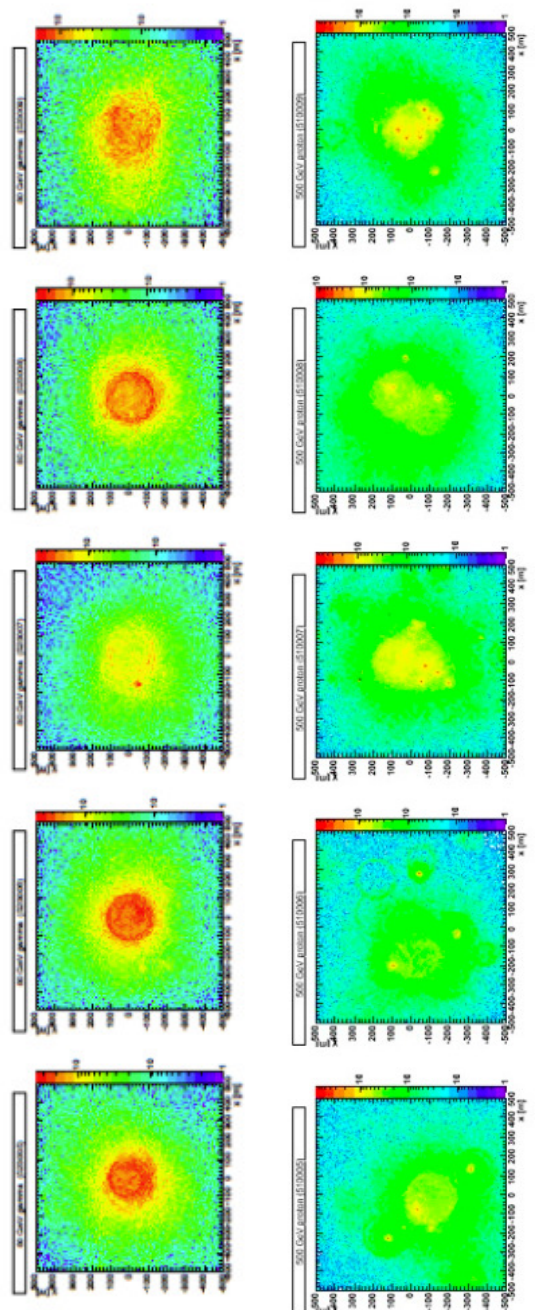


Figure 2.9. Random  $\gamma$ -ray and CR Simulation Results. (Maier 2014)

## CHAPTER 3

### THE VERITAS ARRAY



Figure 3.1. The Very Energetic Radiation Imaging Telescope Array System.

The Very Energetic Radiation Imaging Telescope Array (VERITAS) is a ground-based imaging atmospheric Cherenkov telescope (IACT) array located in southern Arizona ( $31^{\circ}40'33.7008, -110^{\circ}57'10.1376$ ). VERITAS is located 1275 m above sea level (Holder et al. 2006) at the basecamp of the Fred Lawrence Whipple Observatory. The first telescope became operational in 2005, and the four-telescope array was completed in 2007. Since 2007, the VERITAS array has been continually modified to improve sensitivity, including relocation of telescope #1 (T1) in 2009, the upgrade of the trigger system in 2011, and the installation of high quantum efficiency (high-QE) photomultiplier tubes (PMTs) in 2012. This section describes the current VERITAS array.

### 3.1 Telescope Mechanics and Tracking

Each VERITAS telescope consists of an altitude-over-azimuth positioner manufactured by RPM-PSI (Northridge, California) and a tubular steel optical support structure (OSS) custom manufactured by M3 Engineering (Tucson, Arizona). The camera is supported by a quadropod with a counterweight attached to the upper arm. The maximum slew speed is  $1^{\circ}$  per second and the telescope position measurements

are encoded at a rate of 4 Hz. Typical pointing accuracy is  $\pm < 0.01^\circ$  (Holder 2006).

### 3.2 Telescope Optics

The VERITAS optics follows the Davies-Cotton design (Davies & Cotton 1957), creating a 12 m aperture reflector using 350 hexagonal mirrors. Each mirror has an area of  $0.322 \text{ m}^2$  and a  $24.0 \pm 1\%$  radius of curvature. The mirrors were fabricated to have reflectivity values of approximately  $> 90\%$  at 320 nm and  $\geq 85\%$  between 280 nm and 450 nm (Roache et al. 2008). The total reflector area is approximately  $110 \text{ m}^2$ . The optical point spread function (PSF) is defined as the 80% containment radius of the light from a point source at infinity, after the light is propagated through the reflectors of the optical system and into the PMT pixels of the camera on the focal plane. The PSF is less than  $0.05^\circ$  at operational elevations (McCann 2009).



Figure 3.2. Hexagonal Mirrors of the VERITAS Reflector

### 3.3 Camera and Electronics

Photomultiplier tubes (PMTs) provide the basis for the detection of Cherenkov



light generated by VHE  $\gamma$ -rays. PMTs have an extremely fast response time and are sensitive to faint light in the ultraviolet, visible, and near infrared range. A typical PMT consists of a photoemissive cathode (photocathode), an electron multiplier, and an anode in a vacuum tube. When light enters the PMT, a photon strikes the photocathode and causes the emission of an electron(s) into the vacuum. The electrons are directed by a focusing electrode toward the electron multiplier, or dynode. These dynodes are electrical conductors (coated with a secondary emissive material), each kept at a more positive potential than its predecessor. It is in this way that the incoming photoelectrons are multiplied by a secondary emission process (due to the increased kinetic energy as the dynodes progress). The multiplied secondary electrons from the last dynode are then collected by the anode. Figure 3.3 shows the cross section of a PMT.

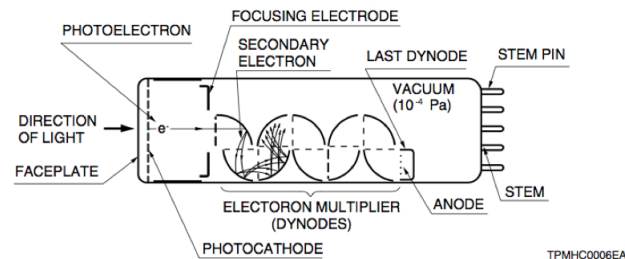


Figure 3.3. Cross Section of a PMT. (Hamamatsu 2010)

Each VERITAS telescope contains a camera in the focal plane consisting of 499 PMTs. The angular spacing of the PMTs is  $0.15^\circ$ , providing a  $3.5^\circ$  diameter field of view (Holder 2006). Light cones are positioned in front of each PMT to improve photon collection and reduce the detection of off-axis background photons. In 2012, the existing PMTs were replaced with new high-quantum efficiency (high-QE) PMTs (Hamamatsu R10560, QE > 32 %; Kieda 2011). Figure 3.4 shows the VERITAS camera with the high-QE PMTs installed.

A multichannel modular commercial power supply provides the high voltage for the PMTs, and allows each PMT to be controlled individually. The high voltage is chosen to give each PMT a gain of  $\sim 10^5$ . A high-bandwidth preamplifier integrated into the PMT base amplifies the signal. Typical currents are  $3 \mu A$  for dark field and  $6 \mu A$  for bright fields (Holder 2006),

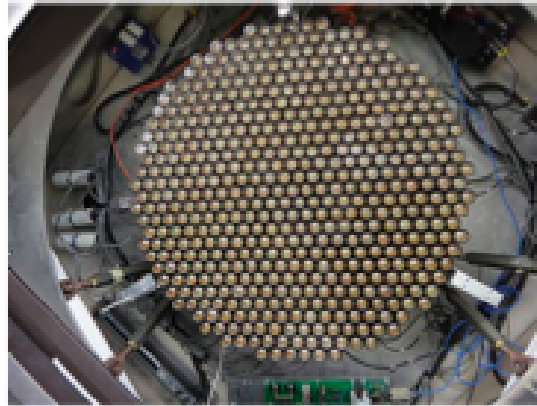


Figure 3.4. The VERITAS Camera. (Kieda 2013)

### 3.4 Other Peripheral Devices

Several other devices make up the telescopes in the VERITAS array.

- Three infrared cameras (two mounted on telescopes 2 and 4, and one mounted on one of the trailers) detect temperature changes in the atmosphere in order to monitor cloud cover.
- A pointing monitor system that includes eight charge-coupled device (CCD) cameras, two on each telescope.
- A custom-built light-emitting diode (LED) flasher system.

### 3.5 The VERITAS Trigger System



VERITAS employs a 3-stage trigger system to reduce the detections of fluctuations in the night sky background (NSB) events and other spurious events such as those caused by the detection of local muons. The trigger system consists of:

**Level One (Pixel) Trigger.** The level-one trigger (L1) is a pixel-wise trigger that fires once the signal in an individual PMT crosses a certain threshold (generally 50 mV).

**Level Two (Pattern) Trigger.** Within all telescopes, each of the 499 L1 outputs a 13 ns wide emitter-coupled logic (ECL) pulse. Then a pattern trigger system, the level-two trigger (L2), uses the relative timing and the distribution of L1 triggers within the camera to remove events that do not arrive in clusters. When first developed, the L2 trigger registered neighboring pixels that had an overlap time of  $\sim 6$  ns (Weinstein 2007). The L2 trigger was upgraded in November 2011 and is now capable of time-aligning individual pixels to within  $\sim 0.2$  ns, allowing for an operational pixel-to-pixel coincidence window of  $\sim 5$  ns. This reduced coincidence window improves night sky background (NSB) event rejection, and effectively lowers the energy threshold (Zitzer 2013).

**Level Three (Array) Trigger.** The level-three (L3) trigger, the *array-wise multiplicity trigger*, is used to identify events that are consistent with the simultaneous observation of air showers across multiple telescopes. The L3 fires if multiple telescopes pass the L2 trigger requirement within a coincidence window of 50 ns. Custom-built VMEbus (VME) modules, the Pulse Delay Module (PDM), the Sub-Array Trigger (SAT) Board, and a commercial VME GPS clock make up the L3 trigger. The SAT board performs the majority of the critical array trigger function. It converts the arrival times of the delay-corrected L2 signals into digital time-stamps via 1.25 ns resolution time-to-digital converters (TDCs) and buffers them (Weinstein 2007). The L3 coincidence logic is performed in the central control building and re-

ceives information from the L2 trigger systems from each telescope via optical fibers using custom built Digital Asynchronous Transceiver modules (DATs).

The L3 also tags the event with supplementary information such as event number. This information along with additional event information such as GPS timestamp is recorded in a *First in, First out* method (FIFO). The FIFO is polled and the results are sent to another software process, *the Harvester*, which binds together the array trigger and telescope-level information into complete events (Weinstein 2007). Figure 3.5 shows the VERITAS trigger system.

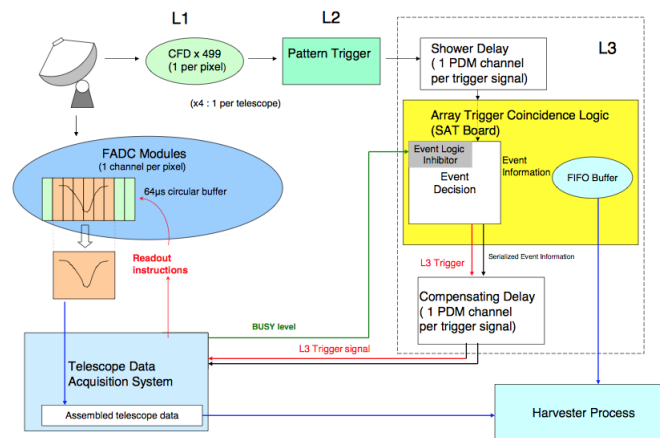


Figure 3.5. The VERITAS Trigger System. (Weinstein 2007)

### 3.6 VERITAS Data Acquisition

VERITAS employs a multi-stage data acquisition process that includes the readout of flash analog-to-digital converters (FADCS), the construction of telescope events and the compilation of various data sets into array-level information. The VERITAS data acquisition system includes a custom-built FADC system that digitizes the PMT signal and participates in the channel-level triggering discussed in the previous section. The VME Data Acquisition (VDAQ) serves as the interface for five VME crates, four of which contain the FADCS, and one that serves as an auxiliary

crate housing a specialized clock-trigger module and a GPS clock (Hays 2007).

In order to increase the dynamic range of the FADCs, each channel employs a *low-gain* delay line and threshold switch. At the input point, each PMT signal is split into three copies: one is delayed and reduced by a factor of 6, one is sent to a threshold discriminator (*HiLo discriminator*), and one is fed directly into the digitizer. If the signal that reaches the digitizer is beyond the range of the PMT, then the low-gain signal is fed into the digitizer.

During read-out the following information is recorded by the data acquisition system:

- The 500 buffered traces
- The L1 trigger pattern
- The HiLo discriminator pattern
- Event information from the L3
- The local GPS timestamp

### 3.7 Event Construction and Compilation

A 48 ns trace accounts for a 3880 byte event fragment that is collected and buffered until they reach a size of 8 MBytes. The buffer is then sent to the telescope *Event Builder*, a program responsible for combining the event fragment from the 5 VME crates to produce telescope events. These events are then written to a local disk and sent to the Harvester, a single eight-core machine that collects data from all telescopes in real-time, including data from the L3 trigger. Once a run is complete, the Harvester creates a single file using the VERITAS Bank File (VBF) data format.

The VBS file groups telescope events together and gives the user immediate access to information on the event as well as data from the array trigger (Hays 2007).

### 3.8 Calibration

VERITAS PMTs and optical reflectors must be monitored periodically to ensure optimal performance and to provide accurate inputs to detector simulation used in the VERITAS analysis. VERITAS PMTs undergo relative and absolute calibration with nightly *flasher runs* and periodic ( $\sim$ month) single-photon and quantum efficiency measurements. VERITAS mirrors are aligned once per season and monitored with monthly calibration of the VERITAS pointing monitor (VPM). In addition, mirror reflectivity is measured every few months.

**Relative Gains.** The relative calibration of VERITAS PMTs is done by a flat fielding process in order to equalize the response of the PMTs. Relative gain measurements are taken by illuminating the entire collection of PMTs with a custom-built LED flasher and diffuser. Each time the PMTs are illuminated, a monitor measures the intensity of the flasher and the corresponding signal measured by the PMT. A 3-minute *flasher run* includes 6700 8-step intensity ramps to provide sufficient statistics. Figure 3.6 shows the relative gains in a VERITAS camera and the Gaussian distribution of these gains.

**Absolute Gains.** The *absolute gain* is an estimate of the signal that results when an incoming photon enters the PMT. For the purpose of VERITAS analysis, there are two metrics that are used to understand the absolute gain. The first metric is determined by estimating the *quantum efficiency* of the PMTs. The second metric is obtained by estimating the signal from a single photoelectron.

The *quantum efficiency* signifies the probability of photoelectron emission when a single photon strikes the photocathode of the PMT. In practice this is mea-

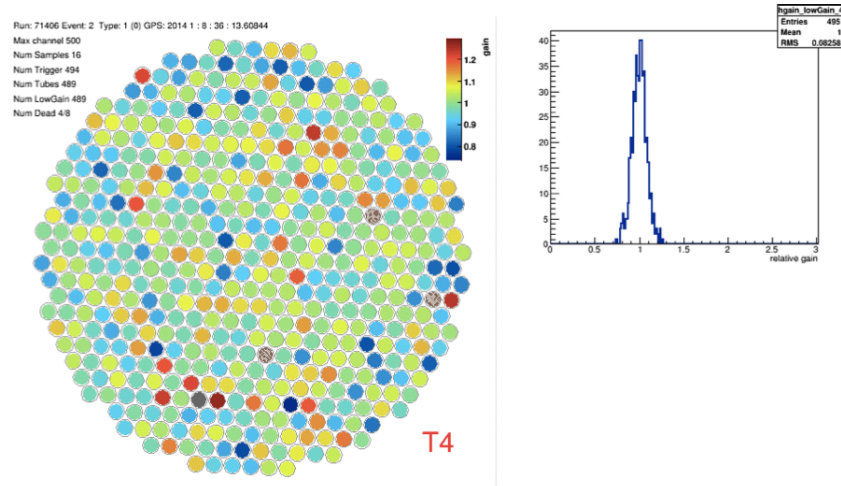


Figure 3.6. Relative Gains and their Gaussian Distribution. (Meier 2014)

sured by determining the ratio of output electrons for an incoming photon. This specification is provided by Hamamatsu (Hamamatsu 2010); however, this estimate is periodically tested by the VERITAS collaboration.

The single photo-electron (PE) measurement estimates the number of digital counts that corresponds to a single photo-electron hitting the first dynode of the PMT. This measure is made every few months by placing a plate with small holes in it (*the holey plate*) in front of the camera and illuminating the camera with faint flashes from the LED source. When a photon hits the holey plate, the majority of the time no photo-electrons are released from the cathode of the PMT; on rare occasions, a single photo-electron is released and the PMT response is recorded. Figure 3.7 shows the holey plate (left) and the charge distribution obtained by the single PE measurement (right).

**Optical Reflectivity.** VERITAS mirrors experience degradation ( $\sim 3\%$  loss in reflectivity per year at 320 nm; Roache et al. 2008) due to weathering. Optical reflectivity measurements are done on an annual basis by selecting 4 mirrors from three areas (top, bottom, and middle) of the reflector. On-site testing is done using

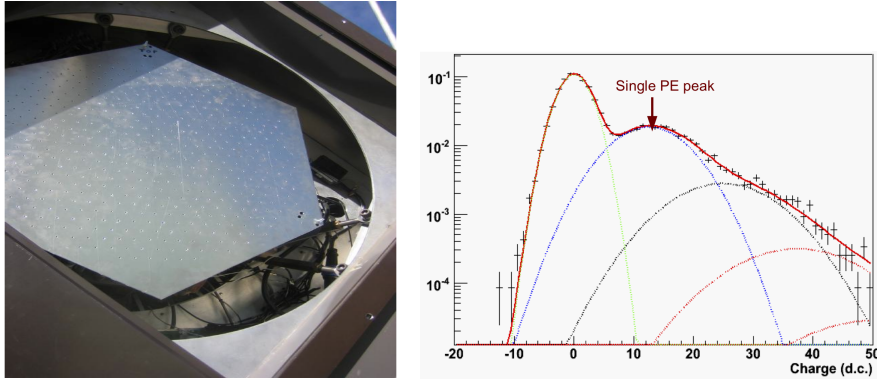


Figure 3.7. Single PE Calibration Tools. (Meier 2014).

a broad spectrum light source, an adjustable filter wheel and a photometer (Roache 2008). Figure 3.8 shows a series of mean reflectivity measurements from different areas of T1's reflector from 2009 to 2012. The black line shows the mean reflectivity for the newly coated mirrors installed in 2008.

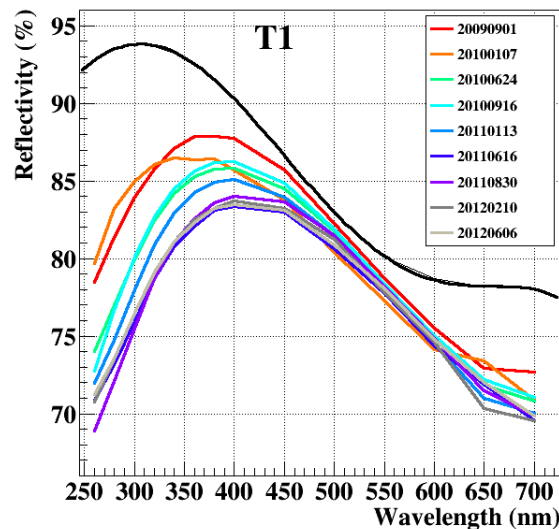


Figure 3.8. Reflectivity Measurements. (Courtesy of Emmet Roache)

**Optical Alignment.** The mirrors on the VERITAS reflector must be periodically aligned, primarily due to the fact they are removed and reinstalled to undergo reflectivity tests. The optical alignment procedure for the VERITAS mirrors is done

using a CCD camera that acquires images of the mirrors as the telescope scans a grid of points centered in the direction of a bright star. Figure 3.9 shows the optical alignment apparatus mounted on the VERITAS camera. **A** indicates the digital camera; **B**, a  $45^\circ$  mirror that allows the virtual image from the camera to be located in the telescope's optical axis at the prime focus of the reflector; **C** a positional stage; **D**, the cable connecting the apparatus to the data acquisition computer.

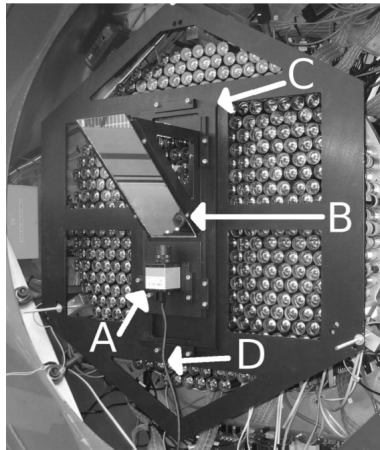


Figure 3.9. Optical Alignment Apparatus. (McCann et al. 2009)

At each point in the scan, the camera registers the amount of light from each of the individual mirrors. Well-aligned mirrors produce the brightest image of the star when the telescope is pointed directly at the star. For misaligned mirrors, the star appears brightest when the pointing direction of the telescope relative to the star is exactly twice the angle of misalignment (McCann et al. 2009). Figure 3.10 illustrates these concepts by showing the on-axis pointing of the telescope (left) and the off-axis pointing of the telescope used to determine the angle of misalignment (right).

The following section will describe how observations taken by the VERITAS instrument are processed and used in the VERITAS analysis chain.

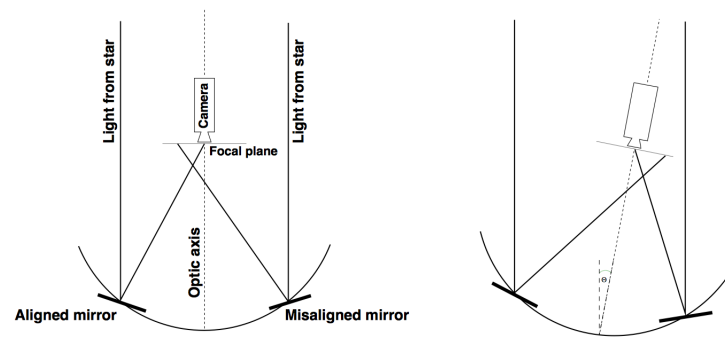


Figure 3.10. Optical Alignment Diagram. (McCann et al. 2009)



## CHAPTER 4

### VERITAS DATA ANALYSIS

Data generated by the VERITAS array consists of digitized pulse signals from the PMTs, GPS clock timestamps, and various trigger information. To analyze the recorded Cherenkov events, the VERITAS data analysis chain requires *parameterizing* the camera image, *reconstructing* the air shower, and from that information estimating the energy spectrum and significance of the detection.

There are a number of analysis tools used to perform the various stages of VERITAS analysis. For this analysis, the *Eventdisplay* software package was used to perform all stages.<sup>3</sup> This section describes the stages of the VERITAS analysis chain. Figure 4.1 shows the structure of the Eventdisplay analysis package (Maier 2014).

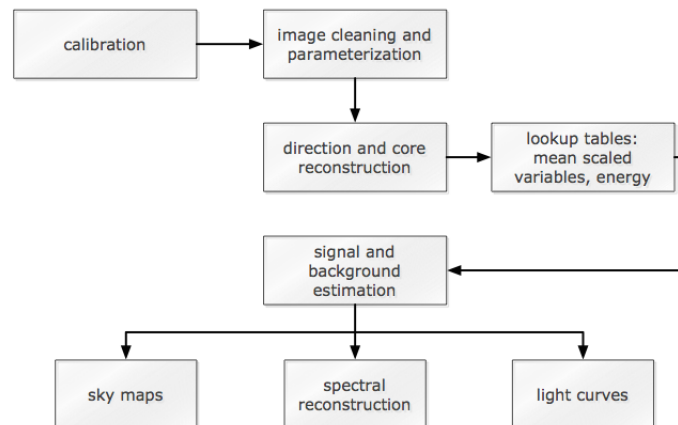


Figure 4.1. Structure of the Eventdisplay Analysis Tool. (Maier 2014)

#### 4.1 Trace Summation

The first step in the VERITAS analysis chain involves determining the charge measured by each pixel. This is done in a multi-stage process that involves first

<sup>3</sup>Eventdisplay was largely developed by Gernot Maier, DESY, Zeuthen and Jamie Holder, University of Delaware with contribution from a large number of VERITAS collaborators

estimating *pedestals*. The night sky background (NSB) is highly variable, and even when Cherenkov events are not being detected, each PMT registers a response to this background light. In order to account for this, *pedestals* are calculated for each pixel. Pedestals are estimates of the PMT signals in the absence of a Cherenkov event. To estimate these values, the L3 system artificially triggers the readout at a rate of 1 Hz, and the results are divided into 3 minute time bins. For each 3-minute period, a mean pedestal value is calculated for each pixel. These pedestal values provide a baseline above which Cherenkov events are estimated. In addition, the standard deviation of the pedestal values in each pixel, for each three minute bin, is also calculated. This quantity, the *pedvar*, is a measure of the amount of noise in the pixel and is used in later steps of the analysis chain.

## 4.2 Double Pass Method

Once pedestal events are calculated, actual triggered events are analyzed using their FADC traces. Eventdisplay analyzes FADC traces using the *double pass method* (Holder 2005). In the first stage, a wide summation window is used to look at the pulse over a 36 ns time period ( $\sim 18$  2-ns samples). The *Tzero* value, the point at which the trace rises to half of its maximum value, is obtained. The mean value of *Tzero* for each pixel is calculated and compared to the mean value of *Tzero* across all pixels. A time gradient is calculated by comparing all *Tzero* values across the camera, and a timing offset is calculated for each channel. Figure 4.2 shows the distribution of *Tzero* values (pulse arrival times) for a sample air shower (in units of 2-ns FADC samples; Holder 2005). The distribution of arrival times is a result of photons that are generated at different points along the shower axis resulting in differences in path lengths to the camera (Heßa et al. 1999).

In the second stage a smaller summation window (6 2-ns samples) is placed on every trace of the sample, with a starting point based on the time gradient determined

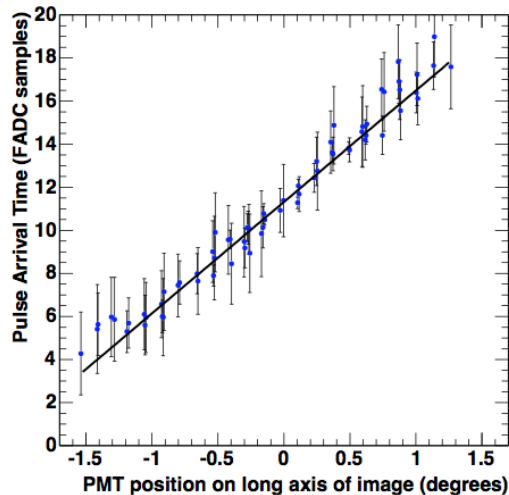


Figure 4.2. Sample Air Shower Tzero values. (Holder 2005)

by the first stage. This smaller window helps to provide a better signal-to-noise ratio while minimizing signal loss. The FADC trace is then summed to get the total charge registered by the pixel, and then the mean pedestal values are subtracted. This *pedestal-subtracted charge* is the value that is used throughout the analysis to estimate the total charge in each pixel. Figure 4.3 shows two FADC traces: Temporal pulse profile generated by a Cherenkov event (left) and fluctuations about a PMT pedestal in the absence of a Cherenkov event (right). That dashed line represents the pedestal value.  $T_0$  is the arrival time estimated by the point at which the trace rises to half of its maximum value. The shaded area represents a 12 sample summation window.

### 4.3 Image Cleaning

The next step of the VERITAS analysis chain involves removing all of the pixels that are deemed to be unrelated to the Cherenkov image. *Fixed threshold* cleaning consists of removing pixels that have a signal below a given threshold. However, the method used for this analysis relies on the *pedvar*. In the first step, in order to select pixels with high signal-to-noise ratios, each pixel with a charge greater than 5 times

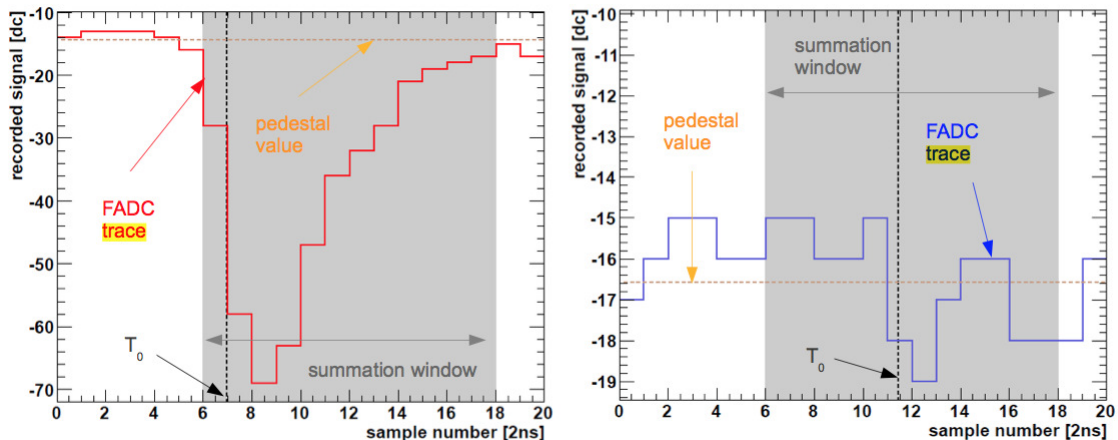


Figure 4.3. Two FADC Traces. (Prokoph 2013)

its pedvar is selected. These pixels are called *image pixels*. Next, a lower threshold of 2.5 times the pedvar is used for pixels that neighbor *image pixels*. If the pixel fulfills this requirement it is labeled a *border pixel* and is kept as part of the shower image. If an image pixel does not have any neighboring pixels that survive the cleaning process it is removed. The resultant *image* and *border* pixels make up the complete shower image. Figure 4.4 shows the total charge in each pixel in one of the VERITAS cameras before image cleaning (left) and after image cleaning (right). In the figure at right, pixels with low signal-to-noise ratios and pixels with no neighboring pixels that meet the threshold requirements have been removed.

#### 4.4 Image Parameterization

Once a complete shower image is recorded and cleaned, the image is then *parameterized*. The original parameterization of  $\gamma$ -ray initiated air showers was done by Michael Hillas (1985). Hillas described extensive air showers using 6 parameters to describe the shape and orientation of the shower as seen by IACT cameras. During the image parameterization stage, the shower image is approximated by an ellipse. The semi-major and semi-minor axes reflect the length and width parameters while

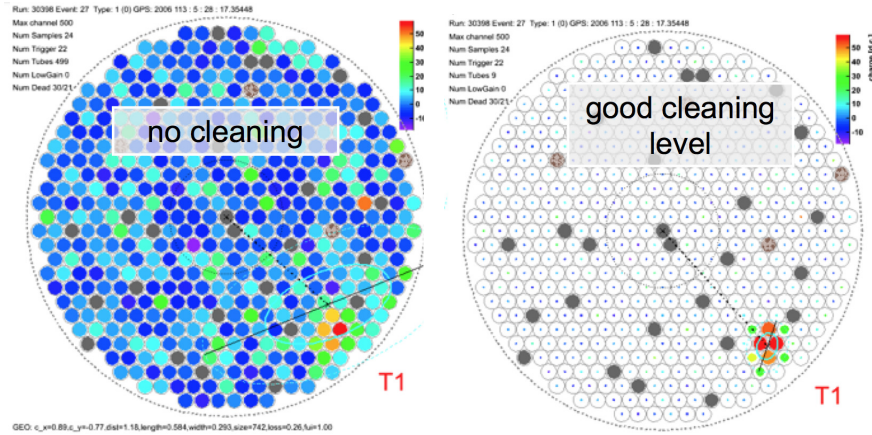


Figure 4.4. VERITAS Camera Image Before and After Cleaning. (Maier 2014)

the alpha, miss, and azwidth relate to the orientation of the image. The distance parameter measures the distance of the image centroid from the center of the camera's field of view. Figure 4.5 shows the geometry of the original Hillas parameters.

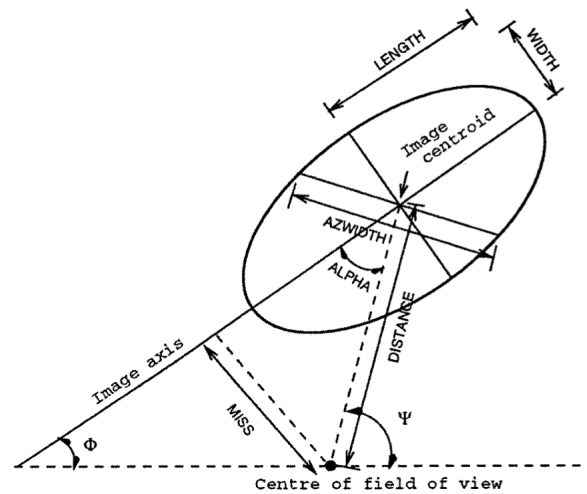


Figure 4.5. Original Hillas Parameters. (Fegan 1997)

The original Hillas parameters have been continually updated and modified, and currently there are a number of parameters that may be assigned to shower images depending on the goals of the analysis. The most relevant parameters for this analysis appear in Table 4.1. The following sections describe how these image parameters are

used to make *cuts* on shower images and how they are used to *reconstruct* air showers.

Table 4.1. Commonly Used Air Shower Parameters.

<b>Parameter</b>	<b>Short Description</b>
<i>Width</i>	RMS spread of the light along the minor axis of the image
<i>Length</i>	RMS spread of the light along the major axis of the image
<i>Distance</i>	<i>Impact parameter</i> : Distance between the image centroid and the center of the camera's field of view
<i>Size</i>	<i>Total brightness</i> (in digital counts); calculated by summing the charge in each of the image pixels
<i>NTubes</i>	Total number of photomultiplier tubes that make up the shower image
<i>Loss</i>	The total fraction of the total <i>size</i> of an image contained in the outermost pixels
<i>Alpha</i>	<i>Image orientation</i> : The angle between the major axis of the image and a line joining the image centroid to the center of the field of view
<i>Size Second Max</i>	The <i>size</i> of the second brightest image across all telescopes that detected the event

## 4.5 Quality Cuts

Before an image is reconstructed, quality cuts are applied to decrease background events and ensure that only higher quality camera images are obtained. For example, to decrease the number of background events and triggering due to standard fluctuations, it is useful to require that the image is made up of a minimum number of pixels ( $NTubes$ ) and has a certain brightness in digital counts (d.c.;  $Size$ ). It is also useful to cap the number of image pixels on the outer edge of the camera ( $Loss$ ) to ensure that the majority of the air shower event was recorded. Additionally, some requirement in the number of telescopes that observed an event is included. Table 4.2 shows the quality cuts used for this analysis.

Table 4.2. Image Quality Cuts.

minimum number of tubes $\geq 5$
minimum size $\geq 1200$ d.c.
minimum loss cut $\leq 0.2$
minimum number of telescopes $\geq 3$

## 4.6 Event Reconstruction

Following the algorithms of Hofmann et al. (1999), the arrival direction and core location of the shower are estimated stereoscopically. The arrival direction of the shower can be estimated by projecting multiple images of the shower on the same plane and calculating the intersection point of the major axes. The shower core location corresponds to the position on the ground that the initial  $\gamma$ -ray photon would have struck if not absorbed by the atmosphere. This point is estimated by projecting the shower image recorded by each telescope onto the ground plane. The arrival direction and core location estimates are weighted by  $size$  and ratio of width-over-length for each image to give more weight to brighter, more elongated images. The intersection estimates are also weighted by the sine of the angle between the two images, as

lines with acute intersection points have a larger error in their intersection estimates (Hofmann et al. 1999). The height of the shower maximum can be estimated with the formula:

$$H = r / \tan(\theta) \quad (4.1)$$

where  $r$  is the distance between the telescope and the reconstructed shower core and  $\theta$  is the angle between the image centroid and the reconstructed arrival direction.

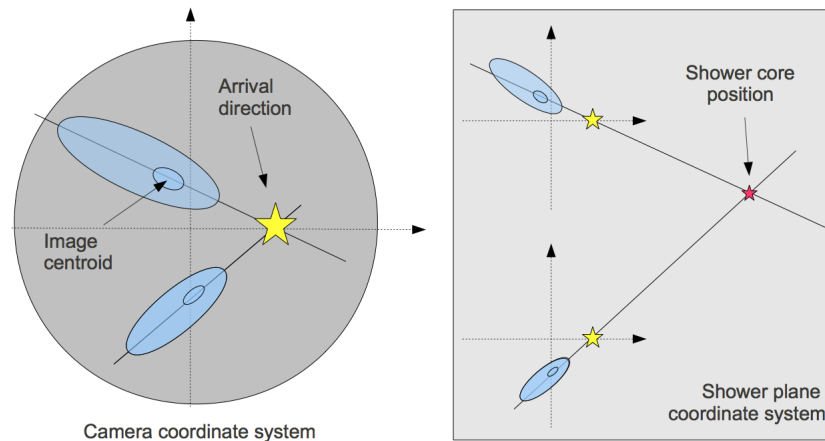


Figure 4.6. Arrival Direction and Shower Core Position. (Prokoph 2013)

## 4.7 Energy Estimation

The number of Cherenkov photons generated by an air shower is closely tied to the energy of the primary gamma-ray (see Section 2.1). This suggests that the image *size* can provide an energy estimate for the shower. However, the *size* recorded by the camera is a function of observing conditions, particularly the shower direction and the *impact parameter*, the distance from the shower core to a given telescope. The recorded image is also a function of the NSB level, as the level 1 trigger and cleaning thresholds influence the recorded size. To cover this large parameter space, *look-up tables* (LUTs) are generated using detailed Monte Carlo (MC) simulations.

The first step in generating energy LUTs involves simulating  $\gamma$ -ray initiated



air showers and the resulting Cherenkov photons (CORSIKA, see Section 2.3). Air showers are simulated over a radius of 750 m from random azimuthal direction and discrete zenith angles. The simulated  $\gamma$ -rays are assumed to have a power law distribution with a spectral index of 2. The resultant Cherenkov photons are then traced to their impact point assuming an atmospheric transmission efficiency based on the U.S. 1976 standard atmosphere (COESA 1976) and local radiosonde measurements (Daniel 2008). From these simulations the arrival direction, impact position and wavelength of each Cherenkov photon is estimated.

Next, the Cherenkov photons are put into a detector response model to simulate their propagation through the VERITAS reflector and camera. The detector model to accounts for:

- The wavelength-dependent reflectivity of the VERITAS mirrors
- The optical alignment of the VERITAS reflectors
- The shadowing of the reflector by the quadrupod arms and camera housing
- The collection efficiency of the light cones
- The quantum efficiency of the VERITAS photomultiplier tubes
- The efficiency and response of the VERITAS trigger and FADC digitizers

From the air shower and detector simulations, resulting camera image are estimated. Simulations are analyzed exactly as are the real data. Multiple analysis are completed for several sky brightnesses (NSB) levels.

Look-up tables are then generated by estimating the energy that corresponds to a given *size*, core location, and zenith angle. In order to assign greater weight to

energy events from narrow distributions, the energy estimate for the event is obtained by weighting each telescope's estimate:

$$E_{\text{event}} = \frac{\sum_{i=1}^N E_i / \sigma_i^2}{\sum_{i=1}^N 1 / \sigma_i^2} \quad (4.2)$$

where  $N$  is the number of telescopes and  $\sigma$  is the standard deviation of the energy estimate.

Figure 4.7 shows LUTs for the median (left) and the standard deviation (right) energy for simulated events. This *slice* of the table shows the results of air showers simulated for a  $20^\circ$  elevation angle and a noise level similar to that of the Crab Nebula field of view (FOV).

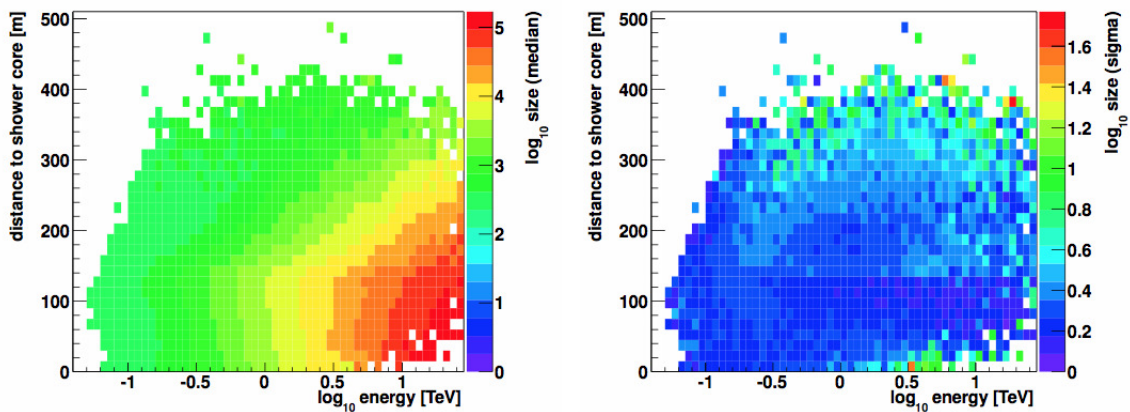


Figure 4.7. Energy Look-up Tables. (Prokoph 2013)

## 4.8 Gamma/Hadron Separation

Once all of the events have been parameterized, and the arrival direction, core location, and energy have been estimated,  $\gamma$ -ray events are separated from the large background of cosmic ray (CR) events. This is done by exploiting the fact that CR-initiated showers are less compact and more irregular. *Expected parameters* for  $\gamma$ -ray events are calculated to help identify those events most likely to result from  $\gamma$ -rays.

Like the simulations performed for the energy estimation, expected parameters are estimated by simulating air showers, varying *size* ( $s$ ), core distance ( $R$ ), zenith angle ( $\Theta$ ), and NSB level. Expected lengths,  $\langle l(s, R, \Theta) \rangle$ , and widths,  $\langle w(s, R, \Theta) \rangle$  are calculated based on the images simulated in the camera after modeling the VERITAS detector. For each event, the *mean-scaled length* (MSCL) and *mean-scaled width* (MSCW) are then calculated:

$$\begin{aligned} \text{MSCL} &= \frac{1}{N} \sum_{i=1}^N \frac{\text{length}_i - \langle l(s, R, \Theta) \rangle}{\sigma_{\text{length}, MC}(s, R, \Theta)} \\ \text{MSCW} &= \frac{1}{N} \sum_{i=1}^N \frac{\text{width}_i - \langle w(s, R, \Theta) \rangle}{\sigma_{\text{width}, MC}(s, R, \Theta)} \end{aligned} \quad (4.3)$$

where  $N$  is the number of telescopes, and  $\sigma_{MC}$  corresponds to the standard deviation of the simulated lengths and widths provided by the MC analysis.

Mean-scaled values for  $\gamma$ -ray initiated events peak at zero, while CR events generally create longer, wider images in the camera that result in greater mean-scaled values. Figure 4.8 shows the distribution of mean-scaled parameters from an analysis of the Crab Nebula (Prokoph 2013). The y-axis shows the number of events. The black dots denote reconstructed events. The peak around zero results from  $\gamma$ -ray events. The red curve shows the events that arise from the CR background. These hadron-initiated showers create camera images that are longer and wider.

#### 4.9 Signal vs. Background Estimation

Once cuts have been made using image shape parameters, the CR background is greatly reduced. The background events that remain are due to  $\gamma$ -ray-like cosmic ray events, CR events whose mean-scaled parameters are similar to those of  $\gamma$ -rays. One of the most powerful background discriminator is the  $\theta^2$  cut. The parameter  $\theta$  is defined as the angle in the sky between the known source position and the

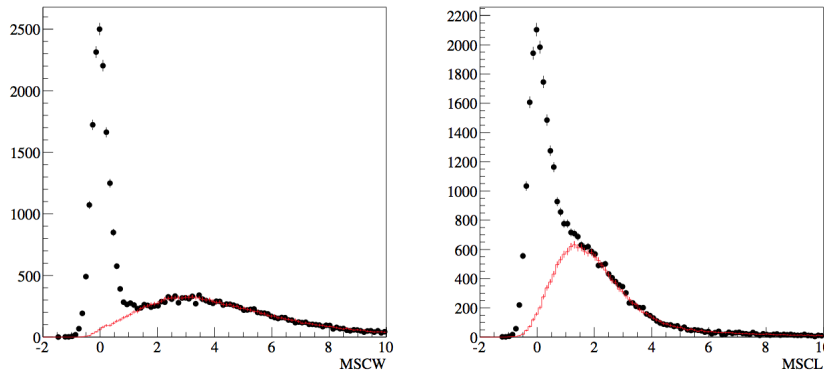


Figure 4.8. Distribution of Mean-scaled Parameters. (Prokoph 2013)

position reconstructed in the earlier stages of the analysis. For a standard point source analysis  $\theta^2 < 0.008 \text{ deg}^2$ . However, this value was adjusted for this analysis based on sensitivity studies (see Section 6.3).

CR background events that remain after the applied cuts are estimated by defining ON and OFF regions on the *sky map*. An ON region, or a  $\theta^2$  region, is defined by a region of radius  $\theta$  that is centered on a potential gamma-ray source. An OFF region is a region that does not include the potential gamma-ray source. In Eventdisplay, an OFF region is estimated by one of two methods: the reflected-region or the ring-background method. Figure 4.9 shows ring (left) and reflected-region (right) background models (Berge et al. 2007).

The reflected-region background model was developed for use with *wobble mode* observations. *Wobble mode* refers to observations where the center of the FOV of the telescope is at a position slightly offset from the source. For typical VERITAS observing runs, the wobble offset is set to  $0.5^\circ$  and the direction is alternated between north, south, east, and west.

Wobble mode observations allow for the definition of *reflected regions* as seen in Figure 4.9. The ON region is reflected with respect to the FOV center of the

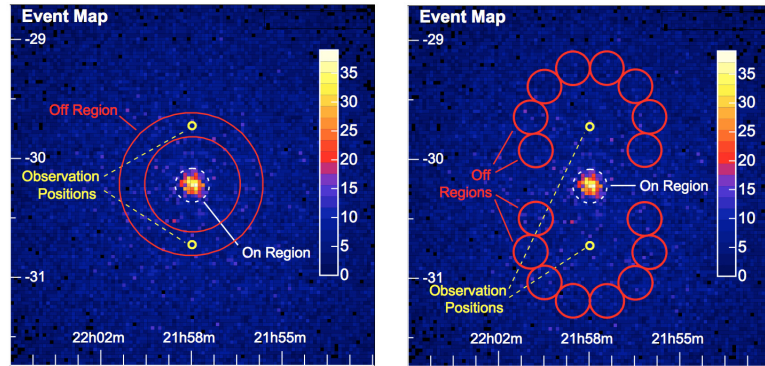


Figure 4.9. Ring and Reflected-region Background Models. (Berge et al. 2007)

camera. OFF regions are defined by several circular regions equidistant from the pointing region, avoiding an area close to the ON region to prevent contamination by  $\gamma$ -ray events. Operating under the assumption that the camera's response is radially symmetric, OFF regions are the same distance from the center of the camera so no correction due to the camera's acceptance is needed.

The ring background method models an annulus around the source position (in celestial coordinates) and uses this ring-shaped region to provide a background estimate. Within the ring, the acceptance cannot be assumed to be constant since the ring covers areas with different offsets from the observation position. Therefore, this method requires the definition of an acceptance correction function.

The size of the ON region (the signal region) is estimated by defining the parameter,  $\theta$ , the angle between the reconstructed event direction and the direction of the candidate source. The maximum allowed value for this angle defines a  $\theta^2$  region. Signal and background events are counted if they fall within the given  $\theta^2$  region. The size of the  $\theta^2$  region is chosen based on the characteristics of the source. A small *exclusion region* is defined around the signal region to prevent poorly reconstructed  $\gamma$ -ray events from populating the background regions.

## 4.10 Statistical Significance

The statistical reliability of a  $\gamma$ -ray source detection must be analyzed in the framework of Poisson statistics to understand the probability that the count rate excess in an expected region is due to an actual source and not background fluctuations. The fact that the background is not exactly known provides one of the biggest challenges in estimating the statistical significance of  $\gamma$ -ray astronomy experiments. Li and Ma (1983) developed the procedure to estimate the significance of VHE  $\gamma$ -ray detections and tested the results with Monte Carlo simulations.

First, Li and Ma defined:

- $N_{on}$ : The total number of  $\gamma$ -ray photon counts in the signal region (*on-source* region)
- $N_{off}$ : The total number of  $\gamma$ -ray photon counts in background regions (*off-source* regions)
- $\alpha$ : The ratio of the size of the on-source region to the size of the off-source region

Approximating the number of background photons included in the on-source counts as:

$$\hat{N}_B = \alpha N_{off} \quad (4.4)$$

The signal detected in the on-region is then defined as:

$$N_S = N_{on} - \hat{N}_B = N_{on} - \alpha N_{off} \quad (4.5)$$

Figure 4.10 shows typical  $\gamma$ -ray count rates.

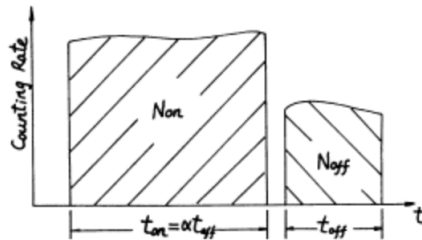


Figure 4.10. Typical  $\gamma$ -ray Counting Rates. (Li & Ma 1983)

Gamma-rays are counted in regions defined as *on* and *off*. Assuming on-source counts and background counts are independent measurements, the variance in the signal is given by:

$$\sigma^2(N_S) = \sigma^2(N_{on}) + \sigma^2(\alpha N_{off}) = \sigma^2(N_{on}) + \alpha^2 \sigma^2(N_{off}) \quad (4.6)$$

Using a maximum likelihood estimation, the standard deviation can be approximated by:

$$\sigma(\hat{N}_S) = \sqrt{\hat{\sigma}^2(N_{on} + \alpha^2 \hat{\sigma}^2(N_{off}))} = \sqrt{N_{on} + \alpha^2 N_{off}} \quad (4.7)$$

where  $\hat{\sigma}^2$  is the maximum likelihood estimate of the variance. Defining the significance,  $S$ , as the ratio between excess counts and its standard deviation:

$$S = \frac{N_s}{\hat{\sigma}(N_s)} = \frac{N_{on} - \alpha N_{off}}{\sqrt{N_{on} + \alpha^2 N_{off}}} \quad (4.8)$$

However, Li and Ma found that this prediction, derived from simple Poisson statistics, deviates significantly from Monte Carlo simulations for  $\alpha \neq 1$ , in part because it does not first assume that any signal in the ON region is due only to background counts (Li and Ma 1983). By applying a statistical hypotheses test (likelihood ratio method) and comparing the results with Monte Carlo simulations, Li and Ma (1983) have shown that this uncertainty is better characterized by:

$$S = \sqrt{2} \left\{ N_{on} \ln \left[ \frac{1 + \alpha}{\alpha} \left( \frac{N_{on}}{N_{on} + N_{off}} \right) \right] + N_{off} \ln \left[ (1 + \alpha) \left( \frac{N_{off}}{N_{on} + N_{off}} \right) \right] \right\}^{\frac{1}{2}} \quad (4.9)$$

Eventdisplay applies this calculation in estimating the significance of a detection. For a significant detection of a  $\gamma$ -ray source, a 5 standard deviation significance ( $S \geq 5$ ) is generally required.

#### 4.11 Spectral Reconstruction

To estimate an energy spectrum of a source, it is necessary to understand the telescope's energy-dependent response. This is done by estimating the *effective area* of the telescope and considering corrections due to the telescope's dead time. The *effective area* of the telescope is the efficiency by which the telescope detects  $\gamma$ -rays. In later stages of the analysis it plays an important role in that it allows the count rate estimated by the detector to be converted into a measured flux from a  $\gamma$ -ray source. To estimate the effective area, simulations are used to understand the number of  $\gamma$ -ray showers predicted to be detected by the telescope over a range of energies. To get an estimate of this efficiency,  $\gamma$ -ray-initiated air showers are simulated over a 750 m radius and an energy range of 30 GeV to 250 TeV and put through the detector response model.

The *effective area* is given by:

$$A_{\text{eff}} = \frac{N(E)}{T(E)} A_0 \quad (4.10)$$

where  $N(E)$  is the number of simulated events passing selection cuts for an energy,  $E$ ;  $T(E)$  is the total number of events simulated for an energy,  $E$ ; and  $A_0$  is the area (in the shower plane) over which  $\gamma$ -ray events are simulated, or *thrown*. For a simulation consisting of  $\sim$ million air shower events, typically just 2-3 % will trigger the simulated detector and only 0.5-2 % will pass cuts (Maier 2013). Figure 4.11 shows the number of showers in a simulated spectrum compared to the number of showers that remain after applying cuts (left), and the effective area as a function of energy (right) (Maier 2013). The Eventdisplay analysis eliminates many of the lower-energy ( $< 1$  TeV) and higher-energy ( $> 10$  TeV) showers through cuts placed



on *size* and *loss* respectively. It should be noted that effective areas are dependent on a number of observing parameters including zenith and azimuthal angle, pointing offset, and NSB level. The VERITAS array has a fairly uniform response for  $\sim$  TeV  $\gamma$ -rays.

The energy threshold is defined using one of two methods. The first method defines the threshold as the energy at which the maximum number of  $\gamma$ -rays is detected after applying cuts, as shown in Figure 4.11. The second method relies on calculating the energy resolution (based on LUTs), and determining the point at which the energy bias reaches a certain level. The reason a larger energy bias is seen at low energies is due to the fact that only upper fluctuations in air shower brightness are recorded by the telescopes once images become very faint.

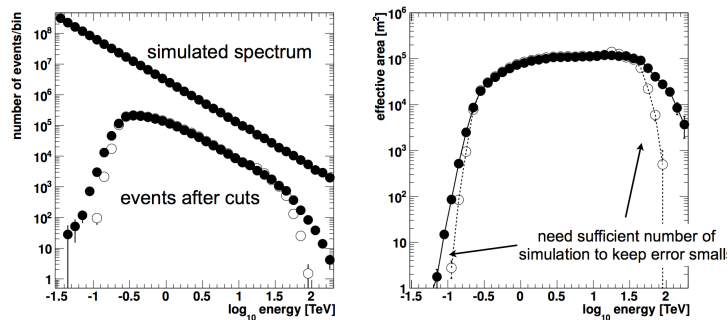


Figure 4.11. Effective Area Derivation. (Maier 2014)

## 4.12 Flux Measurement

To obtain a flux estimate, the number of  $\gamma$ -rays reconstructed in each energy bin must be corrected for the effective area (see Section 4.11) and dead time (see Mohanty et al. 1998). The dead-time is determined by the time it takes the telescope to read out information on events ( $\sim 400 \mu\text{s}$ ; Weinstein 2007). The array dead time scales with the L3 trigger rate, reaching 6-8% at 150-170 Hz, and 10-11% at 225 Hz (Weinstein 2007).

Starting from a measured count rate, the differential energy spectrum is defined as the number of excess events detected per unit area per unit time:

$$\frac{dF(E)}{dE} = \frac{N_{\text{excess}}(E)}{A_{\text{eff}}(E)T_{\text{obs}}dE} \quad (4.11)$$

where  $N_{\text{excess}}$  is the number of excess events,  $T_{\text{obs}}$  is the dead-time corrected observation time,  $A_{\text{eff}}$  is the effective area, and  $dE$  is the width of the energy distribution binning. To combine multiple observations, the excess in each observation is weighted by the time and effective area over which it was estimated:

$$\frac{dF(E)}{dE} = \frac{\sum_{i=0}^n N_{\text{excess}}^i(E)}{\sum_{i=0}^n A_{\text{eff}}^i(E)T_{\text{obs}}^i dE} \quad (4.12)$$

where  $i$  is the index for  $n$  observation runs.

This calculation is complicated by the fact that the effective area ( $A_{\text{eff}}$ , as a function of reconstructed energy) depends on the assumed spectral slope. To correct for this, the effective area is adjusted for the fitted spectrum and then re-fit, repeating until the fit converges (Aharonian et al. 2006). This assumes that the spectral shape can be adequately described by a power law, which is typically a valid assumption. The later sections of this work detail the Eventdisplay analysis that was performed for the starburst galaxy M82.

CHAPTER 5  
DIFFUSE VHE  $\gamma$ -RAY PRODUCTION IN M82



Figure 5.1. M82. (NASA, ESA, & Hubble Heritage Team)

VERITAS has detected VHE  $\gamma$ -rays from over 40 objects including active galaxies, supernova remnants, pulsar wind nebulas, and binary systems. Among the most notable objects detected by VERITAS is M82, a starburst galaxy located approximately 3.6 Mpc from the earth (Freedman et al. 1994) in the direction of Ursa Major. M82 is one of the closest and best studied examples of its class, and it is the only object of its kind detected by the VERITAS array (Acciari et al., 2009; Fermi LAT detection: Abdo et al. 2010). Recently discovered to be a late type barred spiral galaxy (SBc; Mayya et al., 2005), its proximity and favorable inclination ( $i=81^\circ$ ; Lynds & Sandage 1963) make it one of the most studied objects across numerous wavelengths. The closest Type-Ia supernova observed in decades, SN 2014, was observed in the galaxy in January of 2014. Figure 5.1 shows an image of M82 (four color filters from visible to IR & hydrogen filaments). Bright infrared emission due to dust heated by early-type stars is visible from the galaxy's core. Superwinds due to starburst activity can be seen streaming off of the galactic plane.

This section provides an overview of some of the remarkable features of the galaxy, with a focus on those features that influence the production of diffuse  $\gamma$ -ray emission. Table 5.1 shows some of the relevant properties of M82. In addition, this section briefly describes the models that explain the production of VHE diffuse emission.

### 5.1 Overview of the Starburst and Starburst Core

While there is no strict definition of a starburst galaxy, and a complete description of the starburst mechanism is still an active area of research, starburst galaxies are generally identified by their remarkable star-forming characteristics. As the name suggests, starburst galaxies are experiencing periods of increased star formation over a relatively short timescale (relative to the lifetime of the galaxy), and starburst activity is generally localized to a circumnuclear region ( $\sim 10^2$  pc wide), fueled by an accumulation of dense molecular gas.

In the case of M82, evolutionary synthesis modeling suggests that starburst activity occurred in two successive episodes, each lasting a few million years, most likely due to a gravitational interaction with the nearby galaxy M81. During this encounter, material was funneled into the core of M82 creating a burst of star formation. Figure 5.2 show the asymmetrical neutral hydrogen (21-cm HI) distribution in the M81 group (Yun et al. 1995). A tidal bridge extends between M82 (top) and M81 (center). It is estimated that within the core of M82 stars are formed at a rate (SFR)  $\sim 10 M_{\odot} \text{ yr}^{-1}$  (Förster Schreiber et al. 2003; Milky Way SFR  $\sim 1 M_{\odot} \text{ yr}^{-1}$ , Robitaille & Whitney 2010).

The nuclear starburst region of M82 extends approximately 500 pc in diameter and contains  $\sim 10^8 M_{\odot}$  of star forming material, including a high concentration of molecular gas (Förster Schreiber et al. 2001; Sofue, 1998). At optical wavelengths,

Table 5.1. Properties of the Starburst Galaxy M82.

Property	Value	Reference
Coordinates (J2000)	RA 09h 55min 52s   Dec +69° 40' 47"	Skrutskie et al. 2006
Apparent Visual Magnitude	8.4 mag	Dale et al. 2007
Apparent Visual Dimension	$11.2 \times 4.3$ arcmin	Dale et al. 2007
Distance	3.6 Mpc	Freedman et al. 1994
Inclination	$81^\circ$	Lynds & Sandage 1963
Molecular Hydrogen Gas Density ( $n_{H_2}$ )	$(1-6) \times 10^4 \text{ cm}^{-3}$	Naylor et al. 2010
IR Luminosity	$3 \times 10^{10} L_\odot$	Telesco & Harper 1980
Star Formation Rate	$\sim 10 M_\odot \text{ yr}^{-1}$	Förster Schreiber et al. 2003
Supernova Rate	$\sim 0.1 \text{ yr}^{-1}$	Rieke et al. 1980
Wind Velocity	600 km/s	Strickland et al. 1997

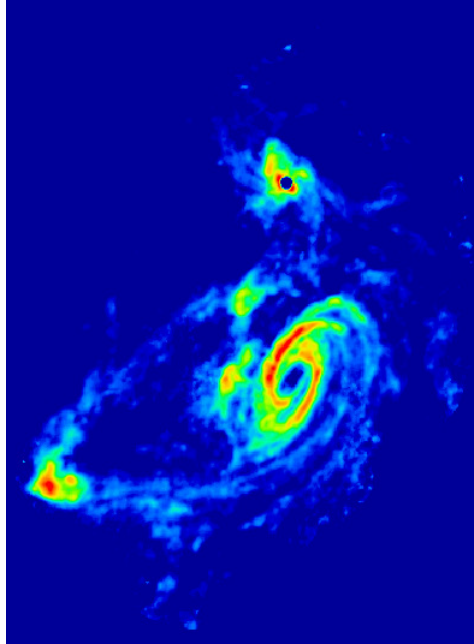


Figure 5.2. Neutral Hydrogen Gas Structure of the M81 Group. (Yun et al. 1995)

the galaxy's core is extremely complex. Dozens of “knotty structures” are distributed throughout the central regions, separated by a large central dust lane and many other smaller dust lanes throughout the region. Even the brightest knots suffer considerable extinction but approximately 50 semistellar objects are visible at optical wavelengths. The objects are most likely young, compact star clusters (O’Connell & Mangano 1978).

M82 is extremely luminous at infrared (IR) wavelengths. The central star-forming region of M82 is approximately 5 times more luminous than the entire Milky Way (Lester et al. 1990). The majority of the luminosity is due to thermal IR radiation resulting from dust heated by early-type stars associated with star formation (Rieke et al. 1980, Lester et al. 1990). The central starburst region emits the majority of the IR emission (Telesco & Harper 1980), and optical and IR observations have revealed numerous high-luminosity star clusters (Lipsy & Plavchan 2004). Figure 5.4 shows seven defined star-forming clusters (circles). Magenta crosses mark the

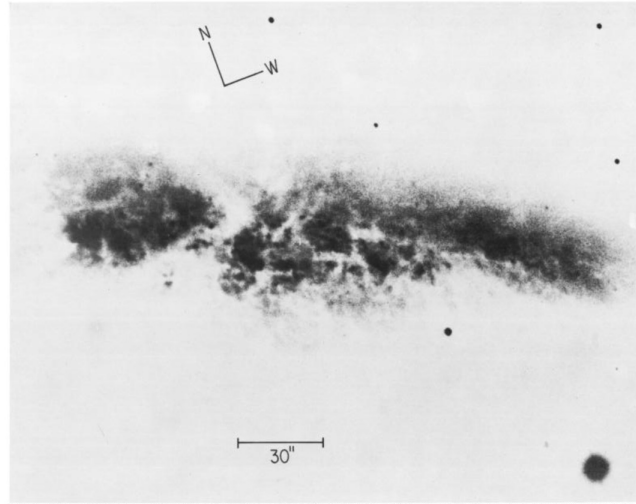


Figure 5.3. Photographic Plate of M82. (O'Connell & Mangano 1978)

position of nonthermal radio sources and red squares mark HII regions (Lipsy & Plavchan 2004).

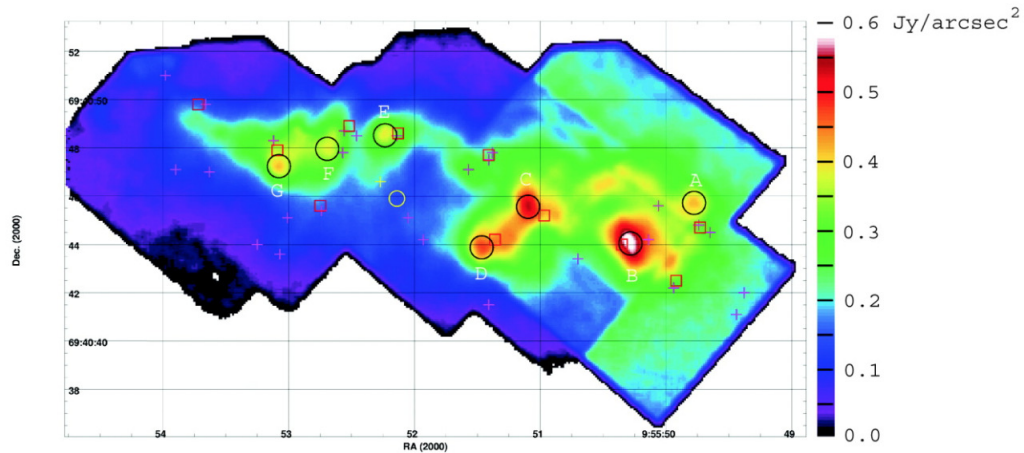


Figure 5.4. M82 at Mid-IR Wavelengths. (Lipsy & Plavchan 2004)

Radio observations reveal other compact features located in the central kpc of the galaxy (Kronberg & Wilkinson 1975, Fenech et al. 2008). Radio emission results from non-thermal synchrotron emission due to the acceleration of particles in supernova, and also thermal free-free emission from HII regions (Condon 1992). Observations of SNR are supported by evolutionary synthesis modeling that predict

high supernova rates, as a large population of high mass stars complete their main sequence evolution (Rieke et al. 1980). It is estimated that the starburst core of M82 has a supernova rate  $\sim 0.1 \text{ yr}^{-1}$  (Rieke et al. 1980, Kronberg & Wilkinson 1975, Antonucci & Ulvestad 2006; Milky Way SN rate  $\sim 0.019 \text{ yr}^{-1}$ , Diehl et al. 2006). Figure 5.5 shows the SN remnants (diamonds), HII regions (triangles), and various unclassified sources (circles) detected by the Multi-Element Radio Linked Interferometer Network (MERLIN). SNR are identified by their shell-like structure and expansion between observing epochs (Fenech et al. 2008).

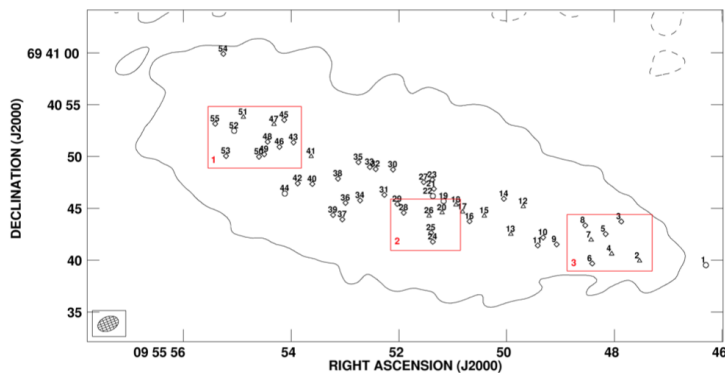


Figure 5.5. Discrete Radio Sources in the Core of M82. (Fenech et al. 2008)

These objects in the galaxy’s core contribute to galactic scale mass outflows driven by the collective effects of supernovae and massive stars. These *superwinds* are created when the energy of the ejecta is converted into thermal energy via shocks. The collective action creates a “bubble” of very hot ( $10^8 \text{ K}$ ) gas that expands rapidly in the direction of the steepest pressure gradient (the minor axis of the galactic disk). These *superwinds* sweep material from the galaxy’s core, propagating away from the core at speeds up to several thousand km/s (Heckman et al. 1993). Figure 5.6 shows images of the superwind at varying scales. The bottom image shows the large scale structure of the superwind crossing the disk of the galaxy and extending  $\sim 6 \text{ kpc}$  off of the galactic plane (Strickland et al. 1997), while the top image shows localized



points of emission (Subaru Telescope Facility 2011).

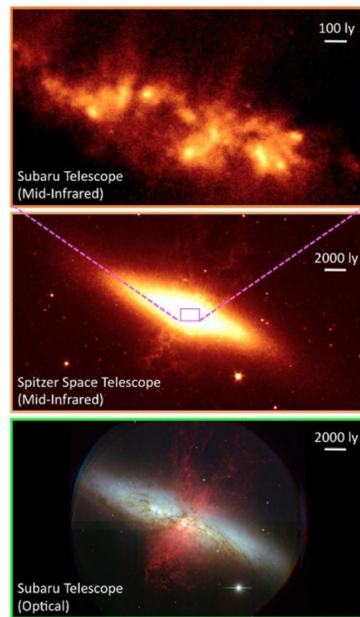


Figure 5.6. The Superwind of M82. (Subaru Telescope Facility 2011)

## 5.2 Diffuse VHE $\gamma$ -ray Production in M82

The source of M82's diffuse VHE emission remains uncertain. The H.E.S.S. detection of NGC 253 is consistent with point-like emission from the central optical regions of the galaxy ( $3\sigma$ , 2.4 arcminute angular extent; Abramowski et al. 2012). However, the small apparent dimensions of M82 make it difficult to attribute the emission solely to the central core of the galaxy.

The extent to which individual sources contribute to the VHE detection is also unknown. A number of sources clustered along the galactic plane of the Milky Way have been shown to emit VHE radiation, including supernova remnants (SNR), pulsar wind nebulae (PWNe), and unidentified sources with no radio or x-ray counterpart. These observations of the inner disk of the Galaxy show strong VHE emission from several regions that have associations with young pulsars (Aharonian et al. 2005). Pulsar wind nebulae show hard spectra and long TeV lifetimes, and high TeV lu-

minosities from starburst galaxies could be explained with PWNe, despite diffusive escape of CRs from the starburst core (Mannheim et al. 2012). Pulsar wind nebulae cannot be ruled out as contributors to the detected  $\gamma$ -ray background in M82, and the level of contamination from discrete unresolved sources remains uncertain.

The observed CR spectrum within our own galaxy is consistent with models that account for the bulk of the CRs through supernovae and theories of diffusive shock acceleration have been broadly applied to a range of shock conditions (*Supernova Paradigm*; Baade & Zwicky 1934; CR Acceleration: see Appendix A). This is supported by recent detections that confirm the existence of very efficient CR acceleration mechanisms in the shock fronts of supernovae. Observations of M82's diffuse  $\gamma$ -ray emission can be explained with similar SN-driven models.

### 5.3 Diffuse VHE $\gamma$ -ray Emission Modeling

Once particles leave sites of acceleration, they produce broadband diffuse emission as they interact with interstellar matter and fields. CR electrons are affected by a number of loss processes including ionization and adiabatic losses. Electrons produce bremsstrahlung emission due to interactions with the dense gas, and infrared (IR) photons serve as targets for inverse Compton scattering. Synchrotron emission dominates at x-ray wavelengths but are negligible at higher energies (Persic et al. 2008). Protons produce  $\gamma$ -ray radiation primarily via neutral pion decay. Diffuse emission models account for these process and account for primary particles as well as secondaries. They also account for factors such as dust emissivity and IR photon density which is used for a target for inverse Compton scattering and for lower frequency radiation (*Q-Diffuse*; see Torres 2004).

Diffuse emission models lack the detail of single source modeling and assume the core of M82 acts as one accelerator and injector of cosmic rays. At sufficiently high

energies, the  $\gamma$ -ray spectrum is determined by the proton emissivity. The injection spectrum is given by:

$$Q_{\text{inj}}(E_{\text{kin}}) = K(E_{\text{kin}})^{-p} \exp(-E_{\text{kin}}/E_{\text{cut}}) \quad (5.1)$$

Where  $E_{\text{kin}}$  is the kinetic energy of the proton,  $p$  is the power index, and  $E_{\text{cut}}$  is the cut-off energy for the accelerated particles. Assuming a collection of uniformly-distributed SNR within the inner region of the starburst, the normalization,  $K$ , is found by estimating the total energy transferred from supernovae to CRs within a given volume:

$$\int_{E_{\text{kin},\text{min}}}^{E_{\text{kin},\text{max}}} Q_{\text{inj}}(E_{\text{kin}}) E dE_{\text{kin}} = \text{NPR}/V \quad (5.2)$$

where  $N$  is the fraction of the SN power transferred into CRs ( $\sim 10\%$ ),  $P$  is the SN explosion power ( $P \sim 10^{51}$  erg),  $R$  is the SN rate ( $\sim 0.1 \text{ yr}^{-1}$ ), and  $V$  is the volume of the starburst core ( $r \sim 10^2$  pc).

To account for all of the processes that affect the particles as they traverse the galaxy, models must follow this primary injection spectrum and estimates losses and secondary production as particles diffuse or are convected out of the starburst region into the outer disk and halo. This is done using diffusion-loss equations. For a distribution of particles  $N(E)$ , the diffusion loss equation is given by (Ginzburg & Syrovatskii 1964):

$$\frac{\partial N(E)}{\partial t} = D \nabla^2 N(E) + \frac{\partial}{\partial E} [b(E)N(E)] + Q(E) - \frac{N(E)}{\tau(E)} \quad (5.3)$$

where  $D$  is the scalar diffusion coefficient,  $Q(E, x, t)$  is the rate of particle production, and  $\tau(E)$  is the confinement timescale. The confinement timescale of the protons must take into account diffusion, convection (due primarily to stellar winds), and

pion production losses:

$$\tau^{-1}(E) = \tau_D^{-1} + \tau_c^{-1} + \tau_{pp}^{-1} \quad (5.4)$$

where  $\tau_D$  is the diffusion timescale,  $\tau_c$  is the convection timescale and  $\tau_{pp}$  is the pion loss timescale. The energy-dependent diffusion timescale,  $\tau_D$ , is on the order of 10 Myr but a range of values may be considered (see de Cea del Pozo et al. 2009). The time scale for convection,  $\tau_c$ , is generally assumed to be on the order of  $r/v_w$  where  $r$  is the radius of the region and  $v_w$  is the collective wind velocity. The pion loss timescale is approximated by:  $t_{pp}^{-1} = (dE/dt)_{pion}/E$  (see Appendix B, de Cea del Pozo et al. 2009).

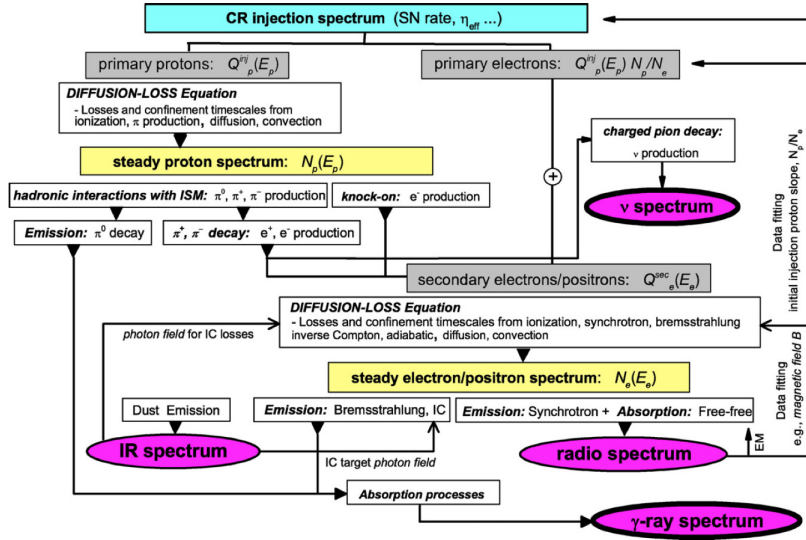


Figure 5.7. Code Flow of *Q-Diffuse*. (de Cea del Pozo et al. 2009)

Figure 5.7 shows the flow of *Q-Diffuse*, a model used to predict multiwavelength spectra by solving the full set of diffusion-loss equation for protons and electrons simultaneously (de Cea Del Pozo et al. 2009). *Q-Diffuse* provides an estimate of the steady-state distribution of particles and then provides emission estimates by modeling a complete set of interactions within the interstellar medium.

With these diffusion and loss processes it becomes apparent that the  $\gamma$ -ray

luminosity depends on the timescale for pion production and the escape timescale due to diffusion and convection. The idea that protons lose the majority of their energy before escaping is referred to as *proton calorimetry* (Pohl 1994). A great deal of research has been devoted to understanding the degree to which SB galaxies act as calorimeters (e.g. Lacki et al. 2011).

Figure 5.8 shows the predicted  $\gamma$ -ray spectrum from M82, based on modeling the collection of SN remnants in the galaxy's core. The predicted spectrum covers a range of uncertainties in SN rates ( $0.1 \text{ SN yr}^{-1}$  to  $0.3 \text{ SN yr}^{-1}$ ), resulting in the two curves shaded in green. The initial injection spectrum was assumed to have a power law index of 2.1 with an energy cut-off of 100 TeV, and the sensitivity of the model to these parameters was examined in the study. At VHE energies, pion decay dominates the production of  $\gamma$ -rays. Sensitivity curves for various  $\gamma$ -ray detectors are shown as curves (Violet, CTA; yellow, MAGIC; red, EGRET; blue Fermi; de Cea del Pozo 2009).

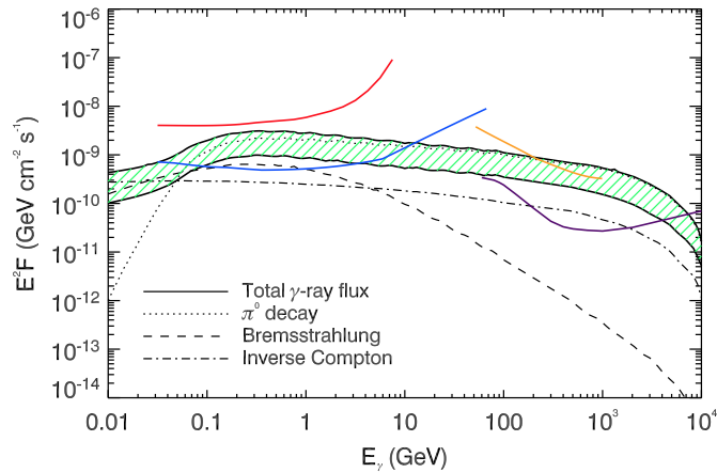


Figure 5.8. Predicted Differential  $\gamma$ -ray Flux. (de Cea del Pozo 2009)

## CHAPTER 6

## VERITAS OBSERVATIONS OF M82

## 6.1 Quality Selection of Observations

VERITAS observations of M82 extend over 6 years, covering 2 telescope configurations and 2 different sets of camera photomultiplier tubes (PMTs). Due to changes in performance and sensitivity, VERITAS data is described by 3 epochs: V4 (original configuration/camera), V5 (new telescope configuration), V6 (high-QE PMTs). Table 6.1 shows the number of quality-selected observing hours from each epoch. The first analysis of the V4 data was published in Acciari et al. 2009. The V5 and V6 data comprise new observations never before analyzed.

Table 6.1. M82 Observations

Epoch	M82 Observations (hrs)
V4: 9/2007 - 9/2009	1/2008 - 4/2009 (142)
V5: 9/2009 - 9/2012	2/2011 - 4/2012 (57)
V6: 9/2012 - Present	2/2013 - 5/2014 (33)

VERITAS observations, known as “runs,” are taken in 20 or 30 minute duration. Runs are monitored nightly to ensure the integrity of the data. The runlist used for this analysis includes only 4 telescope data taken in weather classified by the VERITAS Data Quality Monitoring (DQM) system as A or B weather. C weather runs were inspected to determine usability. Observations taken with malfunctioning hardware were removed. Partial runs were used based on DQM metrics. Figure 6.1 shows a sample output from the VERITAS Run Log Generator. The Run Log Generator sorts runs by source and assigns each run a weather grade based on FIR camera measurements. Comments from observers provide insight into any issues encountered during observations. To complete this analysis, 671 runs were sorted, some manually inspected to ensure quality and capitalize on partial runs.

DATE	RUN	SOURCE	CALIB	UTC	DUR	USE	MODE	SKY	'T1'-FIR CRMS	T3-FIR CRMS	EL	AZ
20130205	66562	M82	1234/2	06:39	30	30 0.5N	A	0.1 (A)	0.1	50	11	
20130205	66563	M82	1234/2	07:12	23	23 0.5S	A	0.1 (A)	0.1	52	8	
20130205	66564	M82	1234/2	07:49	30	30 0.5E	A	0.1 (A)	0.2	52	3	
20130208	66629	M82	1234/1	06:20	35	35 0.5N	B+	0.6 (D)	1.1	50	11	
20130208	66630	M82	1234/1	06:57	35	35 0.5W	B+	1.9 (D)	3.0	51	6	
20130210	66665	M82	1234/1	06:39	30	30 0.5S	A	0.0 (A)	0.1	51	9	
20130210	66666	M82	1234/1	07:11	30	30 0.5E	A	0.0 (A)	0.1	52	5	
20130210	66667	M82	1234/1	07:43	30	30 0.5W	A	0.1 (A)	0.1	52	0	
20130211	66682	M82	1234/1	06:04	30	30 0.5N	A	0.1 (A)	0.1	49	12	

Figure 6.1. VERITAS Run Log Generator Sample Output.

## 6.2 Eventdisplay Analysis

The initial analysis of this data was done using standard cuts developed for Eventdisplay v470. These cuts were created using Crab Nebula data taken at a range of elevations, scaled down to model a weak  $\gamma$ -ray source (1 % Crab Nebula flux). Then optimal cut values for the image parameters were found. The original cuts used were optimized for hard spectrum point sources (*hard cuts*). These cuts results in an energy threshold  $\sim 500$  GeV. Table 6.2 shows the standard hard cuts, which were generally optimized for weak sources, but were not optimized for the V4 epoch at low elevations where the majority of the M82 data was taken.

After processing all seasons of M82 data, these cuts did not produce a significant detection of M82. Table 6.3 shows the results of the original Eventdisplay analysis. A total of 240 hours of observation lead to the detection of 97 excess  $\gamma$ -ray events. In comparison, the original M82 detection recorded 91 excess events from 140 hours of observations (V4 dataset; Acciari et al. 2009).

In order to better understand the non-detection, and also the overall performance of the analysis tool for weak, low elevation sources, a sensitivity study using observations of the Crab Nebula was done (Ratliff & Grube 2015). Crab data obtained over a range of elevations was analyzed using the standard hard cuts. Crab

Table 6.2. Standard Hard Source Cuts.

---



---

Distance of core position to telescope $\leq 350$ m
Distance from camera center $\leq 2.0^\circ$
Angular distance: $\theta^2 < 0.008$ degrees <sup>2</sup>
Mean-scaled width: $-1.2 < MSCW < 0.5$
Mean-scaled length: $-1.2 < MSCL < 0.5$
Size Second Max $> 1600$ d.c.

---

Table 6.3. Summary of  $\gamma$ -ray-like Events using Standard Hard Cuts

---



---

	Hrs	N <sub>ON</sub>	N <sub>OFF</sub>	Excess	Significance
<b>V4</b>	137	299	241	58	3.3
<b>V5</b>	68	131	114	17	1.4
<b>V6</b>	33	124	102	22	2.0
<b>Total</b>	240	554	457	97	4.0

---

observations were divided into low ( $\sim 40$ - $65$  degrees) and high (over  $\sim 65$  degrees) elevation bins. The extracted Crab signal was scaled down (10 % Crab, 1% Crab) to understand the response for weaker sources.

The results demonstrated the decrease in sensitivity for all observing epochs, particularly for low elevation sources. The effects of the relocation of the T1 (V5) and the upgraded PMTs (V6) were seen as the use of these data sets resulted in shorter detection times. However, the V4 data performed particularly poorly, and over half of the VERITAS observations of M82 are comprised of V4 data. These results explained the non-detection of M82, a 0.9 % Crab source observed at approximately 50 degrees elevation. Figure 6.2 shows the results of the sensitivity study for a 1% Crab source. Increased detection times can be seen for observations taken at low elevations. The runlists and full results for this sensitivity analysis are presented in Section C.1.

The results of the sensitivity study provided a test for the performance of the instrument, but the study also demonstrated the need for cut optimization, most



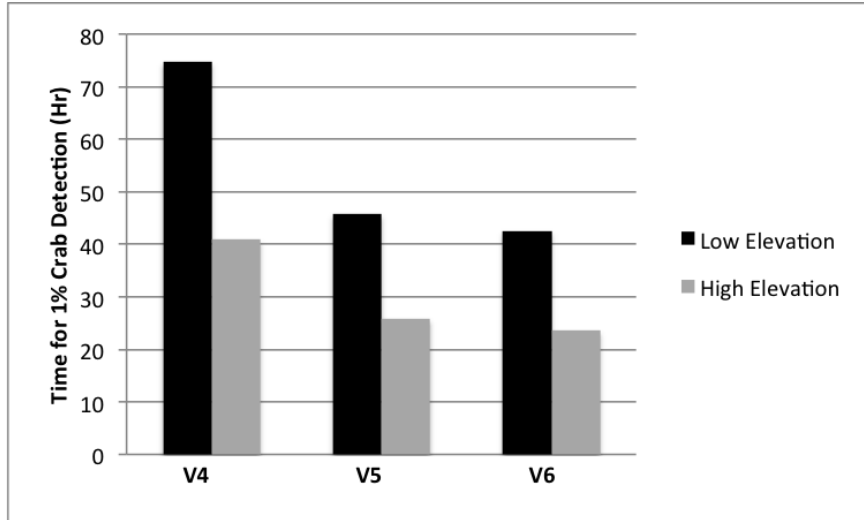


Figure 6.2. Summary of Crab Sensitivity Results.

notably for the V4 data. The next phase of the Crab sensitivity studies involved optimizing cuts using low elevation Crab data. The cut optimization procedure used for this analysis targeted those cuts most likely to affect the analysis of low elevation sources. During this procedure, a cut was varied and Eventdisplay was run on Crab data until the number of hours to a detection was minimized.

The first cut that was studied was the *size second max* cut. New versions of Eventdisplay discriminate events by the size (total digital counts) of an image using this cut. The size second max cut removes events if the second highest size measured by any one telescope does not exceed a given value. This cut was created to ensure that at least two telescopes record bright images, but it was also designed to allow the user to keep the information from smaller sized showers into later stages of the analysis. For the initial analysis a size second max cut of 1600 d.c. was used. Given the weakness of the source and the low elevation effects that create fainter, more difficult to detect air showers, it was unclear if this cut was appropriate. Without extensive studies to rely on and understanding that M82 data might be very sensitive to this cut, we made size cuts using the original definition of *size*. The original size cut

requires a minimum value for each telescope participating in the event (see Section 4.4). If a telescope does not have a high enough size, it is removed from the event. In addition to being better studied, the size cut provides an advantage in that individual telescopes may be cut from the event without the entire event being lost. However, an additional cut requires a certain number of telescope to have recorded the event so this relationship is more complex.

Previous analyses of V4 M82 data have found an optimal size cut of 1200 d.c. (Acciari et al. 2009), and so this was used for the V4 data. Due to the more sensitive PMTs, the V6 data should perform better with a higher size cut; however, our analysis indicated worse sensitivity when raising the size cut. However, these results could be due to insufficient low elevation data ( $\sim 11$  hrs,  $< 60$  degrees elevation). Table 6.4 shows the size sensitivity results with limited V6 data. Based on these results, we found no reason to increase the size cut.

Table 6.4. V6 Size Optimization Results

$\theta^2$	Size	Time for 1% Crab Detection (Hr)
0.015	1200	41.0
0.013	1200	37.0
0.011	1200	39.6
0.015	1300	45.0
0.013	1300	42.6
0.011	1300	45.0
0.015	1400	49.3
0.013	1400	45.8
0.011	1400	48.4

The next cut that was examined was the  $\theta^2$  cut (see Section 4.9). Previous analyses of M82 have demonstrated that looser  $\theta^2$  cuts result in a higher significance. The M82 analysis presented in the original detection (Acciari et al. 2009) found a  $\theta^2$  value of 0.015 to be optimal; however, it was not clear that this value would apply

for V5 and V6 data. In particular, the relocation of the telescope has been shown to improve the reconstruction of the core location, so V5 data could require a tighter  $\theta^2$  cut.

The first attempts at optimizing the  $\theta^2$  cut focused on data taken at elevations lower than 60 degrees to more accurately capture low elevation effects. However, there was a limited supply of Crab data taken at these elevations (7.3 hrs, < 60 degrees elevation), and the optimization was unsuccessful. The observed effects could not be ruled out as statistical fluctuations. Therefore, despite the known effects of elevation on the reconstruction of the air shower parameters, high elevation (60-90 degrees) data was examined out of necessity. Table 6.6 shows the results for the high elevation V5 Crab data. Table C.11 shows the complete list of the 34 high elevation runs used for this analysis. Figure 6.3 shows the  $\theta^2$  plots for V4 (low elevation, left) and V5 (low elevation, right) Crab data. The black lines show the  $\theta^2$  values for  $\gamma$ -ray-like events measured in the ON region. The gray line corresponds to those events measured in the OFF regions. For both V4 and V5 datasets, events from the On regions level out at larger  $\theta^2$  values. These results were used to justify the use of a looser  $\theta^2$  cut with an understanding that additional low elevation data is necessary to better understand this result.

Table 6.5. V5  $\theta^2$  Crab Sensitivity Results

$\theta^2$	1 % Crab Detection (Hr)
0.015	30.0
0.014	38.1
0.013	34.8
0.010	33.5

These studies were used to justify making adjustments to the size and  $\theta^2$  cuts. Table 6.6 shows the optimized cuts used for the final analysis. The following section provides the final Eventdisplay results.

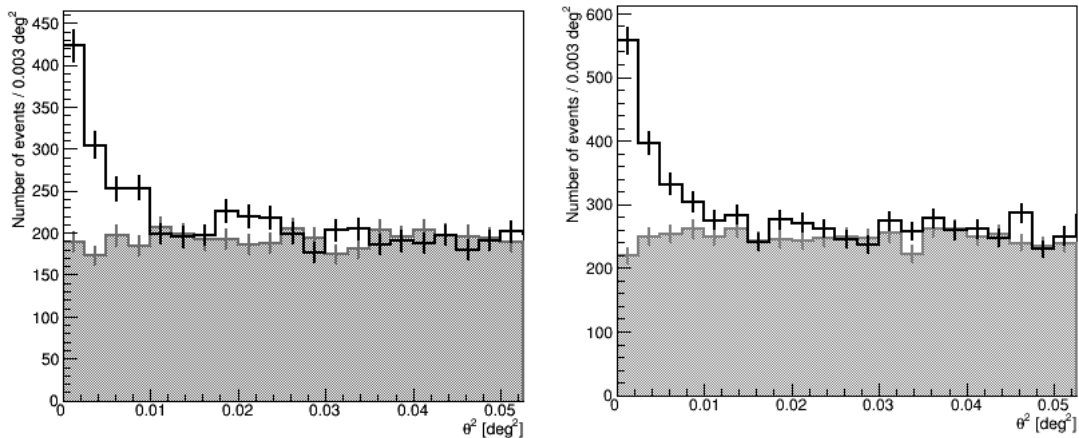


Figure 6.3. V4 and V5  $\theta^2$  Plots from Crab Study.

Table 6.6. Optimized Hard Source Cuts.

---



---

Distance of core position to telescope $\leq 350$ m
Distance from camera center $\leq 2.0^\circ$
Angular distance: $\theta^2 < 0.015$ degrees <sup>2</sup>
Mean-scaled width: $-1.2 < MSCW < 0.5$
Mean-scaled length: $-1.2 < MSCL < 0.5$
Size $> 1200$ d.c.

---

### 6.3 Eventdisplay Results

The final analysis was performed using Eventdisplay version 5dev8, a version very similar to v470 with the addition of several advanced analysis methods that are currently being tested for future work (*3D Model*; Lemoine-Goumard et al. 2006). The reflected region background method was used (see Section 4.9) and the optimized cuts presented in Table 6.6 were applied. Table 6.7 shows a summary of  $\gamma$ -ray-like events determined by this analysis.

The V4 and V5 data showed improved sensitivity with the optimized cuts. The V6 data is notable in that the optimized cuts (primarily optimized on the V4 and V5 datasets) actually decreased the sensitivity. Figure 6.4 shows the significance

Table 6.7. Summary of  $\gamma$ -ray-like Events

	Hrs	$N_{ON}$	$N_{OFF}$	Excess	$\gamma$ -ray Rate ( $min^{-1}$ )	Background Rate ( $min^{-1}$ )	Significance
<b>V4</b>	141.5	203	142.33	60.67	0.007	0.0028	4.4
<b>V5</b>	56.9	71	40.17	30.67	0.009	0.0020	4.0
<b>V6</b>	33.3	78	66.0	12.0	0.005	0.0055	1.3
<b>Total</b>	231.8	352	248.5	103.5	0.007	0.0030	5.7

map of the M82 region. The source region excess and the spatial distribution of the observed excess in background regions is consistent with point-like emission in the direction of M82. The point spread function (PSF) is shown by the black circle.

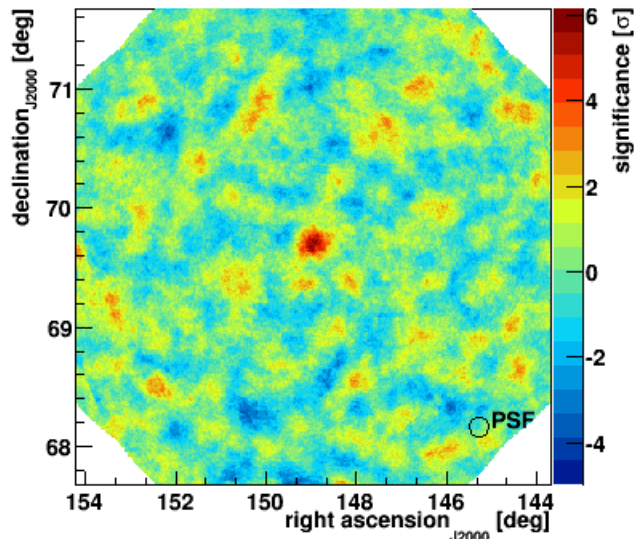


Figure 6.4. Excess VHE  $\gamma$ -ray Events in the M82 Region.

Flux estimates were obtained after effective areas were created by simulating  $\gamma$ -rays and applying the optimized cuts used for this analysis (see Section 4.11). The larger data set provided additional  $\gamma$ -ray events to better constrain spectral properties and to provide enough events to create a higher energy bin (relative to the initial detection). Figure 6.5 shows the M82 spectrum obtained from this analysis fit with a power law model. An upper limit is given for the highest energy bin. Table 6.8 shows  $\gamma$ -ray events by energy. The best fit power law spectral index is  $2.85 \pm 0.38$  with a flux normalization at 1 TeV of  $(2.37 \pm 1.20) \times 10^{-13} \text{ cm}^2 \text{ s}^{-1} \text{ TeV}^{-1}$ .

This analysis allows for the comparison of fluxes across a 6 year span. Variability is not expected in CR-induced diffuse emission model for M82. Consistent with the analysis of Fermi data on smaller timescales (90 days; Ackermann et al. 2012), we do not find significant evidence for variability during our observations ( $\chi^2/\text{dof}=3.26/2$ ).

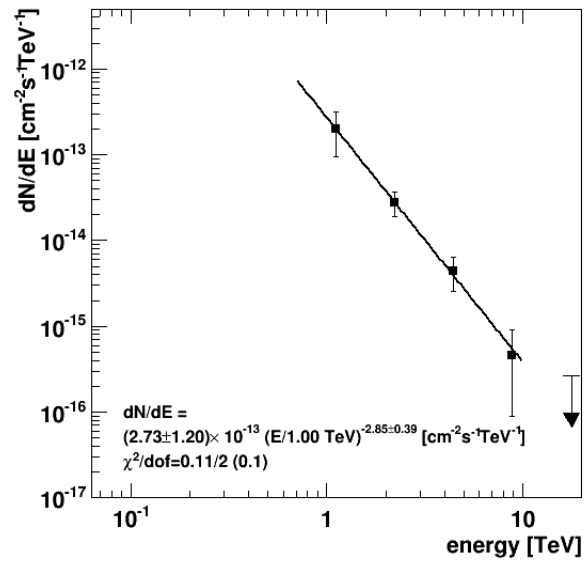


Figure 6.5. M82 Spectrum.

Figure 6.6 shows the VHE light curve for M82. Black points were obtained from this work. The blue point shows the original M82 detection. The decrease in emission observed in the last bin equates to only a 1 sigma effect, and systematic effects cannot be ruled out at this time. Several tests were done to confirm the results of the skymap as well as the flux and spectral results with this set of optimized cuts using Crab Nebula data (see Appendix D).

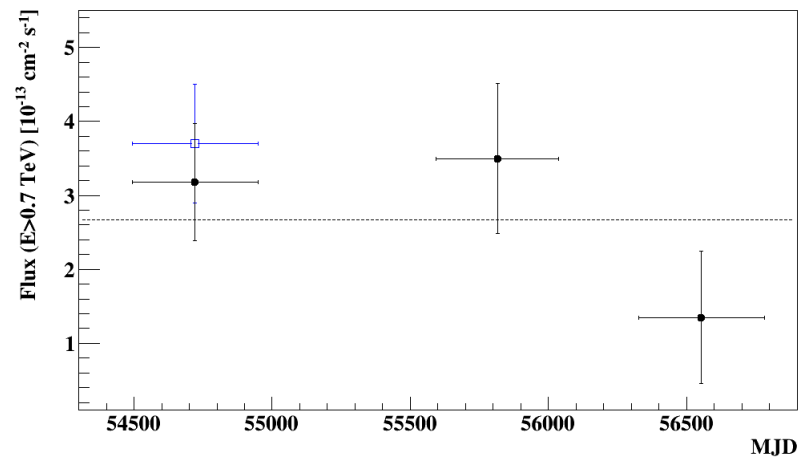


Figure 6.6. M82 Flux Estimates.



Table 6.8.  $\gamma$ -ray-like Events by Energy

Mean Energy (TeV)	Min Energy (TeV)	Max Energy (TeV)	$N_{ON}$	$N_{OFF}$	Excess	Significance
1.122	0.794	1.585	58	43.8	14.1	4.4
2.239	1.585	3.162	92	61.2	30.8	3.5
4.467	3.162	6.310	34	20.57	13.3	2.6
8.913	6.310	12.589	8	0.476	3.24	1.3
17.783	12.589	25.119	1	0.17	0.7	0.8

## CHAPTER 7

### CONCLUSION

VERITAS observations of M82 pose unique challenges. M82 is a source that culminates at low elevations, and it is one of the weakest sources ever detected by the VERITAS array. As confirmed by this study, this combination leads to poor sensitivity when using standard analysis techniques and requires adjustments to quality cuts as well as gamma/hadron cuts to efficiently extract the  $\gamma$ -ray signal. The results of the sensitivity studies performed for this work provide insight into the performance of the Eventdisplay analysis package, a tool that is constantly being refined. These studies are important not only to future analyses of M82, but also to ongoing work to understand and improve the Eventdisplay analysis.

A significant detection of M82 requires exceptionally long observations. For this analysis observations taken over a 6 year period reflect the evolution of the array and require an understanding of the instrument's response over several configurations. In particular, observation obtained after 2012 require an understanding of the effects of the new high-QE PMTs. For our M82 analysis, the V5 optimization led to similar cuts as the V4 data; however, we are just beginning to understand the best way to process the V6 data. High-QE PMTs have the potential to greatly increase photon detection efficiency and lower energy thresholds (Kieda 2013, see Table 7.2), but the data obtained requires an understanding as to how to best make cuts within our analysis tools. Optimization procedures were limited by the lack of data taken at low elevations, particularly for the later telescope configurations. Given the limited supply of V6 data, users are faced with the tradeoff of using higher elevation data to ensure the optimization has sufficient statistics and losing the effects of low elevation. Future work will benefit from an increased V6 data set that will certainly come as the telescope remains in operation.

The results of the sensitivity study and the optimization performed for this analysis provide justification for our choice of cuts. In addition, a range of tests were performed to confirm our results (see Appendix D). However, it is difficult to cross-check our results with other M82 analyses. Table 7.1 shows the results for the standard cuts, the final optimized cuts, as well as the original detection of M82. For the two trials of this work, our analysis results in a post-trial significance of 5.6 sigma. Comparison with the original detection should be applied with caution as these results were produced by another analysis tool, VEGAS, with different cut definitions and values. VEGAS and Eventdisplay are used to confirm each other's results with *secondary analyses*, but these tools are not run with the intention of comparing results on an event level.

Table 7.1. Comparison of Eventdisplay Analyses.

		$N_{\text{on}}$	$N_{\text{off}}$	Excess	Significance
	Original Detection (V4 only)	358	267	91	4.8
This Work	Standard Hard Cuts	554	457	97	4.0
	Optimized Cuts	352	248.5	103.5	5.7
Post-trial Significance: 5.6					

It is also difficult to compare the two trials discussed in this work. There is no straightforward relationship between the size and size second max cuts that were used in our two trials. The optimized cuts result in less events suggesting that our final size cuts removed more low energy events. Table 7.2 shows the energy thresholds for our two sets of cuts. For the V4 and V5 data, our cuts resulted in a higher energy threshold. The V6 data resulted in a lower energy threshold due to the new PMTs. Future studies would benefit from a deeper understanding of the best way to implement size cuts across multiple telescope configurations, particularly for weak, low elevation sources.

Table 7.2. Comparison of Energy Thresholds

V4	Optimized Cuts	1.00 TeV
	Standard Cuts	0.79 TeV
V5	Optimized Cuts	0.88 TeV
	Standard Cuts	0.68 TeV
V6	Optimized Cuts	0.56 TeV
	Standard Cuts	0.56 TeV

A complete understanding of the diffuse VHE emission from M82 remains uncertain. However, VERITAS observations aid in the understanding of CR production and propagation within the galaxy that lead to the production of diffuse emission. The results of this work are consistent with the paradigm in which supernovae (SNe) convert a portion of their mechanical energy into cosmic rays (CRs). Figure 7.1 shows the results of this work along with previous measurements by VERITAS and the Fermi LAT, in comparison with theoretical model predictions (de Cea del Pozo et al. 2009, Blom et al. 1999, Persic et al. 2008). Our measurements are consistent with a broad range of model assumptions and input parameters. For example, the de Cea del Pozo model assumes a 100 TeV energy cut off in the proton spectrum and a range of SN rate values.

Figure 7.1 also demonstrates the need for further modeling to understand this high energy detection. There are currently very few theoretical emission models that describe diffuse  $\gamma$ -ray production up to our detected energy, and this high energy detection is important for understanding, among other things, the physics of diffusive shock acceleration (Fermi I acceleration). Theories of diffusive shock acceleration describe energy cut-offs at which particles reach a maximum attainable energy in supernova shocks due to the finite lifetime of the particle in the shock region and the geometry of the shock (see Appendix A). Estimates cover a very large range of energies (10 GeV to  $10^8$  GeV; see Lagage & Cesarsky 1983, Bell & Lucek 2001,

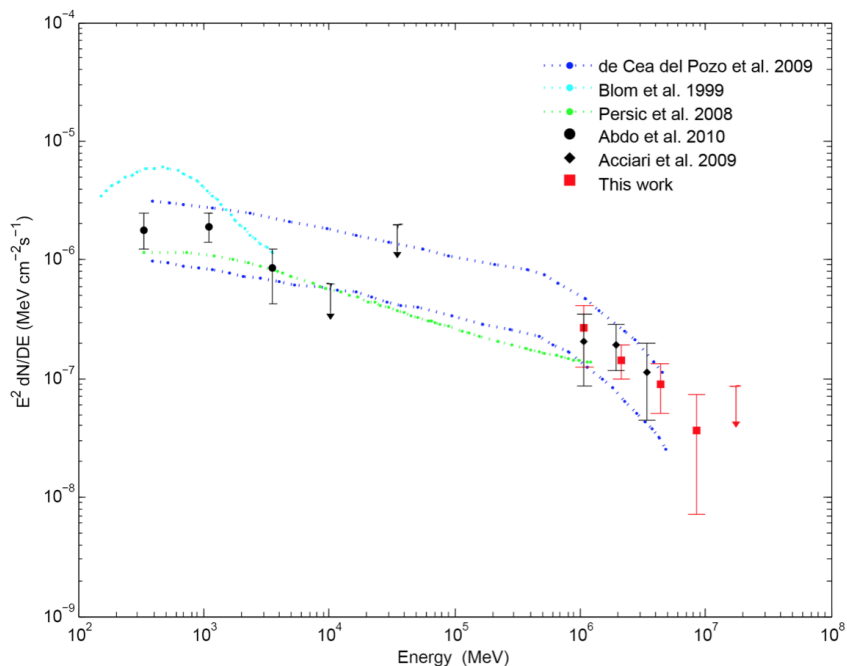


Figure 7.1. M82 Spectral Energy Distribution with Theoretical Predictions.

Blasi et al. 2007). High energy detections test these models by measuring the effects of some of the most energetic particles generated in these shock, and models must begin to accommodate higher energy studies like this one. Along with uncertainties in other galaxy characteristics (e.g. SN rate), there remain large uncertainties in M82 emission model parameters. These results provide additional insight and help to better understand models of CR acceleration and propagation. Detailed treatment of M82 emission mechanisms is needed to understand the implications of a 9 TeV detection, the highest energy detection even obtained for M82.

While these diffuse emission models are considered the most likely explanation for the VHE  $\gamma$ -ray emission from M82, other models account for contributions from discrete sources such as pulsar wind nebula (PWNe; Mannheim et al. 2012). The first detailed calculation (Ohm & Hinton 2012) cannot explain the observed  $\gamma$ -ray spectrum from Fermi to VERITAS energies from a purely PWN-driven source of

CRs. However, a harder PWN  $\gamma$ -ray emission component on top of the diffuse pion decay component cannot currently be ruled out as high numbers of compact objects are expected in the core of starburst galaxies. CTA will have the sensitivity to observe the spectral features associated with this scenario.

M82 was detected at the limit of the VERITAS sensitivity and future improvements in our understanding of diffuse VHE emission will likely come with the introduction of the Cerenkov Telescope Array (CTA). Figure 7.2 shows the simulated sensitivity of CTA compared with the predicted M82 spectrum (tan line). The black data points shows the predicted CTA spectrum after 30 hours of observation. The green line shows the differential sensitivity for one of the proposed CTA configurations. The gray points show the original VERITAS spectrum (Acciari et al. 2009). With a sensitivity increase of a factor of 10, the VHE emission from M82 will be even better constrained, providing a deeper understanding of the diffuse VHE emission from starburst galaxies.

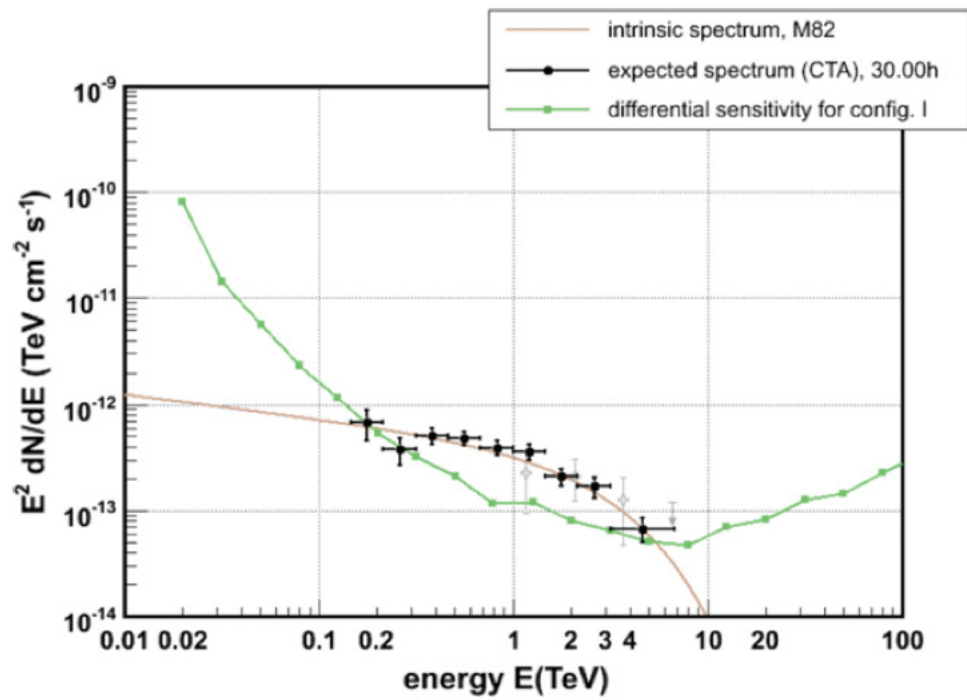


Figure 7.2. Simulation of CTA Observations of M82. (Acero et al. 2013)

APPENDIX A  
FERMI ACCELERATION



First proposed by Enrico Fermi (1949), *Fermi acceleration* originally referred to the acceleration of cosmic particles due to “collisions” against moving irregularities in interstellar magnetic fields. Citing the fact that these magnetic fields have huge dimensions and great stability, Fermi envisioned a scenario in which a particle was injected into the interstellar medium (ISM) and gained energy via multiple collisions against moving magnetic fields. Fermi proposed two types of interactions to describe how charged particles could be accelerated:

- In “Type A” processes, a particle in an irregular magnetic field spirals around a line of force, encounters a stronger field intensity, and as in the case of *magnetic mirrors*, is then reflected back along the same line of force. If the region of high intensity is moving *towards* the particle, the particle will gain energy. Conversely, if the region of high intensity is moving *away* from the particle, the particle overtakes the irregularity before being reflected backward. In this case, the particle will lose energy upon reflection. However, Fermi argued that the net result will be a gain in energy because the relative velocity is larger in the first case, and therefore will occur more frequently.
- In “Type B” processes, the lines of motion of the matter partake in the streaming motion of the particle as shown in figure A.1. In this case, the line of force at the bottom of the curve moves in the directions indicated by arrows a and b. Case a results in a gain of energy while case b results in a loss of energy. Similar to Type A processes, the net result is an increase of energy due to the greater relative velocity.

Fermi expressed the amount of energy gained or lost using a simple argument modeled off of special relativity. In the rest frame of the moving gas, the particle has

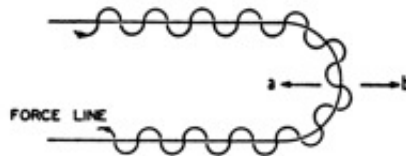


Figure A.1. Type B Reflection of a Cosmic Ray Particle. (Fermi 1949)

total energy:

$$E'_1 = \gamma E_1 (1 - \beta \cos \theta_1) \quad (\text{A.1})$$

where  $\beta = V/c$ ,  $V$  is the velocity of the cloud and  $\gamma = 1/\sqrt{1 - \beta^2}$ . Primes denote the frame of the moving cloud. Figure A.2 shows the schematic of a cosmic ray “scattering” elastically in a magnetic cloud moving with some velocity,  $V$  (Kachelrieß 2008).

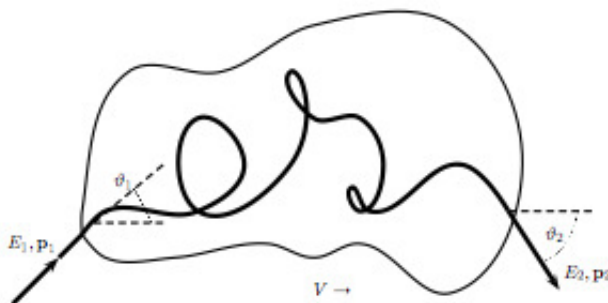


Figure A.2. Elastic Scattering in a Magnetic Cloud. (Kachelrieß 2008)

If we approximate all scatterings due to the magnetic field to be perfectly elastic,  $E'_1 = E'_2$ , where  $E_2$  is the energy of the particle after an encounter with the cloud. After an encounter with the cloud, transforming this energy to the laboratory frame:

$$E_2 = \gamma E'_2 (1 + \beta \cos \theta'_2) \quad (\text{A.2})$$

We can then express the relative energy gain:

$$\begin{aligned}\xi &= \frac{E_2 - E_1}{E_1} = \frac{E_2}{E_1} - 1 = \gamma^2(1 + \beta \cos \theta'_2)(1 - \beta \cos \theta_1) - 1 \\ &= \frac{1 - \beta \cos \theta_1 + \beta \cos \theta'_2 - \beta^2 \cos \theta_1 \cos \theta'_2}{1 - \beta^2} - 1\end{aligned}\quad (\text{A.3})$$

Since the particle will scatter many times off of these magnetic irregularities, its direction on exiting the cloud is randomized. The collision rate between the particle and the cloud is proportional to their relative velocity,  $v - V \cos \theta_1$ . For highly relativistic particles,  $v \rightarrow c$ , and the relative velocity is proportional to,  $c - V \cos \theta$ , or dividing this expression by  $c$ ,  $1 - \beta \cos \theta_1$ .

The collision rate (per solid angle) can be written:

$$\frac{dn}{d\Omega_1} \propto 1 - \beta \cos \theta_1 \quad (\text{A.4})$$

To obtain  $\langle \cos \theta_1 \rangle$ , we find the average value of  $\cos \theta$  over all solid angles:

$$\langle \cos \theta_1 \rangle = \int \cos \theta_1 \frac{dn}{d\Omega_1} / \int \frac{dn}{d\Omega_1} d\Omega_1 \quad (\text{A.5})$$

Using the expression for  $\frac{dn}{d\Omega_1}$  in equation A.4 :

$$\langle \cos \theta_1 \rangle = -\frac{\beta}{3} \quad (\text{A.6})$$

Since the encounter with the cloud will produce random final directions for the particle (see Figure A.2):

$$\langle \cos \theta_2 \rangle = 0 \quad (\text{A.7})$$

Plugging these values into equation A.3, the relative energy gain is given by:

$$\langle \xi \rangle = \frac{E_2 - E_1}{E_1} = \frac{1 + \beta^2/3}{1 - \beta^2} - 1 \approx \frac{4}{3}\beta^2 \quad (\text{A.8})$$

The energy gained by the particle is of second order of  $V/c$  (*second order Fermi acceleration*), where  $V$  is the velocity of the cloud. While the concepts originally

presented by Fermi were instrumental in understanding cosmic ray acceleration, there are a number of problems with second order Fermi acceleration, including the fact that the process is fairly inefficient (since  $V \ll c$ ). A more efficient process, *First order Fermi acceleration*, was proposed independently by a number of researchers in the late 1970's (Axford, Leer, and Skadron 1977, Krymsky 1977, Bell 1978, Blandford & Ostriker 1978; see Longair 2011, Section 17), and has dominated astrophysical thinking since.

First order Fermi acceleration models the acceleration of particles in the presence of strong shocks. These models describe a discontinuity propagating through a diffuse medium, similar to the shock waves that propagate through the interstellar medium (ISM), for example, ahead of the supersonic shells of supernova remnants. In this scenario, a flux of high energy particles is assumed to be present on both sides of the shock front since high energy particles propagate close to the speed of light, much faster than the shock. Because of scattering by streaming instabilities and turbulent motions, the velocity distribution on either side of the shock is isotropic in the reference frame of the moving fluid (see Bell 1978). Figure A.3 shows the dynamics of high energy particles in the vicinity of a strong shock that is propagating at a supersonic velocity,  $U$ , through stationary interstellar gas with pressure;  $p_1$ , temperature,  $T_1$ ; and density,  $\rho_1$  (a). Behind the shock, these values are  $p_2$ ,  $T_2$ , and  $\rho_2$  and are related by the Rankine-Hugoniot jump conditions. The flow of gas in the vicinity of the shock front (b) in the reference frame in which the shock is standing still. (c) in the reference frame in which the upstream gas is stationary and the velocity distribution of the high energy particles is isotropic. (d) in the reference frame in which the downstream gas is stationary and the distribution of the high energy particles is isotropic.

Mass and momentum are conserved when matter passes through the shock.

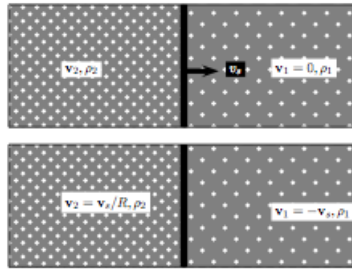


Figure A.3. Dynamics of a Strong Shock. (Longair 2011)

Beginning with the ideal fluid equations for conservation of mass and momentum:<sup>4</sup>

$$\partial_t \rho + \nabla \cdot (\rho v) = 0 \quad (\text{A.9a})$$

$$\rho \frac{dv}{dt} = \rho \frac{\partial v}{\partial t} + \rho v \cdot \nabla v = F - \nabla P \quad (\text{A.9b})$$

where  $\rho$  is the mass density of the fluid,  $v$  is the flow velocity vector,  $F$  is some external force, and  $\nabla P$  is the pressure gradient.

For a one-dimensional, steady strong shock in its rest frame ( $\frac{\partial}{\partial t} = 0$ ), assuming that magnetic and gravitational fields can be neglected. Equations A.9a and A.9b become:

$$\frac{d}{dx}(\rho v) = 0 \quad (\text{A.10})$$

$$\frac{d}{dx}(P + \rho v^2) = 0 \quad (\text{A.11})$$

Accounting for the change in kinetic, internal, and potential energy with time, and also an energy flux through the boundary of the volume in question, conservation of energy can be expressed:

$$\frac{\partial}{\partial t} \left( \frac{\rho v^2}{2} + \rho U + \rho \Phi \right) + \nabla \cdot \left[ \rho v \left( \frac{v^2}{2} + U + \frac{P}{\rho} + \Phi \right) \right] = 0 \quad (\text{A.12})$$

---

<sup>4</sup>The first equation is the *continuity equation*, and requires that for steady state processes, the mass leaving the system equals the mass entering the system. The second equation, the *Euler equation*, expresses the change in velocity (for a fixed coordinate), while accounting for external forces and changes in the pressure gradient.

where  $U$  is the internal energy of the system and  $\Phi$  is the gravitational potential. For a one-dimensional ( $\frac{\partial}{\partial y} = \frac{\partial}{\partial z} = 0$ ) steady state ( $\frac{\partial}{\partial t} = 0$ ) flow, again neglecting the gravitational field, equation A.12 becomes:

$$\frac{d}{dx} \left( \frac{\rho v^2}{2} + (U + P)v \right) = 0 \quad (\text{A.13})$$

For a discontinuity at the shock, we integrate equations A.10, A.11, and A.13 over the discontinuity, we obtain the ‘‘Rankine-Hugoniot’’ jump conditions for a plane-parallel shock:

$$\rho_1 v_1 = \rho_2 v_2 \quad (\text{A.14a})$$

$$P_1 + \rho_1 v_1^2 = P_2 + \rho_2 v_2^2 \quad (\text{A.14b})$$

$$\frac{\rho_1 v_1^2}{2} + \frac{\gamma}{\gamma + 1} P_1 v_1 = \frac{\rho_2 v_2^2}{2} + \frac{\gamma}{\gamma + 1} P_2 v_2 \quad (\text{A.14c})$$

where  $\gamma$  is the ratio of specific heats:  $\gamma = \frac{C_P}{C_V}$ .

Inserting  $\rho_2 = (v_1/v_2)\rho_1$  into equation A.14b, we get:

$$P_2 = P_1 + \rho_1 v_1 (v_1 - v_2) \quad (\text{A.15})$$

We can then eliminate  $\rho_2$  and  $P_2$  from equation A.14c:

$$\frac{\gamma + 1}{\gamma - 1} v_2^2 + \frac{2\gamma}{\gamma - 1} \left( \frac{P_1 + \rho_1 v_1^2}{\rho_1 v_1} \right) v_2 + v_1^2 \frac{2\gamma}{\gamma - 1} \frac{P_1}{\rho_1} = 0 \quad (\text{A.16})$$

Rewriting the speed of sound,  $c_1$ :  $c_1 = \sqrt{\frac{\gamma P_1}{\rho_1}}$ , and replacing  $P_1$  with  $c_1^2$ , and divide through by  $v_1^2$ . Equation A.16 can now be written as a quadratic in terms of  $x = \frac{v_1}{v_2}$ :

$$\frac{\gamma + 1}{\gamma - 1} x^2 + \frac{2\gamma}{\gamma - 1} \left( \frac{c_1^2}{v_1^2} + \gamma \right) x + \left( 1 + \frac{2}{\gamma + 1} \frac{c_1^2}{v_1^2} \right) = 0 \quad (\text{A.17})$$

If we consider only fast flows across strong shocks, the velocity of the gas is much greater than that of the shock ( $v_1 \gg c_1$ ). The *Mach number*,  $M \equiv v_1/c_1$ , is large, and we can neglect the  $1/M^2$  terms and find the solutions to equation A.17:

$$x = 1 \quad (\text{A.18a})$$

$$x = \frac{\gamma - 1}{\gamma + 1} \equiv R \quad (\text{A.18b})$$

where  $R$  is the *compression ratio*. The first solution is trivial since it corresponds to  $v_1 = v_2$ . For a monoatomic ideal gas  $\gamma = 5/3$ , and the second solution corresponds to a scenario in which,  $R = 4$ , or  $v_2 = v_1/4$  and  $\rho_2 = 4\rho_1$ . One of the key features is that for a strong shock, the ratio of upstream and downstream velocities is related by a factor of four.

Similar to the calculation performed for second order Fermi acceleration, for shock acceleration, the collision rate of a particle with the shock is proportional to their relative velocities:

$$\frac{dn}{d\Omega_1} \propto v_2 - V_s \cos \theta_1 = v_s \left( \frac{1}{R} - \cos \theta_1 \right) \propto 4 - \cos \theta_1 \quad (\text{A.19})$$

Where  $v_s$  is the velocity of the shock and  $v_2$  is the particle's velocity and  $R$  is the ratio in equation A.18b.

Again using equation A.3 to calculate the relative energy gain:

$$\langle \cos \theta_1 \rangle = \int \cos \theta_1 (4 - \cos \theta_1) d\Omega_1 / \int (4 - \cos \theta_1) d\Omega_1 = -\frac{2}{3} \quad (\text{A.20})$$

On the other side of the shock:

$$\langle \cos \theta_2 \rangle = -\langle \cos \theta_1 \rangle = \frac{2}{3} \quad (\text{A.21})$$

The average energy gain expressed in equation A.3 becomes:

$$\xi = \frac{E_2 - E_1}{E_1} = \frac{1 + \frac{4}{3}\beta + \frac{4}{9}\beta^2}{1 - \beta^2} - 1 \approx \frac{4}{3}\beta \quad (\text{A.22})$$

The gain is now linear with respect to  $\beta$ , making the case for *first order Fermi acceleration*.

The above first order Fermi acceleration process produces a power law spectrum  $\sim 2$  (see: Longair 2011, Section 17). However, for cosmic rays and non-thermal spectra:  $dN(E) \propto E^{-x}dE$ , where the exponent,  $x$ , is typically measured to be between 2-3. These conditions can be met if first order Fermi acceleration models are modified to include more details surrounding a range of shock conditions, such as scenarios in which the specific heats of the upstream and downstream velocities are different (Bell 1978). With more a detailed treatment of a wide range of shock conditions, the spectrum that results from first order Fermi acceleration has an index:  $x \sim 2.5$ , consistent with the galactic CR spectrum. Figure A.4 shows An *oblique* shock in which propagation is neither parallel nor perpendicular. Bell generalized shock acceleration to any shock orientation.  $B$  shows the direction of the magnetic field, while  $W_1$  and  $W_2$  represent the wave velocity on the respective sides of the front. Bell modeled multiple crossings of charges particles confined to a region around the shock by the Alfvén waves that they generate.

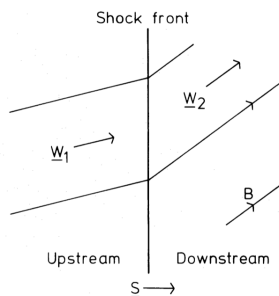


Figure A.4. Oblique Shock. (Bell 1978)

Detailed simulations suggest that shock fronts expanding into uniform circumstellar material, as in supernova remnants (SNR), can accelerate particles to very high energies ( $\sim 10^{17}$  eV; Bell & Lucek 2001). These simulations are supported by strong



observational evidence from the detection of a number of young SNR. In particular, the TeV  $\gamma$ -ray detection suggests efficient acceleration, providing proof that particles  $\sim 100$  TeV are accelerated at the shock (Aharonian et al. 2007). Figure A.5 shows the TeV  $\gamma$ -ray image of SNR RX J0852.0-4622, one of the first shell-type SNR to be detected at TeV energies (Aharonian et al. 2007). The  $\gamma$ -ray image shows excess counts and resembles that of a homogeneously emitting shell. To date, TeV  $\gamma$ -rays from approximately 13 shell-type SNR have been detected (Wakely & Horan 2015).

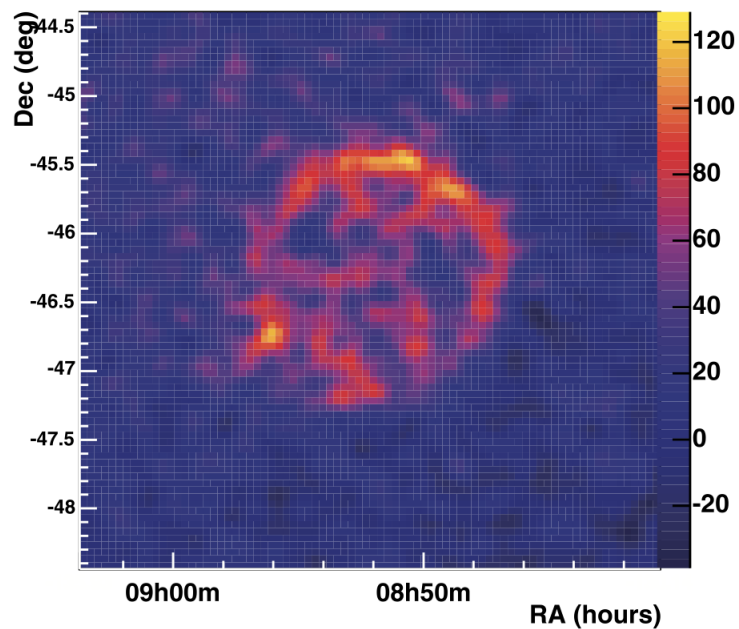


Figure A.5. SNR RX J0852.0-4622. (Aharonian et al. 2007)

## APPENDIX B

VHE  $\gamma$ -RAY EMISSION DUE TO NEUTRAL PION DECAY

Particles that have undergone acceleration processes in extreme astrophysical environments produce high energy radiation by reacting with ambient matter and fields. When relativistic protons and nuclei (cosmic rays, CRs) collide inelastically with ambient gas in the interstellar medium (ISM) they produce TeV  $\gamma$ -rays via the production and decay of secondary pions, kaons, and hyperons. The neutral pion provides the main channel for the creation of high energy  $\gamma$ -rays, and this channel is thought to provide the principal source of diffuse galactic emission above 200 MeV (see Mori 1997, Dermer 1986).

Pion decay has been studied by a number of authors (Stecker 1971, Dermer 1986, Mori 1997), and a precise solution requires integration over cross-sections obtained experimentally by particle detectors (see Mori 1997). However, simple formalisms can explain some of the most important features of the observed  $\gamma$ -ray spectrum. This section follows the work of Stecker (1971) and describes the notable features of diffuse  $\gamma$ -ray emission due to neutral pion decay.

## B.1 Pion Production Kinematics

Astrophysical proton-proton reactions involve energies much larger than the rest masses of the particles involved, therefore relativistic kinematics are used to describe the reactions between particles. Following Stecker, four-vectors are used to describe the momentum and velocity of the particles:

$$\begin{aligned} p^{(4)} &= (p, iE) \\ \beta^{(4)} &= (\beta, i) \end{aligned} \tag{B.1}$$

where  $\beta = v/c$  and  $c$ , the speed of light is taken as unity.

Introducing the *rapidity*,  $\phi$ , Stecker described Lorentz transformations as hyperbolic rotations in the complex four vector space. Using four-vectors, Lorentz transformations are simply hyperbolic rotations in the complex four-vector space.

The *rapidity*,  $\phi$ , is given by:

$$\tanh(\phi) = \beta = \frac{v}{c} \quad (\text{B.2})$$

The Lorentz factor,  $\gamma$  can be written in terms of the rapidity:

$$\gamma = \frac{1}{\sqrt{1 - \beta^2}} = \frac{1}{\sqrt{1 - \tanh^2(\phi)}} = \frac{\cosh^2(\phi)}{\sqrt{\cosh^2(\phi) - \sinh^2(\phi)}} = \cosh(\phi) \quad (\text{B.3})$$

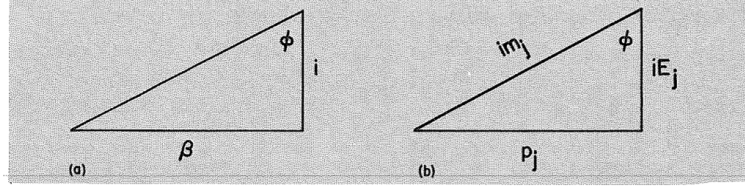


Figure B.1. Energy Momentum and Velocity Triangles. (Stecker 1971)

From Figure B.1, we can derive the following geometric relationships to describe relativistic kinematics:

$$\begin{aligned} E &= m \cosh(\phi) = \frac{m}{\sqrt{1 - \beta^2}} = m\gamma \\ p &= m \sinh(\phi) = \frac{m\beta}{\sqrt{1 - \beta^2}} = m\beta\gamma \\ E &= m \cosh(\phi) = \frac{m}{(1 - \beta^2)^{1/2}} \end{aligned} \quad (\text{B.4})$$

For the case of a two-body collision in which a particle  $a$  collides with particle  $b$  initially at rest in the lab system, Stecker derived an expression for the cms energies of the particles after the collision. The length of the four-vector momentum is invariant, so we describe a transformation between the laboratory system (ls) and the center-of-momentum system (cms) by equating the lengths of the momentum vectors:

$$[\sum p_{ls}^{(4)}]^2 = [\sum p_{cms}^{(4)}]^2 \quad (\text{B.5})$$

Noting that and  $p'_a = -p'_b$  in the cms. Equation B.5 simplifies to:

$$p_a^2 - (E_a + m_b)^2 = -(E'_a + E'_b)^2 \quad (\text{B.6})$$

where quantities in the cms are denoted in primes.

From Equation B.6, the total energy in the cms frame can be written:

$$\begin{aligned} E' = E'_a + E'_b &= [(E_a + m_b)^2 - p_a^2]^{1/2} = [E_a^2 - p_a^2 + m_b^2 + 2m_b E_a]^{1/2} \\ &= [m_a^2 + m_b^2 + 2m_b E_a]^{1/2} \end{aligned} \quad (\text{B.7})$$

Taking another invariant inner product of the momentum four-vector:

$$\begin{aligned} [p_a^{(4)} \cdot (p_a^{(4)} + p_b^{(4)})]_{ls} &= [p_a^{(4)} \cdot (p_a^{(4)} + p_b^{(4)})]_{cms} \\ (p_a, E_a) \cdot [(p_a + p_b), (E_a + E_b)] &= (p'_a, E'_a) \cdot [(p'_a + p'_b), (E'_a + E'_b)] \end{aligned} \quad (\text{B.8})$$

If we consider a system in which the target particle, b, is at rest in the ls,  $p_b = 0$ , and in the cms frame,  $p'_a = -p'_b$ . The above simplifies to:

$$(p_a, E_a) \cdot [p_a, (E_a + E_b)] = (p'_a, E'_a) \cdot [0, (E'_a + E'_b)] \quad (\text{B.9})$$

Solving Equation B.9, first for  $E'_a$ , and then for  $E'_b$ , and using the substitution for  $E'$  found in Equation B.7, we obtain expressions for the individual cms energies of particles  $a$  and  $b$ :

$$\begin{aligned} E'_a &= \frac{E'^2 + m_a^2 - m_b^2}{2E'} \\ E'_b &= \frac{E'^2 + m_b^2 - m_a^2}{2E'} \end{aligned} \quad (\text{B.10})$$

Lorentz transformations can be expressed as “rotations” through an imaginary angle  $\phi$  in the complex four-vector space. If we denote the original system with subscript 1, the transformation quantity with a subscript 2, and the final transformed quantity with a subscript, 3:

$$\phi_3 = \phi_2 + \phi_2 \quad (\text{B.11})$$

We can transform our kinetic equations from one system to another by performing a Lorentz transformation specified by some velocity  $\beta_2$ . The Lorentz transformation in the new system can be written:

$$\begin{aligned}
 \gamma_3 &= \cosh \phi_3 = \cosh(\phi_1 + \phi_2) \\
 &= \cosh \theta_1 \cosh \theta_2 + \sinh \theta_1 \sinh \theta_2 \\
 &= \gamma_1 \gamma_2 + \gamma_1 \beta_1 + \gamma_2 \beta_2 \\
 &= \gamma_2 [\gamma_1 + \beta_2 (\gamma_1 \beta_1)]
 \end{aligned} \tag{B.12}$$

Using the relations in Equation B.4, the above equation becomes the energy transformation relation:

$$E_3 = \gamma_2 [E_1 + \beta_2 p_1] \tag{B.13}$$

However, by analogy of the Lorentz contraction formulas:  $x_3 = \gamma_2(x_1 + \beta_2 t_1)$ , we must generalize our transformations to reactions in a 2-dimensional x-y plane:  $x \rightarrow x \cos \theta$  and  $p \rightarrow p \cos \theta$ . Generalizing the energy transformation equation by looking at reactions in a 2-dimensional x-y plane (with x at an angle  $\theta$  with the axis of the Lorentz transform,  $x \rightarrow x \cos \theta$  and  $p \rightarrow p \cos \theta$ ). More generally, the energy transformation equation can be written:

$$E_3 = \gamma_2 [E_1 + \beta_2 p_1 \cos \theta] \tag{B.14}$$

To describe pion decay, Stecker modeled a scenario in which a particle of mass,  $M$ , decays into two particles of mass,  $m_a$  and  $m_b$ , in the rest frame of mass,  $M$ .

The cms energy of the two particles is given by equations B.10 which becomes:

$$\begin{aligned}
 E'_a &= \frac{M^2 + m_a^2 - m_b^2}{2M} \\
 E'_b &= \frac{M^2 + m_b^2 - m_a^2}{2M}
 \end{aligned} \tag{B.15}$$

since mass,  $M$ , is initially at rest in the cms.

To obtain the Lorentz transformation into an ls where the original mass  $M$  has energy  $E_M = \gamma M$ , we use equation the energy transformation relations given in

equation B.14:

$$E_{a,b} = \gamma(E'_{a,b} + \beta p' \cos \theta') \quad (\text{B.16})$$

The rest system of mass,  $M$  must be the cms for the two decays particles, as they must have equal and opposite momentum,  $p'$ . Combining Equations B.10 & B.16: Equations B.15 now becomes:

$$E_{a,b} = \frac{E_M}{M} \left[ \left( \frac{M^2 + m_{a,b}^2 - m_{b,a}^2}{2M} \right) + \left( 1 - \frac{M^2}{E_M^2} \right)^{1/2} p' (M, m_a, m_b) \cos \theta' \right] \quad (\text{B.17})$$

$$E_{a,b} = \frac{E_M}{M} \left[ \left( \frac{M^2 + m_{a,b}^2 - m_{b,a}^2}{2M} \right) + \left( 1 - \frac{M^2}{E_M^2} \right)^{1/2} \times p' (M, m_a, m_b) \cos \theta' \right] \quad (\text{B.18})$$

where  $p'$  is given by conservation of energy:  $(p'^2 + m_a^2)^{1/2} + (p'^2 + m_b^2)^{1/2} = M$ .

If both decay particles have mass zero (as in the case of  $\gamma$ -ray production), the above equation reduces to:

$$E_{a,b} = \frac{1}{2} E_M \left[ 1 + \left( 1 - \frac{M^2}{E_M^2} \right)^{1/2} \cos \theta' \right] = \frac{1}{2} M (1 + \beta_M \cos \theta') \quad (\text{B.19})$$

This provides the energy of the pion decay products in the ls.

Stecker defined the energy distribution function as the the probability that a  $\gamma$ -ray of energy,  $E_\gamma$  will result from the decay of a particle of type s:

$$f_s(E_\gamma | E_s) \quad (\text{B.20})$$

Assuming the particle  $M$  decays isotropically, there is equal probability of emission in all directions in the cms, and we can rewrite the energy distribution based on the angular distribution of the emitted particles. The normalized angular distribution function is given by:

$$f(\theta') d\theta' = \frac{d\Omega(\theta')}{4\pi} = \frac{1}{2} \sin \theta' d\theta' \quad (\text{B.21})$$

If we define:

$$\eta = \mu/M \tag{B.22}$$

$$\kappa = p'/M$$

and

$$\kappa = p'/M \tag{B.23}$$

where  $\mu$  is the cms energy of the decay particle (see equation B.15). Equation B.18 becomes:

$$E(\theta') = E_M(\eta + \beta\kappa \cos \theta') \tag{B.24}$$

and

$$dE(\theta') = \beta E_M \kappa \sin(\theta') d\theta' \tag{B.25}$$

We can now rewrite the energy distribution function:

$$f(E)dE = \frac{f(\theta')}{dE/d\theta'} dE = \frac{1}{2\beta E_M} dE \tag{B.26}$$

If the decay products have zero mass,  $p' = M/2$  from the energy conservation equations. Equation B.26 simplifies to:

$$f(E)dE = (E_\pi^2 - m_\pi^2)^{-1/2} dE \tag{B.27}$$

Figure B.2 shows the form of the energy distribution function for a particle formed isotropically from two-body decay (Stecker 1971).

**B.2 Gamma-ray Spectrum due to Neutral Pion Decay** Adopting the framework of Stecker, we can define a source function  $q(E)$ , where  $q(E)dE$  is the number of particles with energy in the range between  $E$  and  $E + dE$  produced *per unit volume per unit time*. This source function for pion production can be written:

$$q_\pi(E_\pi) = n\nu_c \langle \zeta \rangle \tag{B.28}$$



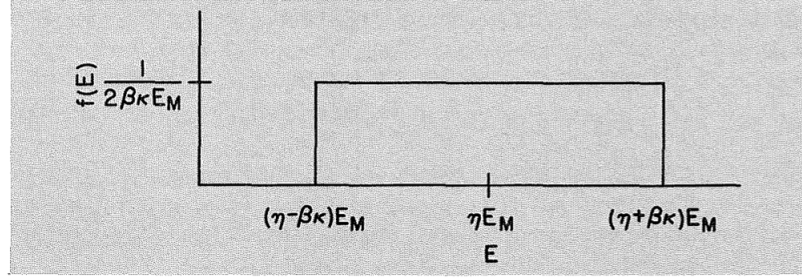


Figure B.2. Energy Distribution of Two-body Decay. (Stecker 1971).

where  $n$  is the density of the target nuclei in the medium being considered,  $\nu_c$  is the collision frequency per target nucleus and  $\langle \zeta \rangle$  is the average multiplicity of particles produced per collision.  $\nu_c$  is related to the average collisional cross-section,  $\langle \sigma \rangle$ :

$$\nu_c = \langle \sigma \rangle 4\pi I_{cr} \quad (\text{B.29})$$

where  $I_{cr}$  is the average directional intensity of cosmic rays (in units of  $m^{-2}s^{-1}sr^{-1}$ ). (The  $4\pi$  comes from the integration over the solid angle.)

The CR “beam” intensity varies with energy, and the CR energy ( $E_{cr}$ ) also determines the cross-section value. Combining (B.28) and (B.29), and explicitly expressing the dependence of the primary CR energy:

$$q_\pi(E_\pi) = 4\pi n \int \sigma(E_{cr}) I(E_{cr}) dE_{cr} \quad (\text{B.30})$$

The concentration of CR particles,  $N$ , is related to the CR intensity:

$$N(E_{cr}) = \frac{1}{v} \int I(E_{cr}) d\Omega = \frac{4\pi \bar{I}(E_{cr})}{v} \quad (\text{B.31})$$

where  $v$  is the velocity of the CR particle.

Using this relationship, Equation (B.30) becomes:

$$q_\pi(E_\pi) = N(E_{cr}) v \int \sigma(E_{cr}) dE_{cr} \quad (\text{B.32})$$

In the case of a *catastrophic collision* of two protons that leads to pion production, the cross section should be represented by  $\sigma(E', E)$  which is the probability per unit time and per unit energy of the appearance of a neutral pion with an energy  $E$ , that results from the collision of a CR proton, of energy  $E'$ . Following Gaisser (1990), we rewrite the cross section using the delta function approximation:

$$\sigma_i^k(E', E) = \sigma_i^k E_p \delta(E, E') \quad (\text{B.33})$$

If  $k_\pi$  is that fraction of the kinetic energy of the proton ( $E_{\text{kin}} = E_p - m_p c^2$ ) transferred to the neutral pion ( $k_\pi \sim 0.17$ ; Gaisser 1990):

$$E_\pi = k_\pi E_{\text{kin}} = k_\pi (E_p - m_p c^2) \quad (\text{B.34})$$

Rearranging Equation B.34, to express the proton energy in terms of the energy of the pion:

$$E_p = \frac{E_\pi}{k_\pi} + m_p c^2 \quad (\text{B.35})$$

The cross-section becomes:

$$\sigma(E', E) = \sigma E_p \delta(E_\pi, k_\pi E_{\text{kin}}) \quad (\text{B.36})$$

Using this expression for the cross-section, the pion emissivity becomes:

$$\begin{aligned} q_\pi(E_\pi) &= nv \int \sigma_i^k E_p \delta(E_\pi - k_\pi E_{\text{kin}}) N(E_{\text{cr}}) \frac{1}{k_\pi} dE_\pi \\ &= \frac{nv}{k_\pi} \sigma (E_\pi k_\pi + m_p c^2) N(E_\pi k_\pi + m_p c^2) \end{aligned} \quad (\text{B.37})$$

The  $\gamma$ -ray emissivity can be expressed, using the energy distribution function (Equation B.27; see Ahanonian 2004, Section 3.1). The  $\gamma$ -ray emissivity is given by:

$$q_\gamma = 2 \int_{E_{\text{min}}}^{\infty} \frac{q_\pi(E_\pi)}{\sqrt{E_\pi^2 - m_\pi^2 c^4}} dE_\pi \quad (\text{B.38})$$

$E_{\text{min}}$  is obtained from equation B.19, noting that in the extreme cases,  $\gamma$ -rays are emitted such that,  $\cos\theta' = 1, -1$ , providing the maximum and minimum energies

of the particles in the ls:

$$\begin{aligned} E_{\gamma,\min} &= \frac{1}{2}E_{\pi}(1 - \beta_{\pi}) \\ E_{\gamma,\max} &= \frac{1}{2}E_{\pi}(1 + \beta_{\pi}) \end{aligned} \quad (\text{B.39})$$

For a photon emitted with energy,  $E_{\gamma,\max}$ , there must be a corresponding photon emitted of energy,  $E_{\gamma,\min}$ :

$$E_{\gamma,\max} + E_{\gamma,\min} = \frac{1}{2}E_{\pi}(1 + \beta_{\pi}) + \frac{1}{2}E_{\pi}(1 - \beta_{\pi}) = E_{\pi} \quad (\text{B.40})$$

Noting that:

$$(E_{\gamma,\min})(E_{\gamma,\max}) = \frac{1}{4}E_{\pi}^2(1 - \beta_{\pi}^2) = \frac{1}{4}m_{\pi}^2 \quad (\text{B.41})$$

We can write the energy of the pion as:

$$E_{\pi} = E_{\gamma,\max} + \frac{m_{\pi}^2}{4E_{\gamma,\max}} \quad (\text{B.42})$$

This criteria becomes the lower limit for pion creation, corresponding to the minimum energy needed to produce the emission of two  $\gamma$ -rays (at various energies and angles  $\theta$ , see: Equation B.19). The lower limit on the pion energy integration becomes:

$$E_{\pi,\min} = E_{\gamma} + \frac{m_{\pi}^2}{4E_{\gamma}} \quad (\text{B.43})$$

Using these results we can model the spectrum that results from neutral pion decay in various astrophysical settings. Approximating cross-section values from accelerator experiments (for example, Kamae et al. 2006), we can compute the  $\gamma$ -ray emissivity per hydrogen atom expected for a given CR flux (for example, see Aharonian 2004, Figure 3.3). Figure B.3 shows the predicted  $\gamma$ -ray spectrum due to pion decay in the core of starburst galaxy M82 using Equation B.38. High CR and gas densities make the galaxy an excellent candidate for  $\gamma$ -ray production due to neutral pion decay.

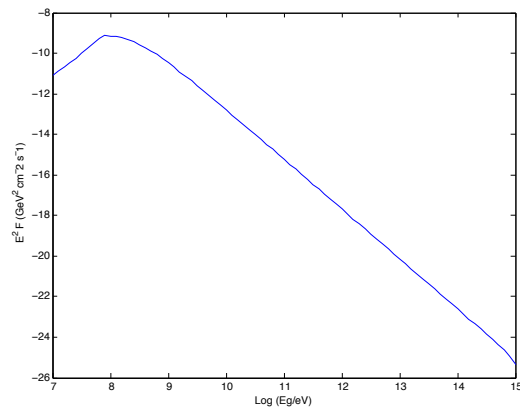


Figure B.3. Predicted  $\gamma$ -ray Spectrum due to Pion Decay.

APPENDIX C  
CRAB SENSITIVITY STUDIES SUPPLEMENTARY TABLES

The Crab Nebula is one of the strongest, most steady sources of VHE  $\gamma$ -rays. It is commonly used to monitor the performance of the VERITAS instrument and the various analysis packages used by the collaboration. Within the collaboration, Crab studies have been to understand and optimize a broad range of VERITAS analyses. This section provides the runlists and full results of studies used to understand the sensitivity of the standard analysis package and to optimize the quality and gamma/hadron cuts used for the final analysis of M82.

### C.1 Eventdisplay v470 Sensitivity Study

The first sensitivity study was performed to test the performance of the Eventdisplay analysis package. The study was done using standard *hard cuts* for Eventdisplay v470 (see Table 6.2). The study examined both low and high elevation data across all 3 observing epochs. Tables C.1 and C.2 show the V4 runlists. Tables C.4 and C.5 show the V5 runlists. Tables C.7 and C.8 show the V6 runlists. Data was processed using the standard Eventdisplay procedure with the  $\gamma$ -ray signal scaled down to estimate the results for weaker sources. The results of the analysis are then used to estimate the time required for a 5 sigma detection. The results of the Eventdisplay analysis are shown in Tables C.3, C.6, and C.9.

### C.2 M82 Cut Optimization

A second sensitivity study was performed to determine the appropriate cuts to use for the final M82 analysis. The V4 data was processed using the same cuts as those used for the original VERITAS detection (Acciari et al. 2009); however, the analysis had never been optimized for the V5 and V6 data. The cut optimization process is described in Section 6.2. Tables 6.4 and 6.5 show the results of the size and  $\theta^2$  optimization respectively. Tables C.10 and C.11 show the runlists used for these analyses.

Table C.1. V4 Low Elevation Crab Runlist

Date	Run	Elevation (°)	Date	Run	Elevation (°)
20080112	38753	58	20090128	44237	42
20080311	39833	66	20090131	44330	56
20080328	40036	40	20090131	44339	44
20081027	42510	68	20090201	44370	54
20081222	43681	48	20090220	44609	52
20081222	43682	52	20090222	44660	49
20081229	43748	47	20090226	44694	46
20081229	43749	52	20090301	44780	51
20081229	43750	57	20090314	44863	63
20081229	43754	62	20090314	44864	59
20081229	43766	64	20090314	44865	54
20090118	44053	63	20090318	44926	52
20090118	44054	58	20090319	44953	51
20090118	44055	54	20090324	45082	52
20090120	44098	64	20090326	45141	50
20090128	44236	46			

Table C.2. V4 High Elevation Crab Runlist

Date	Run	Elevation (°)	Date	Run	Elevation (°)
20080928	41727	74	20081106	42895	69
20080929	41793	72	20081107	42928	80
20080929	41794	76	20081108	42948	79
20080930	41851	79	20081108	42949	76
20081001	41876	71	20081201	43366	80
20081001	41877	75	20081201	43367	79
20081001	41879	78	20081204	43464	80
20081002	41925	76	20081204	43465	80
20081002	41926	79	20081229	43757	73
20081004	41988	81	20081229	43758	76
20081006	42032	80	20081229	43760	80
20081025	42439	79	20081229	43763	77
20081025	42440	80	20081229	43764	73
20081028	42553	79	20081229	43765	70
20081105	42854	78	20090116	44015	78
20081106	42894	74			



Table C.3. V4 Sensitivity Results

Low Elevation		High Elevation	
Flux (Crab Units)	Time (Hr)	Flux (Crab Units)	Time (Hr)
1.0	0.105	1.0	0.058
0.1	1.56	0.1	0.865
0.03	10.6	0.03	5.76
0.01	74.8	0.01	41.0

Table C.4. V5 Low Elevation Crab Runlist

Date	Run	Elevation (°)	Date	Run	Elevation (°)	Date	Run	Elevation (°)
20091118	48403	65	20110104	54173	48	20120219	60438	61
20091120	48456	42	20110104	54174	52	20120225	60613	65
20091122	48535	40	20110203	54783	63	20120225	60614	61
20091215	48930	63	20110228	55215	66	20120315	61200	43
20110102	54081	44	20110309	55469	65	20120316	61260	53
20110103	54114	41	20111127	58970	64	20120317	61290	50
20110103	54115	47	20111227	59451	65	20120317	61291	44
20110103	54116	51	20120219	60436	65	20120317	61292	41

Table C.5. V5 High Elevation Crab Runlist

Date	Run	Elevation (°)	Date	Run	Elevation (°)	Date	Run	Elevation (°)
20091118	48394	68	20091215	48924	80	20110123	54501	71
20091118	48395	73	20091215	48925	81	20110123	54502	76
20091118	48396	76	20091215	48926	78	20110123	54503	78
20091118	48397	78	20091215	48927	76	20110124	54520	74
20091118	48398	80	20091215	48928	71	20110124	54521	78
20091118	48399	79	20091215	48929	68	20110124	54522	80
20091118	48400	77	20101208	53703	78	20110127	54586	79
20091118	48401	73	20101208	53704	80	20110127	54587	77
20091118	48402	70	20101208	53705	80	20110128	54612	73
20091123	48587	67	20101209	53734	77	20110128	54613	76
20091211	48854	80	20101209	53735	80	20110128	54614	79
20091215	48921	69	20101209	53736	80	20110204	54806	74
20091215	48922	73	20101210	53772	78	20110204	54807	77
20091215	48923	76	20101211	53811	78			

Table C.6. V5 Sensitivity Results

Low Elevation		High Elevation	
Flux (Crab Units)	Time (Hr)	Flux (Crab Units)	Time (Hr)
1.0	0.074	1.0	0.044
0.1	1.02	0.1	0.588
0.03	6.66	0.03	3.76
0.01	45.8	0.01	25.9

Table C.7. V6 Low Elevation Crab Runlist

Date	Run	Elevation (°)	Date	Run	Elevation (°)	Date	Run	Elevation (°)
20121212	65456	40	20130307	67140	48	20131030	70351	63
20130105	65776	64	20130307	67141	41	20131031	70373	56
20130206	66582	55	20130308	67231	43	20131102	70458	60
20130213	66735	59	20130311	67253	58	20131104	70482	49
20130216	66867	44	20130311	67254	52	20131106	70527	62
20130216	66868	40	20130312	67272	64	20131106	70530	61
20130302	67071	63	20130313	67293	61	20131109	70604	51
20130302	67072	58	20130315	67374	52	20130311	67251	71
20130302	67074	52	20130331	67602	52	20130311	67252	65
20130302	67075	47	20130331	67603	44	20130312	67271	69
20130303	67092	51	20131007	69976	41	20130314	67332	67
20130303	67093	47	20131007	69977	49			
20130303	67094	42	20131007	69978	55			
20130307	67138	40	20131007	69979	61			
20130307	67139	54	20131028	70314	40			

Table C.8. V6 High Elevation Crab Runlist

Date	Run	Elevation (°)	Date	Run	Elevation (°)
20121013	64080	79	20121210	65370	73
20121013	64081	80	20121210	65371	77
20121013	64082	80	20121211	65404	79
20121013	64083	77	20121211	65474	79
20121020	64257	67	20130105	65777	71
20121020	64259	74	20130105	65778	76
20121022	64325	76	20130105	65779	79
20121022	64326	80	20130113	66002	73
20121024	64378	78	20130116	66112	77
20121024	64379	79	20130116	66113	80
20121024	64380	80	20130201	66534	79
20121026	64444	66	20130205	66556	79
20121113	64759	77	20130205	66557	74
20121113	64760	80	20130208	66625	73
20130307	67137	67	20130208	66626	67
20121208	65311	74	20130301	67044	78
20121208	65312	79	20130307	67135	75

Table C.9. V6 Sensitivity Results

Low Elevation		High Elevation	
Flux (Crab Units)	Time (Hr)	Flux (Crab Units)	Time (Hr)
1.0	0.070	1.0	0.037
0.1	0.95	0.1	0.52
0.03	6.3	0.03	3.38
0.01	42.6	0.01	23.6

Table C.10. V6 Crab Low Elevation Runlist: Size Study

Date	Run	Elevation(°)	Date	Run	Elevation(°)
20130206	66582	55	20131007	69977	49
20130213	66735	59	20131007	69978	55
20130302	67072	58	20131031	70373	56
20130302	67074	52	20131104	70482	49
20130302	67075	47	20131107	70551	51
20130303	67092	51	20131109	70604	51
20130303	67093	47	20141025	74829	57
20130307	67139	54	20141028	74894	59
20130307	67140	48	20141229	75837	47
20130311	67253	58	20141230	75863	47
20130311	67254	52	20150120	76040	47
20130315	67374	52	20150212	76304	57
20130331	67602	52	20150212	76305	52



Table C.11. V5 Crab High Elevation Runlist:  $\theta^2$  Study

Date	Run	Elevation (°)	Date	Run	Elevation (°)
20091027	47833	76	20091123	48581	78
20091027	47834	72	20091123	48582	80
20091027	47835	69	20091123	48583	80
20091029	47866	76	20091123	48584	76
20091029	47867	73	20091123	48585	73
20091118	48395	73	20091123	48587	67
20091118	48396	76	20091211	48854	80
20091118	48397	78	20091215	48921	69
20091118	48398	80	20091215	48922	73
20091118	48399	79	20091215	48923	76
20091118	48400	77	20091215	48924	80
20091118	48401	73	20091215	48925	81
20091118	48402	70	20091215	48926	78
20091118	48403	65	20091215	48927	76
20091123	48578	67	20091215	48928	71
20091123	48579	71	20091215	48929	68
20091123	48580	75	20091215	48930	63

APPENDIX D  
SYSTEMATIC CHECKS

Several tests were performed to ensure that systematic effects did not create a false signal for the final M82 analysis. Figure D.1 shows the cumulative significance and the significance distribution of skymap pixels for the M82 region. The cumulative significance plot shows the signal steadily build. The red curve in the significance distribution plot shows the skymap pixels, including the M82 region. The blue curve excludes an 0.35 degree radius centered on the M82 region. The green line shows the Gaussian fit to the blue curve. The Gaussian fit shows a mean centered at approximately zero. The root mean square (rms) value is close to 1 which is expected for a purely random distribution of background events.

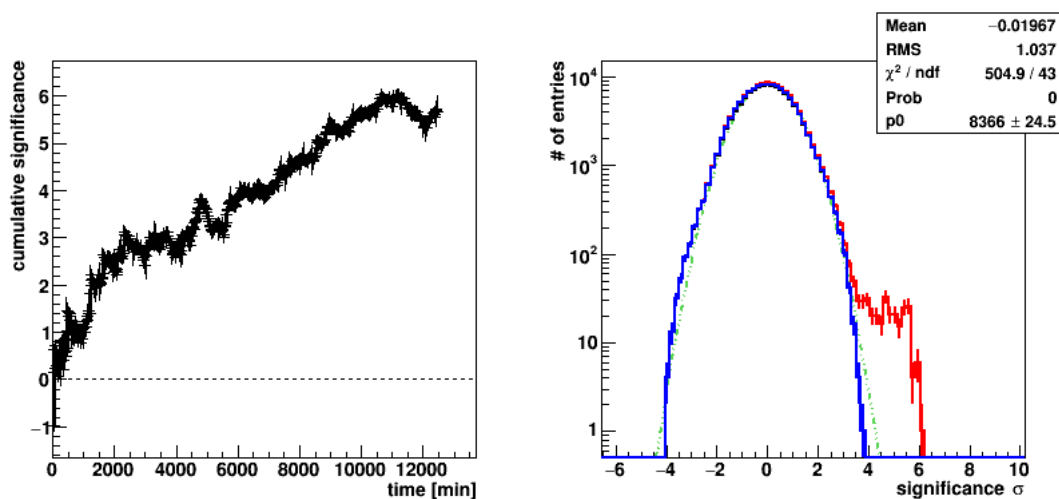


Figure D.1. Significance Metrics.

To test the validity of the flux and spectral calculations, an analysis was run using low elevation Crab data from each epoch. The same cuts and effective areas were used to reconstruct the Crab spectrum. Figure D.2 shows the results compared to other instruments' best-fit spectrum obtained from their Crab Nebula detections. The plots show (clockwise from the top left) our results for the V4, V5, & V6 data. The dark green lines show the Magic log-parabolic fit, the blue lines show the H.E.S.S. power law spectrum with an exponential cut-off, the light green lines show the H.E.S.S. power law spectrum, and red lines show the Whipple power

law spectrum. The Crab spectra constructed from our parameters are in reasonable agreement with these instruments.

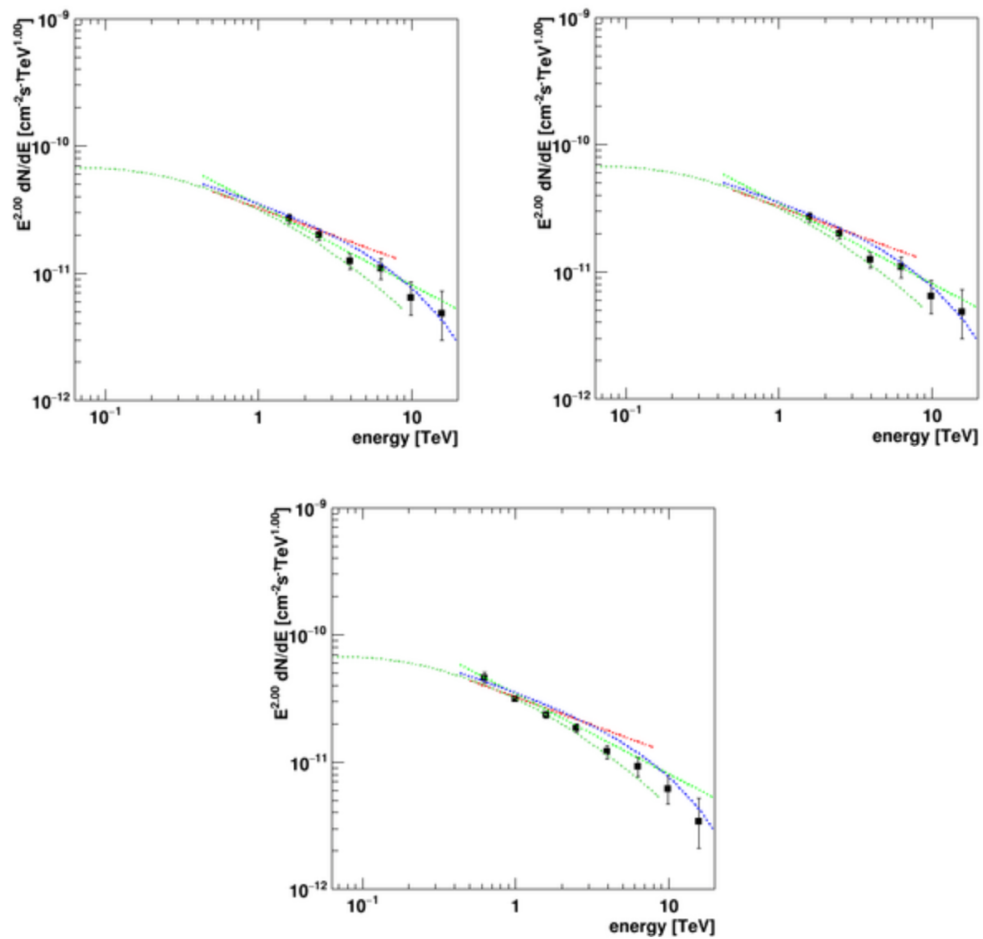


Figure D.2. Reconstructed Crab Spectrum.

## BIBLIOGRAPHY

- [1] Abdo, A.A. et al. [The Fermi LAT Collaboration]. “Detection of Gamma-Ray Emission from the Starburst Galaxies M82 and NGC 253 with the Large Area Telescope on Fermi.” *The Astrophysical Journal Letters* 709 (2010): 152.
- [2] Abramowski, A. et al. [The H.E.S.S. Collaboration]. “Spectral Analysis and Interpretation of the  $\gamma$ -ray Emission from the starburst galaxy NGC 253.” *The Astrophysical Journal* 757.2 (2012).
- [3] Acciari, V.A. et al. [The VERITAS Collaboration]. “A connection between star formation activity and cosmic rays in the starburst galaxy M82.” *Nature* 462 (2009): 770-772.
- [4] Acero, F., A. Bamba, S. Casanova, E. de Cea, E. de Ona Wilhelmi, S. Gabici, Y. Gallant, D. Hadasch, A. Marcowith, G. Pedalletti, O. Reimer, M. Renaud, D.F. Torres, F. Volpe. “Gamma-ray signatures of cosmic ray acceleration, propagation, and confinement in the era of CTA.” *Astroparticle Physics* 43 (2013): 276-286.
- [5] Acharya, B.S. “Ground-based TeV  $\gamma$ -ray Astronomy in India.” *Proceedings of the 29th International Cosmic Ray Conference*, Pune, India, 2005.
- [6] Acharya, B.S. et al. [The CTA Collaboration]. “Introducing the CTA concept.” *Astroparticle Physics* (2013): 3-18.
- [7] Ackermann, M. et al. [The Fermi LAT Collaboration]. “GeV Observations of Star-forming Galaxies with the Fermi Large Area Telescope.” *The Astrophysical Journal* 755.164 (2012).
- [8] Aharonian, F.A. & A.K. Konopelko. “Stereo Imaging of VHE Gamma-Rays.” *Proceedings of Towards a Major Atmospheric Cherenkov Detector-V*, Kruger Park, South Africa, 1997.
- [9] Aharonian, F.A. et al. [The H.E.S.S. Collaboration]. “Evidence for TeV gamma ray emission from Cassiopeia A.” *Astronomy and Astrophysics* 370 (2001): 112.
- [10] Aharonian, F.A. *Very High Energy Cosmic Gamma Radiation: A Crucial Window to the Extreme Universe*. River Edge:World Scientific, 2004.
- [11] Aharonian, F. et al. [The H.E.S.S. Collaboration]. “A new population of very high energy  $\gamma$ -ray sources in the Milky Way.” *Science* 307.5717 (2005): 1938-1942.
- [12] Aharonian, F. et al. [The H.E.S.S. Collaboration]. “Observations of the Crab Nebula with H.E.S.S.” *Astronomy and Astrophysics* 457 (2006): 899-915.
- [13] Aharonian, F.A. et al. [The H.E.S.S. Collaboration]. “H.E.S.S. Observations of the Supernova Remnant RX J0852.0-4622: Shell Type Morphology and spectrum of a widely extended very high energy gamma-ray source.” *The Astrophysical Journal* 661 (2007): 236-249.
- [14] Aharonian, F., Buckley, J., Kifune, T. & Sinnis, G. “High energy astrophysics with ground-based gamma ray detectors.” *Reports on Progress in Physics* 71.09 (2008).

- [15] Antonucci, R.R.J. & Ulvestad, J. S. “A large family of compact radio sources in the starburst nucleus of NGC 253.” *The Astrophysical Journal, Part 2 - Letters* 339 (1988): L97-L100.
- [16] Arbutina, B., Urošević & Vukotić, B. “High supernova rate and enhanced star-formation triggered in M81-M82 encounter.” *Proceedings of the International Astronomical Union Symposium*, 2006.
- [17] Arqueros, F., S. Martinez & M. Rozanska, *Proceedings of the 23rd International Cosmic Ray Conference*, Calgary, Canada, 1993.
- [18] Axford, W.I., Leer, E. & Skadron G. “The acceleration of cosmic rays by shock waves.” *Proceedings of the 15th International Cosmic Ray Conference*, Plovdiv, Bulgaria, 1997.
- [19] Baade, W. & F. Zwicky, “Supernovae and cosmic rays.” *Physical Review* 46 (1934): 76.
- [20] Battistoni, G., S. Muraro, P.R. Sala, F. Cerutti, A. Ferrari, S. Roesler, A. Fasso, J. Ranft, 2007. The FLUKA code: Description and benchmarking, Proceedings of the Hadronic Shower Simulation Workshop Fermilab, IL M. Albrow, R. Raja eds., *AIP Conference Proceedings* 896 (September 2006): 31-49.
- [21] Bell, A. R. “The acceleration of cosmic rays in shock fronts. I” *Monthly Notices of the Royal Astronomical Society* 182 (1978): 147-156.
- [22] Bell, A. R. & Lucek, S. G. “Cosmic ray acceleration to very high energy through the non-linear amplification by cosmic rays of the seed magnetic field.” *Monthly Notices of the Royal Astronomical Society* 321 (2001): 433.
- [23] Berge, D., Funk, S. & Hinton, J. “Background modelling in very-high-energy  $\gamma$ -ray astronomy.” *Astronomy and Astrophysics* 466 (2007): 1219.
- [24] Bernlöhr, K. “Simulations of imaging atmospheric Cherenkov telescopes with CORSIKA and sim\_telarray.” *Astroparticle Physics* 30.149 (2008).
- [25] Blackett, P.M.S., “The Emission Spectra of the Night Sky and Aurorae” *The International Conference* London: The Physical Society (1948): 34
- [26] Blandford, R.D. & J.P. Ostriker. “Particle Acceleration by Astrophysical Shocks.” *The Astrophysical Journal* 221 (1978): L29-L32.
- [27] Blasi P., E. Amato & D. Caprioli. “The maximum momentum of particles accelerated at cosmic ray modified shocks.” *Monthly Notices of the Royal Astronomical Society* 375 (2007): 1471-1478.
- [28] Blom, J.J. Paglione & T., Carramiñana, “Diffuse Gamma-Ray Emission from Starburst Galaxies and M31.” *The Astrophysical Journal* 516.744 (1999 May 10): 749.
- [29] Cherenkov, P.A. “Visible Emission of Clean Liquids by Action of  $\gamma$  Radiation.” *Proceeding of the USSR Academy of Sciences* 2 (1934): 451.
- [30] Cherenkov, P.A. “Radiations of Particles Moving at a Velocity Exceeding That of Light, and Some of the Possibilities for Their Use in Experimental Physics” December 11, 1958. *Nobel Lectures Physics 1942-1962*, Elsevier Publishing Company, Amsterdam, 1964.

- [31] Cocconi, G. *Proceedings of the 6th International Cosmic Ray Conference*, Moscow 1959.
- [32] COESA, United States Committee on Extension to the Standard Atmosphere Technical report , U.S. Standard Atmosphere, National Oceanic and Atmospheric Administration, Rockville, Md. 1976.
- [33] Condon, J.J. “Radio Emission from Normal Galaxies.” *Annual Review of Astronomy and Astrophysics* 30 (1992): 575-611.
- [34] Contursi, A., A. Poglitsch, J. Grácia Carpio, S. Veilleux, E. Sturm, J. Fischer, A. Verma, S. Hailey-Dunsheath, D. Lutz, R. Davies, E. González-Alfonso, A. Sternberg, R. Genzel, L. Tacconi. “Spectroscopic FIR mapping of the disk and galactic wind of M82 with Herschel-PACS.” *Astronomy & Astrophysics* 549 (2013).
- [35] Dale, D.A., , A. Gil de Paz, K. D. Gordon, H. M. Hanson, L. Armus, G. J. Bendo, L. Bianchi, M. Block, S. Boissier, A. Boselli, B. A. Buckalew, V. Buat, D. Burgarella, D. Calzetti, J. M. Cannon, C. W. Engelbracht, G., Helou, D. J. Hollenbach, T. H. Jarrett, R. C. Kennicutt, C. Leitherer, A. Li, B. F. Madore, D. C. Martin, M. J. Meyer, E. J. Murphy, M. W. Regan, H. Roussel, J. D. T. Smith, M. L. Sosey, D. A. Thilker, F. Walter. “An Ultraviolet-to-Radio Broadband Spectral Atlas of Nearby Galaxies.” *The Astrophysical Journal* 655.2 (2007): 863-884.
- [36] Daniel, M.K. “The VERITAS standard data analysis.” *Proceedings of the 30th International Cosmic Ray Conference*, Mexico City, Mexico, 2008.
- [37] Daum. A. et al. [The HEGRA Collaboration]. “First Results on the Performance of the HEGRA IACT Array.” *Astroparticle Physics* 8.1 (1997).
- [38] Davies, J. & M. Cotton. “Design of the Quartermaster Solar Furnace.” *Journal of Solar Energy Science and Engineering* 2.3 (1957): 16-22.
- [39] de Cea del Pozo, E. D. F. Torres & Y. Rodriguez Marrero. “Multimessenger Model for the Starburst Galaxy M82.” *The Astrophysical Journal* 698 (2009 June 20): 1054-1060.
- [40] Dermer, C.D. “Secondary production of neutral pi-mesons and the diffuse galactic gamma radiation.” *Astronomy and Astrophysics* 157.2 (1986): 223-229.
- [41] Diehl, R., H. Halloin, K. Kretschmer, G. G. Lichti, V. Schoenfelder, A.W.Strong, A. von Kienlin, W. Wang, P. Jean, J. Knoedlseder, J.-P. Roques, G. Weidenspointner, S. Schanne, D. H. Hartmann, C. Winkler, C. Wunderer. “Radioactive  $^{26}\text{Al}$  and massive stars in the Galaxy.” *Nature* 439 (2006): 45-47.
- [42] “Emission spectra of the night sky and aurora.” *The Observatory* 67 (1947): 121-127.
- [43] Fazio, G.G., H.F. Helmken, G.H. Rieke & T.C. Weekes. “An experiment to search for discrete sources of cosmic ray gamma rays in the  $10^{11}$  to  $10^{12}$  eV region.” *Canadian Journal of Physics* 46.10 (1968): S451-S455.
- [44] Fegan, D. J., “ $\gamma$ /hadron separation at TeV energies.” *Journal of Physics G: Nuclear and Particle Physics* 23 (1997): 1013.

- [45] Fenech, D.M. T.W.B. Muxlow, R.J. Beswick, A. Pedlar & M.K. Argo, “Deep MERLIN 5GHz Radio Imaging of Supernova Remnants in the M82 Starburst.” *Monthly Notices of the Royal Astronomical Society* 391.3 (2008): 1384-1402.
- [46] Fermi, E. “On the Origin of Cosmic Radiation.” *Physical Review* 75.8 (1994): 1169-1174.
- [47] Ford, R.L. & W.R. Nelson. “The EGS Code System: Computer Program for the Monte Carlo Simulations of Electromagnetic Cascade Showers.” Stanford Linear Accelerator Center Report SLAC-210 (1978).
- [48] Förster Schreiber, N.M., R. Genzel, D. Lutz & A. Sternberg. “The nature of starburst activity in M82.” *The Astrophysical Journal* 599 (2003): 193-217.
- [49] Freedman, W. L., Hughes, S. M., Madore, B. F., Mould, J. R., Lee, M. G., Stetson, P.; Kennicutt, R. C., Turner, A., Ferrarese, L., Ford, H., Graham, J. A., Hill, R., Hoessel, J. G., Huchra, J., Illingworth, G. D. “The Hubble Space Telescope Extragalactic Distance Scale Key Project. 1: The discovery of Cepheids and a new distance to M81.” *The Astrophysical Journal* 427.2 (1994): 628-655.
- [50] Fruin, J.H., J.V. Jelley, C.D. Long, N.A. Porter & T.C. Weekes. “Flux Limits for high-energy from quasi-stellar and other radio sources.” *Physics Letters A* 10 (1964): 176-177.
- [51] Funk, S. , G. Hermann, J. Hinton , D. Berge, K. Bernlöhr, W. Hofmann, P. Nayman, F. Toussenel, P. Vincent. “The Trigger System of the H.E.S.S. Telescope Array.” *Astroparticle Physics* 22 (2004): 285-296.
- [52] Gaisser, T.K. & A.M. Hillas. “Reliability of the method of constant intensity cuts for reconstructing the average development of vertical showers.” *Proceeding of the 15th International Cosmic Ray Conference* Munich 1977.
- [53] Gaisser, T.K. *Cosmic Rays and Particle Physics*. Cambridge:Cambridge University Press, 1990.
- [54] Galbraith, W. & J.V. Jelley. “Light pulses from the night sky associated with Cosmic Rays.” *Nature* 171. 351 (1953).
- [55] Ginzberg, V.L. & S.I. Syrovatskii. *The Origins of Cosmic Rays*. New York:Macmillan, 1964.
- [56] Grieder, P.K.F. *Extensive Air Showers: High Energy Phenomena and Astrophysical Aspects*. New York:Springer, 2010.
- [57] Hamamatsu Photonics K.K., Electron Tube Division, *Photomultiplier Tubes: Photomultiplier Tubes and Related Products*, Updated November 2010, TPMZ0001E01, Printed in Japan.
- [58] Hays, E. “VERITAS Data Acquisition.” *Proceedings of the 30th International Cosmic Ray Conference*, Mérida, Mexico, 2007.
- [59] Heßa, M., K. Bernlöhr, A. Daum, M. Hemberger, G. Hermann, W. Hofmann, H. Lampeitl, F.A. Aharonian, A.G. Akhperjanian, J.A. Barrio, J.J.G. Beteta, J.L. Contreras, J. Cortina, T. Deckers, J. Fernandez, d, V. Fonseca, J.C. Gonzalez, G. Heinzlmann, A. Heusler, H. Hohl, I. Holl, D. Horns, R. Kankanyan, M.



- Kestel, O. Kirstein, C. Köhler, A. Konopelko, H. Kornmayer, D. Kranich, H. Krawczynski, A. Lindner, E. Lorenz, N. Magnussen, H. Meyer, R. Mirzoyan, A. Moralejo, L. Padilla, M. Panter, D. Petry, f, R. Plaga, J. Prahl, C. Prosch, G. Pühlhofer, G. Rauterberg, W. Rhode, A. Röhring, M. Samorski, J.A. Sanchez, D. Schmele, F. Schröder, W. Stamm, H.J. Völk, B. Wiebel-Sooth, C.A. Wiedner, M. Willmerel. “The time structure of Cherenkov images generated by TeV  $\gamma$ -rays and by cosmic rays.” *Astroparticle Physics* 11.3 (1999): 363-377.
- [60] Heck, D., Knapp, J., Capdevielle, J.N., Schatz, G. & Thouw, T. “Users Guide, CORSIKA: A Monte Carlo Code to Simulate Extensive Air Showers.” Forschungszentrum Karlsruhe GmbH, Karlsruhe 1998.
- [61] Heckman, T.M., Lehnert, M.D. & L. Armus. “Galactic Superwinds” *The Environment and Evolution of Galaxies*. Eds. J.M. Shull & A. Thronson Jr. Kluwer. 1993.
- [62] Heitler, W. *The Quantum Theory of Radiation*. 3rd Edition London:Oxford University Press, 1954.
- [63] Helou, G., Soifer, B.T. & Rowan-Robinson, M. “Thermal infrared and nonthermal radio-remarkable correlation in disks of galaxies.” *The Astrophysical Journal* 298 (1985): L7-L11.
- [64] Hillas, A. M. “Cherenkov light images of EAS produced by primary gamma.” *Proceedings of the 19th International Cosmic Ray Conference*, La Jolla, California, 1985.
- [65] Hofmann, W., I. Jung, A. Konopelko, H. Krawczynski, H. Lampeitl & G. Pühlhofer, “Comparison of techniques to reconstruct VHE gamma-ray showers from multiple stereoscopic Cherenkov images” *Astroparticle Physics* 12 (1999): 135.
- [66] Holder, J. “Exploiting the VERITAS Timing Information.” *Proceedings of the 29th International Cosmic Ray Conference*, Pune, India, 2005.
- [67] Holder, J. et al. [The VERITAS Collaboration]. “The First VERITAS Telescope.” *Astroparticle Physics* (2006): 391-401.
- [68] Holder, J. et al. [The VERITAS Collaboration]. “VERITAS: Status and Highlight.” *Proceedings of the 32nd International Cosmic Ray Conference*, Beijing, China, 2011.
- [69] Kachelrieß, M. “Lecture Notes on High Energy Cosmic Rays”, Jyväskylä Summer School. 2008.
- [70] Kamae, T. N. Karlsson, T. Mizuno, T. Abe & T. Koi. “Parameterization of  $\gamma$ ,  $e^\pm$ , and neutrino spectra produced by p-p interactions in astronomical environments.” *The Astrophysical Journal* 647 (2006): 692-708.
- [71] Kieda, D.B. “The Gamma Ray Detection sensitivity of the upgraded VERITAS observatory.” *Proceedings of the 32nd International Cosmic Ray Conference*, Beijing, China 2011.
- [72] Kieda, D.B. “Status of the VERITAS Upgrade.” *Proceedings of the 33rd International Cosmic Ray Conference*, Rio de Janeiro, Brazil, 2013.

- [73] Kronberg, P.P & P.N. Wilkinson. “High-resolution, Multifrequency Radio Observations of M82.” *The Astrophysical Journal* 200 (1975): 430-438.
- [74] Krymsky, G.F. “A regular mechanism for the acceleration of charged particles on the front of a shock wave.” *Proceeding of the USSR Academy of Sciences* 234.1306, 1977.
- [75] Lacki, B.C., T.A. Thompson, E. Quataert, A. Loeb & E. Waxman. “On the GeV and TeV Detection of the Starburst Galaxies M82 & NGC 253.” *The Astrophysical Journal* 734 (2011): 107.
- [76] Lagage, P. O. & Cesarsky, C. J. “The maximum energy of cosmic rays accelerated by supernova shocks.” *Astronomy and Astrophysics* 125.2 (1983): 249-257.
- [77] Lemoine-Goumard M., B. Degrange & M. Tluczykont. “Selection and 3D-Reconstruction of Gamma-Ray-induced Air Showers with a Stereoscopic System of Atmospheric Cherenkov Telescopes” *Astroparticle Physics* 25 (2006): 195.
- [78] Lester, D. F., Gaffney, N., Carr, J. S., Joy, M. “A near-infrared spectroscopic study of the starburst core of M82.” *The Astrophysical Journal* 352 (1990): 544-560.
- [79] Li, T.-P. & Y.-Q. Ma. “Analysis methods for results in gamma-ray astronomy.” *The Astrophysical Journal* 272 (1983): 317-324.
- [80] Lidvansky, A.S. “Air Cherenkov Methods in Cosmic Rays: A Review and Some History.” *Radiation Physics and Chemistry* 75,8 (2006): 891-898.
- [81] Lipsy, S.J & P. Playchan. “Globular Cluster Formation in M82.” *The Astrophysical Journal* 603 (2004): 82-86.
- [82] Longair, M.S. *High Energy Astrophysics* 3rd Edition Cambridge:Cambridge University Press, 2011.
- [83] Lorenz, E. & R. Wagner. “Very high-energy gamma-ray astronomy: A 23-year success story in high-energy astroparticle physics.” *Journal of European Physics* (2012): 459-513.
- [84] Lynds, C.R. & A.R. Sandage. “Evidence for an Explosion in the Center of the Galaxy M82.” *The Astrophysical Journal* 137 (1963): 1005.
- [85] Maciel, W.J, H. J. Rocha-Pinto & R.D.D. Costa. “The star formation rate in the Milky Way: Results from stars and planetary nebulae, The Spectral Energy Distribution of Galaxies.” *Proceedings International Astronomical Union*, 2012.
- [86] Maier, G. “Eventdisplay Introduction.” VERITAS Analysis Bootcamp. Westward Look Hotel, Tucson, Az. January 2014.
- [87] Mannheim, K. D. Elsässer & O. Tibolla. “Gamma-rays from pulsar wind nebulae in starburst galaxies.” *Astroparticle Physics* 35,12 (2012): 797-800.
- [88] Mayya, Y.D., L. Carrasco & A. Luna. “The Discovery of Spiral Arms in the Starburst Galaxy M82.” *The Astrophysical Journal* 628 (2005): L33-L36.
- [89] McCann, A. D. Hanna, J. Kildea & M. McCutcheon. “A New Mirror Alignment System for the VERITAS Telescopes.” *Proceedings of the 31st International Cosmic Ray Conference*, Lodz, Poland, 2009.

- [90] McCann, A. *Discovery of Emission above 100 GeV from the Crab Pulsar with VERITAS* (Doctoral Dissertation), McGill University, Montreal, Quebec, 2011.
- [91] Mohanty, G., S. Biller, D.A. Carter-Lewis, D.J. Fegan, A.M. Hillas, R.C. Lamb, T.C. Weekes, M. West, J. Zweerink. "Measurement of TeV gamma-ray spectra with the Cherenkov imaging technique." *Astroparticle Physics* 9.1 (1998): 15-43.
- [92] Mori, M. "The Galactic Diffuse Gamma-Ray Spectrum from Cosmic-Ray Proton Interactions." *The Astrophysical Journal* 478 (1997): 225-232.
- [93] Morrison, P. "On Gamma-Ray Astronomy." *Il Nuovo Cimento* 7.6 (1958).
- [94] Naylor, B. J., C. M. Bradford, J. E. Aguirre, J. J. Bock, L. Earle, J. Glenn, H. Inami, J. Kamenetzky, P. R. Maloney, H. Matsuhara, H. T. Nguyen, J. Zmuidzinas. "A Census of the High-density Molecular Gas in M82." *The Astrophysical Journal* 722 (2010): 668-681.
- [95] Nelson, W.R., H. Hirayama & D.W.O. Rogers. "The EGS4 Code System." SLAC National Laboratory Report, SLAC-265, UC-32, E/I/A 1985.
- [96] O'Connell, R.W. & J.J Mangano. "The central regions of M82." *The Astrophysical Journal* 221 (1978): 69-79.
- [97] Ohm, S. & J.A. Hinton. "Non-thermal emission from Pulsar-Wind Nebulae in Starburst Galaxies." *Monthly Notices of the Royal Astronomical Society* (2012): 1-5.
- [98] Ong, R. A. "Very high-energy gamma ray astronomy." *Physics Reports* 305 (1998).
- [99] Ostapchenko, S. "QGSJET-II: physics, recent improvements, and results for air showers." *EPJ Web of Conferences* 52 (2013).
- [100] Otte, N. "Upgrade of VERITAS with high efficiency photomultipliers." *Proceedings of the 32nd International Cosmic Ray Conference*, Beijing, China, 2011.
- [101] Paglione, T.A.D. & R.D. Abrahams. "Properties of Nearby Starburst Galaxies Based on their Diffuse Gamma-ray Emission." *The Astrophysical Journal* 611.2 (2012): 106.
- [102] Persic, M. Y. Rephaeli & Y. Arieli. "VHE emission from M82." *Astronomy and Astrophysics* 486.1 (2008): 143-149.
- [103] Pohl, M. "On the Predictive Power of the Minimum Energy Condition. II. Fractional Calorimeter Behavior in the Diffuse High Energy Gamma Emission of Spiral Galaxies." *Astronomy and Astrophysics* 287 (1994): L17.
- [104] Prokoph, H. "Investigations on gamma-hadron separation for imaging Cherenkov telescopes exploiting the time development of particle cascades." Deutsches Elektronen-Synchrotron Report No.:PHPPUBDB-12192, 2009.
- [105] Prokoph, H. "Observations and modeling of the active galactic nucleus B2 1215+30 together with performance studies of the ground-based gamma-ray observatories VERITAS and CTA." (Doctoral Dissertation), Mathematisch-Naturwissenschaftlichen Fakultät I der Humboldt-Universität zu Berlin, Berlin, Germany, 2013.

- [106] Ratliff, G. & J. Grube. “Update on M82.” VERITAS Collaboration Meeting. Westward Look Hotel, Tucson, AZ. January 2015.
- [107] Rieke, G.H., M.J Lebofsky, R.I. Thompson, F.J. Low & T. Tokunaga. “The Nature of the Nuclear Sources in M82 and NGC 253.” *The Astrophysical Journal* 238 (1980): 24-40.
- [108] Roache, E., Irvin, K., Perkins, J.S., Harris, K., Falcone, A., Finley, J., and T. Weeks. “Mirror Facets of the VERITAS Telescopes.” *Proceedings of the 30th International Cosmic Ray Conference*, Mexico City, Mexico, 2008.
- [109] Robitaille, T.P. & B. A. Whitney “The present-day star formation rate of the Milky-Way determined from Spitzer detected young stellar objects.” *Astrophysical Journal Letters* 710 (2010): L11-L15.
- [110] Schmidt, F. & J. Knapp, 2005, “CORSIKA Shower Images.” Web. January 2015. <<http://www-zeuthen.desy.de/~jknapp/fs/>>.
- [111] Skrutskie M.F, R. M. Cutri, R. Stiening, M. D. Weinberg, S. Schneider, J. M. Carpenter, C. Beichman, R. Capps, T. Chester, J. Elias, J. Huchra, J. Liebert, C. Lonsdale, D. G. Monet, S. Price, P. Seitzer, T. Jarrett, J. D. Kirkpatrick, J. E. Gizis, E. Howard, T. Evans, J. Fowler, L. Fullmer, R. Hurt, R. Light, E. L. Kopan, K. A. Marsh, H. L. McCallon, R. Tam, S. Van Dyk, S. Wheelock. “The Two Micron All Sky Survey (2MASS).” *The Astronomical Journal* 131 (2006): 2.
- [112] Sofue, Y. “Is M82 A Disk-truncated Bulge by a close encounter with M81?” *Publication of the Astronomical Society of Japan* 50 (1998): 227-231.
- [113] Stecker, F.W. *Cosmic Gamma Rays* Scientific and Technical Information Office, National Aeronautics and Space Administration, NASA SP-249 (1971).
- [114] Stokes B., Ivanov, D. & Thomas, G. “A Comparison between Hadronic Interaction Models and Observations by the Telescope Array.” *Proceedings of the International Cosmic Ray Conference*, Rio de Janeiro, (July 2013).
- [115] Strickland, D.K., T.J. Ponman & I.R. Stevens. “ROSAT Observations of the Galactic Wind in M82.” *Astronomy & Astrophysics* 320, 378 (1997).
- [116] Subaru Telescope Facility. “New images of starburst galaxy M82 reveal multiple sources of its superwind.” Web. March 2011. <<http://www.astronomy.com/news/2011/03/new-images-of-starburst-galaxy-m82-reveal-multiple-sources-of-its-superwind>>
- [117] Tamm, I.E. & I.M. Frank. “Kogerentnoe izluchenie bystrogo elektrona v srede” (“The coherent radiation of a fast electron in a medium”) *Proceedings of the Russian Academy of Sciences* 14.107 (1937).
- [118] Tamm, I.E. “Radiation Emitted by Uniformly Moving Electrons.” *Journal of Physics-USSR* 1.439 (1939).
- [119] Telesco, C.M. & D.A. Harper. “Galaxies and Far-Infrared Emission.” *The Astrophysical Journal* 235 (1980): 392-404.
- [120] Tešić, G. & Staszak, D. “D.C. to PE Ratio from Photostatistics and Single Photoelectron Runs.” VERITAS Calibration and Simulations Meeting, Tucson, AZ January 2012.

- [121] *Timeline to VERITAS*, The VERITAS Collaboration. Web. June 2015. <<http://veritas.sao.arizona.edu/about-veritas-mainmenu-81/history-aamp-timeline-mainmenu-89>>
- [122] Torres, D.F. “Theoretical modeling of the diffuse emission of  $\gamma$ -rays from extreme regions of star formation: The case of Arp 220.” *The Astrophysical Journal* 617 (2004): 966.
- [123] Völk, H.J & K. Bernlöhr. “Imaging Very High Energy Gamma-Ray Telescopes.” *Experimental Astronomy* 25 (2009): 173-191.
- [124] Wakely, S. & D. Horan. *TeVCat*. Univeristy of Chicago. Web. June 2015. <<http://tevcat.uchicago.edu>>.
- [125] Weekes, T.C., M.F. Cawley, D.J. Fegan, K.G. Gibbs, A.M. Hillas, P.W. Kwok, R.C. Lamb, D.A. Lewis, D. Macomb, N.A. Porter, P.T. Reynolds, G. Vacanti. “Observation of TeV Gamma Rays from the Crab Nebula using the Atmospheric Cerenkov Imaging Technique.” *The Astrophysical Journal* 342 (1989): 379-395.
- [126] Weekes, T.C. “TeV gamma ray astronomy.” *Nuclear Physics B-Proceedings Supplements* 38.1-3 (1995): 457-466.
- [127] Weekes, T.C. “How We Got from There to Here.” *Proceedings from Trevorfest Tucson, Arizona* (2013).
- [128] Weinstein, A. “The VERITAS Trigger System.” *Proceedings from the 30th International Cosmic Ray Conference*, Mexico City, Mexico, 2007.
- [129] Yun M.S., P.T.P. Ho & K.Y. Lo. “A high-resolution image of atomic hydrogen in the M81 group of galaxies.” *Nature* 372 (1994): 530-532.
- [130] Zatsepin, V.I. & A.E. Chudakov. “On the methods of searching for local sources of high energy photons.” *Journal of Experimental Theoretical Physics* 41.655 (1961).
- [131] Zitzer, B. “The VERITAS Upgraded Telescope-Level Trigger System: Technical Details and Performance Characterization.” *Proceeding of the 33rd International Cosmic Ray Conference*, Rio de Janeiro, Brazil, 2013.